
THE UNIVERSITY of ADELAIDE

# Cement Sheath Integrity Assessment Subject to Pressure and Temperature Variations

Elaheh Arjomand

Thesis submitted in fulfilment of the requirements

for the degree of Doctor of Philosophy

The University of Adelaide
Faculty of Engineering, Computer and Mathematical Sciences
School of Civil, Environmental and Mining Engineering
December 2018

# Contents

## List of Figures:

## List of Tables:

# Abstract

The exploration and exploitation of hydrocarbon wells should not cause any environmental hazards including contamination of groundwater (aquifers) and atmosphere. The cement placed in the annular gaps between the casing strings and the formation acts as a key barrier to provide zonal isolation and maintain the integrity of the wells.

The integrity of the cement sheath and the cement sheath interfaces is susceptible to be compromised during well operational processes, including but not limited to, pressure integrity tests (PIT), completion operations, stimulation treatments, and production processes. The cement sheath may experience different types of mechanical damage as a result of being exposed to these different wellbore operational procedures. Therefore, understanding of cement failure mechanisms is of the utmost importance for better assessments of wellbore integrity.

This thesis demonstrates the results of the experimental-numerical studies and investigates the integrity of the cement sheaths subjected to pressure and temperature variations.

The overall purpose of this study is to improve the modelling capabilities of cement sheath integrity assessments by employing a more comprehensive constitutive model for the cement sheath compared to the rest of the models previously used. The experimental studies on the behaviour of the cement-based specimens under compression tests showed a strong non-linearity in the obtained stress-strain curves which confirms the necessity of applying plasticity theories. However, it is hard to explain the elastic stiffness degradation of the cement-based materials which happens during experiments using the classical plasticity theories. Therefore, in this thesis, the modified Concrete Damage Plasticity (CDP) model was employed, particularly formulated for modelling geo-materials such as rocks, concrete, and cementitious materials. The Concrete Damage Plasticity is a continuum model which combines plasticity and damage mechanisms, considering two different tensile and compressive state of damage. The yield criterion in the CDP model also represents the pressure-dependency of the geo-material behaviour under shearing at different levels of confinement in addition to the incorporation of non-associated flow rule (material dilatancy). These features show the superiority of the CDP model for employing in cement sheath integrity assessments.

However, the paucity of cement class G mechanical parameters, e.g. lack of experimental data under different confining pressure and tensile properties, was an impediment to the incorporation of Concrete Damage Plasticity model.

Therefore, the experimental aspect of this study intends to expand the cement class G inventory. The experimental data and analyses added to inventory are as followed. The investigations of curing temperature and pressure confinements effects on the strength and post-peak response of the cement class G under compression and also obtaining cement tensile properties. The experimental results show by increasing the curing temperatures, the compressive strength of the material decreases significantly. This effect is attributed to the differences in the formation of calcium silicate hydrate (CSH) gels due to an increase in the curing temperature. Additionally, by increasing the confining pressure, the load-carrying capacity of specimens increases, and cement shows more ductile behaviour. The results of three-point bending tests to obtain cement tensile properties on prismatic samples showed that some modifications were required to be able to measure cement fracture energy properly. Modifications were incorporated by employing the crack-mouth clip gauge opening displacement to control the test loading rate, which led to less brittle behaviour and allowed us to obtain the fracture energy. The results collected from the clip gauge were validated by Digital Image Correlation (DIC) technique measurements. The approximate shape of the yield surface for elastoplastic models was procured utilizing the experimental data. The corresponding constitutive model parameters were computed by the curve fitting process and were validated by numerical analyses. The incorporation of the obtained parameters leads to the more accurate implementation of concrete damage plasticity model in cement sheath integrity assessments.

In the numerical modelling aspect of this thesis, the integrity of cement sheaths was assessed based on the local compression and tensile damage, and global damage indicators within the cement sheaths considering different mechanical and thermal loading scenarios. The occurrence of maximum compression and tensile damage on the narrowest side of the eccentric cement sheaths confirms the importance of casing centralisation. The global damage indicator of compressive (crushing) and tensile (cracking) states shows a higher possibility of cement sheath failure while operating in anisotropic in-situ stress fields with soft rocks. The high magnitude of tensile damage (cracking index) in some simulations confirms the importance of incorporating tensile damage mechanisms into the constitutive modelling. The simulations result also showed that cement sheaths subjected to controlled heating rates might experience less potential compression damage comparing to cement sheath subjected to instant heating. The magnitude and localisation of tensile damage were shown to be more dependent on the geometry of the wellbore rather than the heating rates. In cooling scenarios, the effects of wellbore contractions due to

temperature reduction on the cement sheath integrity were shown to be minimal due to the dominant effect of pressurizing the wellbore and in-situ stress confinement.

Ultimately, this research leads to better cement sheath integrity evaluations subjected to pressure and temperature variations using the CDP model along with the incorporation of calibrated the constitutive model parameters using the experimental data.

# Statement of originality

I certify that this work contains no material which has been accepted for the award of any other degree or diploma in my name, in any university or other tertiary institution and, to the best of my knowledge and belief, contains no material previously published or written by another person, except where due reference has been made in the text. In addition, I certify that no part of this work will, in the future, be used in a submission in my name, for any other degree or diploma in any university or other tertiary institution without the prior approval of the University of Adelaide and where applicable, any partner institution responsible for the joint-award of this degree.

I acknowledge that copyright of published works contained within this thesis resides with the copyright holder(s) of those works.

I also give permission for the digital version of my thesis to be made available on the web, via the University's digital research repository, the Library Search and also through web search engines, unless permission has been granted by the University to restrict access for a period of time.

I acknowledge the support I have received for my research through the Completion Scholarship.

Signature: Date: 11-12-2018

# Acknowledgements

I gratefully acknowledge my principal supervisor Dr Terry Bennett, and my co-supervisor Dr Giang D Nguyen who have always supervised, supported and encouraged me during my candidature period. Your combined skill, expertise and passion for research have been precious to me.

I would also like to thank the following people wholeheartedly.

I would like to sincerely thank Mr Ian Cates, Mr Simon Golding, Mr Ian Ogier, and Mr Dale Hodson for their kind help and great support during my experimental phase of the research. I extend this gratitude to the other staff at ECMS infrastructure and technical services department for their assistant.

I would also thank Leticia Mooney for her editorial assistance in improving one of my manuscripts.

I would also like to thank Professor Martin Lambert for his support in providing the Completion scholarship.

My fellow postgraduate students and academics at the University of Adelaide. Our discussions over the years provided a great deal of insight and encouragement during my candidature.

Finally, I would like to thank my parents, for supporting me emotionally during my PhD research. Last but not least, I would like to thank my husband for his selfless love and support.

*December 2018*

# 1. Introduction

There are more than four million onshore hydrocarbon wells drilled worldwide [9] with nearly 10000 in Australia alone [9] (from data retrieved from Geoscience Australia). A wellbore provides access to natural sources such as oil and gas. The wellbores are encased in different layers of steel casings and cement sheaths within the annuli. After drilling, the steel casing is run into a borehole, and be placed and protected with the help of Portland cement. The cement is placed by cement slurry circulation downward through the central wellbore and up the annular space between the casing and the rock. Layers of the casing with decreasing diameters are placed at the centre of the hole in each step [10-12]. The number of casing strings is dependent on the formation properties for each wellbore. In general, a well can have between two to four casing strings including the conductor, surface, intermediate, and production casing as shown in Figure 1.1. These casing strings run to different depths, and one or two of them may not be required based on the drilling conditions. These strings might be run as liners or in combination with liners [1].

Conductor casing is the first layer of casings with the largest diameter running from the surface until the depth of 12-150 meters in onshore wells and up to 300 meters in offshore wells [1]. Conductor casing prevents any unconsolidated surface sediments to enter the wellbore [1]. Surface casing is placed after conductor casing is installed and cemented. The length of surface casing varies according to each well design and can be up to 1500 meters. One of the roles of surface

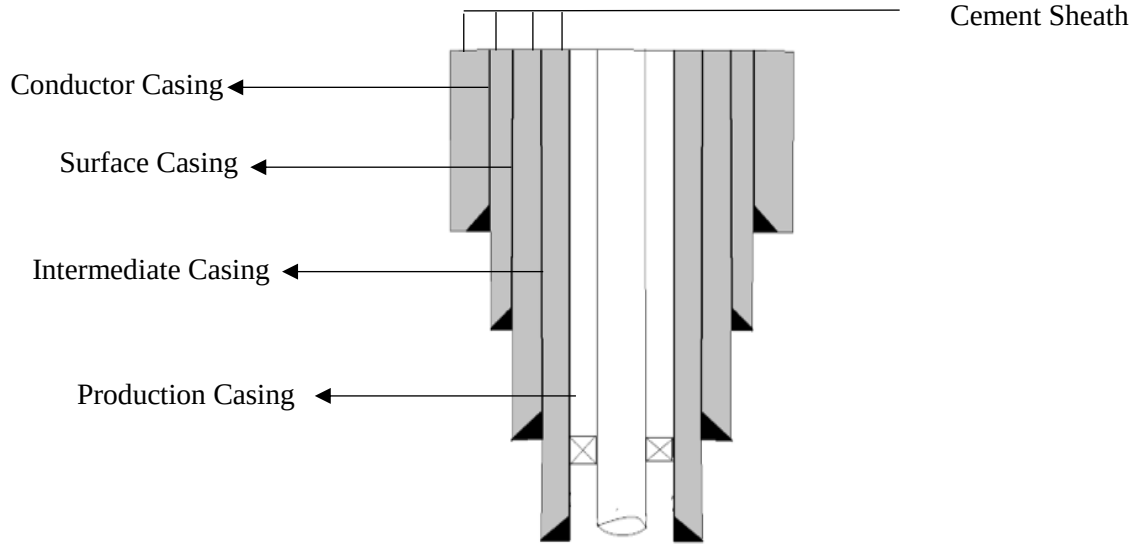


Figure 1.1: Wellbore Architecture after [1]

casing is isolating the freshwater-bearing formations [1]. The intermediate casing or protective casing is placed between the surface casing and production casing to protect any unusual high-pressure rock from initiating wellbore instability. An additional layer of intermediate casing might be required corresponding to the different formation characteristic, i.e. abnormal formation pore pressure. Intermediate casing varies in length from 2000-4500 meters [1]. The Production casing is run as the final casing, and it starts from the surface to the reservoir, and it protects the prospective productive zone from other subsurface formations [1, 13].

The exploration and exploitation of hydrocarbon wells should be in line with the protection of the environment to prevent groundwater (aquifers) contamination [14, 15] and migration of fugitive emissions [16] into the atmosphere [9]. Groundwater sources are protected from the contents of well operational processes, i.e. drilling, hydraulic fracturing, production operations, etc. by layers of steel casing, and cement sheaths which act as multiple barriers to separate the formation fluids from the outside environment [17]. Although wellbores are sealed and prevent any communication between formation fluid and geologic strata (which may contain groundwater), the integrity of wellbores might still be compromised [9, 18]. At this point, wellbores may turn into the high-permeability conduits for the formation fluids [19] which impose a potential risk to the environment by polluting the groundwater and atmosphere. To maintain the integrity of the wellbores, a wellbore barrier system should be designed in a way to endure the mechanical and thermal operational procedures imposed by production and recovery phases during a wellbore lifetime.

However, wellbore barrier failure might occur due to the failure of the individual or multiple barriers even if there are no indications of detectable leakage into the wellbore surroundings [18]. If a barrier fails, an assessment has to be done to evaluate the imposed risk of fluid leakage and repairing procedures should be planned. A barrier failure might happen during different stages of a wellbore lifetime, i.e. pre-production phases / and production phases [20].

### 1.1. Barrier Failure during Pre-Production Phase

Some of the well operational procedures may lead to a barrier failure in the pre-production phase, i.e. pressure integrity tests (leak-off tests) [21-24], extended leak-off tests [25]. Pressure integrity tests (PIT) are performed after the cementation of each casing, and impose pressure upon set cement [26]. Drilling practices may also damage the unstable formations (caving) due to the imposed vibrations and pressures which may lead to formation failure. In addition, some formations are naturally weak and not stable enough or may have some faults and cracks. These

faults can threaten the integrity of the wellbores even before the commencement of production procedures [20, 27].

The casing centralization should be executed properly. Otherwise, the cement would not be able to move the mud from the annulus completely during cementing procedures and leads to the formation of eccentric cement sheath and non-uniform cement sheath thickness or possibly not fully covers the created gap [20]. This deviation of the casing from the centre can cause unbalance concentration of stress on the one side of the wellbore which results in additional shear stress to the cement sheath [28].

The existence of mud cake and grease deteriorates the bond strength between the cement with the casing and the formation during cement pumping procedure. Additionally, contamination of cement by mud or formation fluid may weaken the cement mechanical properties as well, which may lead to compromising the wellbore integrity. [20, 29]. Muds have a thixotropic behaviour and tend to build a gel-structure under low shear circumstances. The gelled pockets should be broken up and cleaned to achieve a stronger cement bonding. Another reason could be related to the improper composition (cement slurry formulation) of the cement slurry, in terms of its compatibility with the formation which results in weak bonding properties [12, 20].

Cement shrinkage leads to a volumetric reduction and can consequently cause de-bonding between cement and casing or formation. This can also result in tensile cracks and increased permeability which provides pathways for undesired fluid and gas migration. [12, 20, 30].

Due to high-pressure conditions (high gradient of pressure between the well and the formation), the fluid in the cement slurry could be filtrated. This lack of water during the hydration process will decrease the cement strength [20].

## 1.2. Barrier Failure during Production Phase

During production phases, the mechanical and thermal stress state of a wellbore is subjected to different pressure and temperature variations due to different reasons [31] including the alteration in induced pressure and temperature originating from casing expansion / contraction [32], hydraulic stimulation [33], loading from formation stresses such as tectonic stress, subsidence and formation creep [12], change of pore pressure or temperature [34], normal well production [12], injection of hot steam or cold water [35, 36], etc. These operational procedures have significant effects on the integrity and the failure mechanism of cement sheaths.

Wellbore integrity failure might occur when all the wellbore barriers fail, and leakage pathways are created. Thus, leakage is detected in the soils, strata, and or atmosphere [18]. Potential leakage pathways might already exist or be created in different regions within these multiple barriers

system during the lifetime of a wellbore [10]. Leakage paths are divided into two categories, primary and secondary. Primary category is more related to the time of primary cementing and secondary are associated with the events and conditions after cementing is complete [6].

Figure 1.2 illustrates the possible locations of primary and secondary leakage pathways along a wellbore. Primary leakage pathways can be created due to casing burst or collapse (Figure 1.2b) [6, 10], unsatisfactory annular cementing job when the cement does not fill the annulus entirely (Figure 1.2f), poor bonding due to the existence of mud cake (Figure 1.2g), and development of channels in the cement (figure 1.2d) [6].

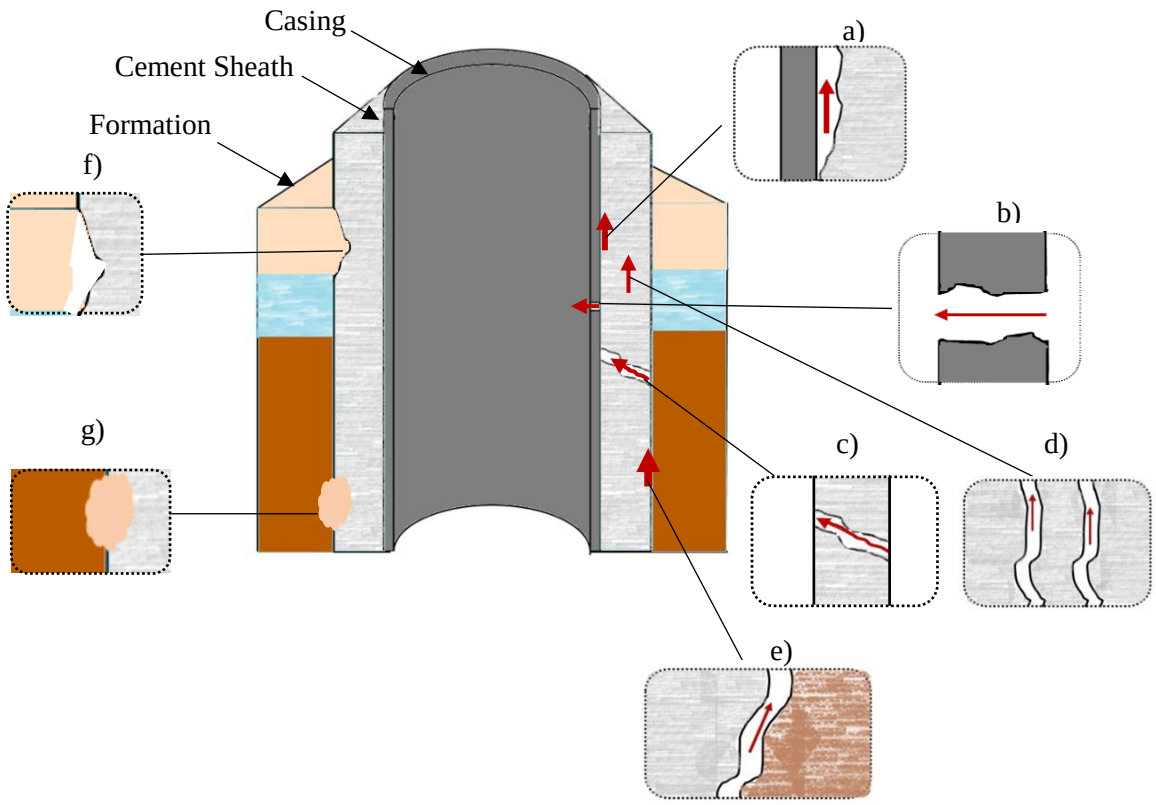


Figure 1.2 : Potential Leakage Pathways along a Wellbore after [6, 7]

The secondary category included the leakage pathways created along micro-annuli at the cement sheath interfaces with the casing and the formation respectively [7, 10] as shown in Figure 1.2a and Figure 1.2e, and degraded or cement fractures (Figure 1.2c) [6, 10].

These pathways might be created due to many reasons including but not limited to deterioration of cement bond strength which leads to the creation of micro-annulus at cement interfaces with the casing and the formation, poor removal of the mudcake formed during drilling, mechanical failure of the casing, cement shrinkage, and cement mechanical failure [34].

The cement sheath is subjected to variations of mechanical and thermal cycles due to different wellbore operational processes, i.e. drilling, hydraulic fracturing, production operations, etc. during the lifetime of a wellbore. Hence, the integrity of the cement sheath and the cement sheath bonding integrity [37] affect the long-term integrity of the wellbores significantly [6].

It is worth noting that the cement used in the oil and gas industry has very low permeability, usually less than a 0.2 mD [38] which indicates that hydraulic isolation is accomplished straightforwardly, and any possible leakage can only occur through mechanical failures of the cement sheath [11]. Therefore, the integrity of the cement sheath may be compromised mostly because of the creation of cracks and micro-annulus within the cement sheath [39].

## 1.3. Cement Sheath Serving as the Key Barrier

Well-cementing (cementation) is an influential stage of a wellbore completion since the cement sheath is responsible for providing complete zonal isolation [40]. The cement sheath should meet both short-term and long-term required characteristics to overcome all pressure and temperature variations imposed to a well during well lifetime and also after it is decommissioned/abandoned [41]. Accordingly, it is of utmost importance to comprehend the cement mechanical failure mechanisms. The cement sheath may experience different types of mechanical damage as a result of exposing to different wellbore operational procedures [8].

It is worth noting that cement class G is mostly utilised in the oil and gas industry. Class G is manufactured by implementing the improved technology in slurry acceleration and retardation with respect to their chemical reactions. Manufacturers are not allowed to add special chemicals, including glycols or acetates, to the clinkers [42]. These chemicals enhance the grinding efficiency but have been shown to intervene with the effect of various cement additives. Classes G and H are the most commonly employed in well cements nowadays. Class G is mostly utilised as a basic ingredient for cementing from the surface to 8,000 ft (2,440 m) depth as manufactured or can be employed along with accelerators and retarders to cover a wide range of well depths and temperatures [42].

Figure 1.3 schematically demonstrates the different types of cracks may occur within the cement sheaths. Radial cracks (Figure 1.3a) might be created due to the difference in pressure between the inner wall of the cement sheath with the outer wall which leads to the cement sheath expansion/contraction [8]. The cement sheath may experience a large deviatoric state of stress which leads to shear damage (Figure 1.3b) [8]. Disking cracks might be created due to axial sliding / disking of the cement sheath (Figure 1.3c) [8]. The cement sheath interfaces debonding may occur due to the uneven expansion/contraction of the cement sheath in comparison with the

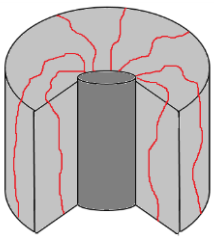

a) Radial Cracking

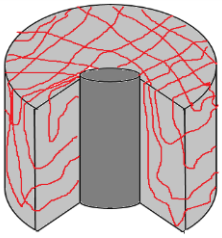

b) Shear

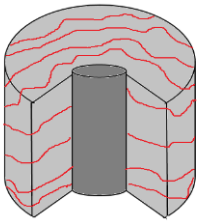

c) Disking Cracks

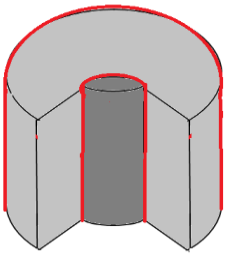

d) Interface debonding

Figure 1.3: Different Types of Cracks within the Cement Sheath after [6, 8]

displacement of the surrounding wellbore components which leads to the creation of micro-annulus within the wellbores (Figure 1.3d) [8]. Consequently, understanding of cement failure mechanisms under different operating conditions is of the utmost importance for the better evaluation of wellbore integrity.

Mechanical failure of the cement sheath within a wellbore is affected and governed by many factors including material mechanical properties (cement compressive strength [4-6], Young's modulus [43-45], tensile strength [31, 46], and bond strength [37, 47]), loading conditions (in-situ stresses [44, 46, 48]), cement history (cement shrinkage) [8], and also wellbore architecture (cement sheath thickness, formation properties, cement sheath eccentricity, and wellbore deviation [8, 37]).

A comprehensive model is required to consider the contribution of each aforementioned factor in predicting the initiation and propagation of the cement mechanical failure. So far, different analytical and numerical modelling approaches were carried out to achieve a better assessment of cement sheath integrity in wells. Numerical modelling, including Finite Element Method (FEM) in particular, has been considerably improved regarding their accuracy and ability to incorporate different constitutive models, complex types of geometry and boundary conditions, and in-situ stress conditions [47]. The incorporation of appropriate material constitutive law and subsequently the evolution of corresponding model parameters are fundamental stages in order to develop a numerical model.

To this point, the linear elastic was employed in a few cement integrity analyses, i.e. [28, 37, 49]. However, the obtained stress-strain curves from the isotropic drained compression tests on the cementitious specimens by [36] are non-linear. Therefore, the employment of linear elastic theory in cement integrity simulations perturbs the accuracy and reliability of the results. Additionally, the existence of the permanent strains upon unloading [36] confirms the incompatibility of linear elastic theory in cement integrity evaluations again as the elastic theory does not incorporate the time-dependency and materials hysteresis law [50].

The non-linear approaches including those employing Von-Mises [51], Mohr-Coulomb / with smeared cracking [31, 44], Drucker-Prager [52], Ottosen model [5, 53], and modified Cam-Clay [36] were incorporated in the cement sheath integrity assessments to alleviate the shortcomings of the linear elastic models. These approaches along with their merits and limitations are reviewed in the literature review Section 3.1.2. completely.

Notwithstanding all the progress has been made in the cement integrity simulations in numerical fields, some aspects of the modelling still require attention including the incorporation of a comprehensive constitutive which reflects both compression and tensile damage mechanisms in addition to the pressure-dependency of the behaviour subjected to confining pressures. Furthermore, the incompleteness of the cement (cement class G utilised in oil and gas industry) mechanical parameters inventory is another impediment to the numerical modelling, for instance, the function of triaxial tests experiments to approximate the shape of the shape of yield / and failure surfaces are neglected. The measurement procedures of cement tensile strength properties, fracture energy, in particular, are not consistent. However, these properties are required to simulate the tensile behaviour mechanism. Moreover, the effect of curing temperature on the cement long-term mechanical properties was also missing from the literature to the best of author's knowledge. The experimental studies available in the literature are explored and reviewed in section 3.2. along with their merits and limitations.

Consequently, in this research, the emphases were placed on filling the gaps in the cement mechanical properties inventory in addition to the incorporation of an appropriate constitutive model (Concrete Damage Plasticity model) specifically formulated for the modelling of geo-materials developed and modified by [54, 55].

The main advantage of Concrete Damage Plasticity (CDP) model is coupling plasticity with damage mechanism which evidently describes the elastic stiffness degradation of materials during the experiments due to the creation of microcracking. The creation of microcracks which is also characterized by softening behaviour of the materials is difficult to explain using classical

plasticity models [55]. The modified version of CDP by [55] benefits from considering the difference in tensile and compressive responses of geo-materials since geo-materials experience different states of damage while subjected to different loading conditions. This model also considers the materials pressure-dependency behaviour under shearing at different levels of confinement. The non-associated flow rule which represents the dilatancy of the geo-materials also embedded into the model. These features make this model a very suitable model to be applied to a range of geo-materials including rocks, and cement-based materials [55].

To be able to incorporate the CDP model into the simulations the corresponding constitutive model parameters were determined by experimental investigations along with parameters calibrations to ensure their reliability for cement sheath integrity assessment.

In the experimental aspects of this thesis, laboratory experiments including confined and unconfined compression tests, and three-point bending tests considering different curing conditions were performed on specimens manufactured from class G well cement. The approximate shape of the yield surface for elastoplastic models was obtained using the aforementioned experimental data, and the corresponding parameter intended for Concrete Damage Plasticity model was computed by calibration process and were also validated by numerical analyses. The incorporation of the obtained parameters leads to the more accurate implementation of Concrete Damage Plasticity model into the cement sheath integrity assessments.

In the numerical aspects, three-dimensional (3-D) finite element frameworks are developed employing the constitutive model for cement sheath and a surface-based cohesive behaviour for the interfaces in the cement sheath integrity investigations. The obtained parameters from the experimental aspect of this thesis implemented into the Concrete Damage Plasticity model for the cement sheath subjected to variations of mechanical and thermal loads. The effects of anisotropy of in-situ stresses, different stiffnesses of surrounding rocks, and different degrees of cement sheath eccentricity within the wellbores on the integrity of the cement and interfaces are also investigated.

Moreover, the outcomes of numerical models are mesh dependent which might be a source of uncertainty within the integrity simulations. To lessen the drawbacks of mesh dependency in numerical analyses the concepts of crack band methodology by Bažant and Oh [56] was applied through incorporation of the characteristic length [57] in utilised software (ABAQUS) which is related to the element size and formulating the softening part of the constitutive law by embedding the stress-displacement instead of stress-strain relationship. Incorporating the stress-displacement

formulation leads to the computation of the correct amount of energy is dissipated and significantly lessens the mesh dependency issue [58].

# 2. Thesis Overview

This thesis is organised into nine chapters where the main contributions are presented in **Chapter 5** to **Chapter 7**. Each of these chapters is presented in the form of a technical paper. The first of these has been published in the *Journal of Petroleum Science and Engineering*, the second has been published in *Australian Journal of Civil Engineering*. The third paper is well-prepared and will be submitted for peer review shortly.

In **Chapter 3,** a literature review was explored on cement sheath integrity modelling and experimental laboratory studies. The advantages and limitations of different approaches in the literature were assessed which leads to the identification of the research gaps.

**Chapter 4** explains the overall objective of this research along with the three specific objectives and the linkage between the research objectives and papers.

In **Chapter 5**, an experimental-numerical study is represented to investigate the effect of enhancing pressure on the cement sheath integrity. Concrete Damage Plasticity constitutive model specifically formulated for the modelling of geo-materials was applied to the investigations of cement sheath integrity, incorporating both compression and tensile damage mechanisms. Laboratory experiments were carried out to obtain strength properties of cement class G followed by calibration of the model parameters based on the obtained experimental results. A three-dimensional finite element framework employing the constitutive model for cement sheath and a surface-based cohesive behaviour for the interfaces was developed for integrity investigations. The effects of different orientations and the anisotropy of in-situ stresses, different stiffness's of surrounding rocks, and the eccentricity of the casing within the wellbore on the integrity of the cement and interfaces were investigated.

**Chapter 6** describes the laboratory experiments that were carried out to investigate the effect of curing conditions on the cement class G mechanical properties, including confined and unconfined compression tests and three-point bending tests on specimens cured at different conditions. The interpretation of the results and experimental parameters calibration and validation were performed to ensure their suitability to predict the behaviour of cement class G.

In **Chapter 7**, a numerical approach was undertaken to investigate the integrity of eccentric cement sheaths after being subjected to mechanical and thermal wellbore operational procedures in relation to the creation of cracks within the cement sheath. The importance of incorporating the appropriate constitutive model (Concrete Damage Plasticity model) for modelling geo-materials such as well cement was highlighted. Three-dimensional finite element frameworks employing the constitutive model for the cement sheath and a surface-based cohesive behaviour accompanied

by defining thermal conduction behaviour at the interfaces were developed. A parametric study was also carried out to assess the effect of wellbore architecture (e.g. casing eccentricity, different layers of cement sheath and casing), different heating and cooling rates on the integrity of cement sheath.

Conclusions are portrayed in **Chapter 8**, which summarises the research contributions and contains a discussion of the limitations and recommendations for future work following with the references in **Chapter 9**.

# 3. Literature Review

The importance of applying a comprehensive model to simulate the cement sheath behaviour under downhole conditions has been highlighted throughout the introduction chapter. In the following sections, the cement sheath numerical modelling and the cement experimental studies are reviewed.

## 3.1. Cement sheath Modelling

Cement sheath integrity models investigated could be categorised into analytical and numerical models. Analytical methods are generally performed by applying simplified assumptions to facilitate finding solutions. The accuracy of analytical models and subsequently their solutions are limited to the correctness and the suitability of their initial assumptions and simplifications [47]. While numerical modelling can be very advantageous considering its ability to incorporate material non-linearity, different types of geometry and boundary conditions, and in-situ stress conditions [9], the accuracy of these numerical models is reliant on the validation and verification of obtained experimental data utilised as inputs for constitutive models [47].

Different wellbore operations including sudden dynamic loading [59], perforation of the casing [11], $CO_2$ injections [60], hydraulic fracturing [61], acidization and finally production of the reservoir, variations of production rate [37], pressure integrity tests (leak-off tests) [24] affect the stress distribution within the cement sheath and the cement sheath bond with the casing and the formation. During pressure testing, fracturing and acidizing and normal production, the wellbore will be pressurised which may lead to different failure mechanisms (compression/shear) to the cement sheath. The tensile failure may also happen as the results of high contact shear stress at the interfaces of the cement sheath with the casing and the rock formation due to pressuring or de-pressuring the wellbores. CO2 injections may cause thermally induced expansion and contraction within the wellbores, possibly resulting in the formation of leakage paths. The thermal loading and unloading generate thermal stresses inside the wellbore components [62]. Consequently, the well barrier materials may fail as a result of the thermal cycling operations.

### 3.1.1. Cement Sheath: Analytical Modelling

Thiercelin, Dargaud, Baret and Rodriquez [63] developed a plane strain analytical approach to measure the induced damage and determining of controlling key parameters assuming the linear-elastic properties for cement, axisymmetric geometry, and fully bonded or unbound situations for

the interfaces. Their results showed the mechanical response of the set cement is dependent on the mechanical properties of the cement and the rock, and wellbore geometry.

Honglin, Zhang, Shi and Xiong [64] have proposed a 2-Dimensional (2-D) analytical model using Mohr-Coulomb failure criterion to investigate the effect of well head casing pressure (WHCP) on the cement sheath integrity in high pressure and temperature (HPHT) wellbores. They suggested a safety factor diagram considering different ranges of temperature and WHCP at the casing interface. Their safety factor diagram showed in the circumstances with high WHCP, the influence of temperature change on the cement sheath failure was diminished which also results in low safety factors. They stated that in cases with WHCP below 40MPa, the effect of temperature can generally be neglected.

Shi, Li, Guo, Guan and Li [65] estimated the initial radial and tangential stresses at cementing interfaces with the assumption of axisymmetric geometry, isotropic horizontal in-situ stresses and elastic properties for the cement sheath and interfaces.

Zhang, Yan, Yang and Zhao [52] proposed an analytical plain-strain approach to assess the integrity of a wellbore under HPHT conditions by coupling solid-temperature approach. The Mises criterion, Drucker-Prager, and Joint Roughness Coefficient-Joint Compressive Strength (JRC-JCS) were exploited to model the casing, cement sheath and cement interfaces respectively. In their parametric study, they showed that the cement mechanical properties affect the failure coefficient of the casing-cement sheath-formation system significantly. They tried a wide range of 3 GPa to 90 GPa for the cement Young's modulus and 0.1to 0.4 for the cement Poisson ratio. They demonstrated that incorporating cement with low Young's modulus and high Poisson ratio resulted in lower failure coefficient, therefore, it is more favourable to the wellbore integrity.

The assumptions and simplifications made in analytical models such as the aforementioned study may lead to unrealistic results. For instance, failure modes in all directions would not be captured in two-dimensional (2-D) plane strain models. Furthermore, the axisymmetric geometry and the assumed isotropic in-situ stresses do not correctly reflect the real conditions [47].

### 3.1.2. **Cement Sheath: Numerical Modelling**

Numerical modelling has been significantly improved compared to analytical modelling regarding complexity and ability to model wellbore integrity assessment with a high degree of accuracy. The incorporation of appropriate material constitutive law and consequently the evolution of corresponding model parameters are the fundamental stage in developing a numerical model.

To this point, the elastic linear principle was utilised in a few cement integrity studies reviewed as follows. Nabipour, Joodi and Sarmadivaleh [28] simulated downhole stresses using Finite Element Method (FEM) along with sensitivity analyses on casing internal pressure, anisotropic horizontal in-situ stresses, and casing eccentricity. They have used a plain strain model with thermo-elastic material properties, and the interfaces are assumed to be fully bonded. According to this study, the failure of cement and formation bond and the initiation of radial cracks from the inner surface of the cement sheath are the most possible scenarios for losing the cement sheath integrity.

Wang and Taleghani [37] performed a three-dimensional (3-D) poroelastic simulations with a particular focus on the interface modelling to assess the integrity of the interfaces. They also explained the superiority of developing 3-D models in terms of capturing the spatial fracture patterns which may not be completely explained by common two-dimensional axisymmetric models. Since in these 2-D models the failure paths are constrained to the direction parallel to the borehole axis.

Guo, Bu and Yan [49] presented a numerical study to investigate the effect of the heating period, cement thermal expansion, and overburden pressure on the cement integrity under steam stimulation conditions. All materials presumed to be linear elastic. They recommended a moderate heating rate and moderate cement thermal expansion coefficient is beneficial to the cement sheath integrity.

Li, Liu, Wang, Yuan and Qi [48] developed a coupled framework to investigate the effect of non-uniform in-situ stress filed, temperature, and pressure effects on wellbore integrity. The stress states evaluated assuming the linear elastic behaviour for all the materials. According to this study, the anisotropy of in situ stresses resulted in the creation of shear stresses and non-uniform stress distribution within the cement sheath. By increasing the casing temperature, the tensile stresses develop and lead to the creation of fractures in the inner surface of the cement sheath.

De Andrade and Sangesland [66] conducted a numerical study with a special focus on thermal-related load cases. They built a 2-D model and assumed a linear elastic behaviour for all the materials, bonded contact between wellbore components and isotropic in-situ stresses. A utilisation factor based on Mogi-Coulomb criterion was defined to check the state of the stress and estimate cement sheath failure. The utilisation of Mogi-Coulomb criterion instead of Mohr-Coulomb was explained by considering the obtained experimental data by Al-Ajmi [67] which states Mogi-Coulomb criterion represents the state of shear failure in different types of rocks better than Mohr-Coulomb criterion. According to their results, the likelihood of cement sheath damage

and bonding failure is higher in cooling scenarios compared to the heating scenarios. The effect of casing centralisation and controlled heating/cooling rates seemed to be trivial.

The employment of linear elastic theory to simulate the cement sheath behaviour can affect the accuracy and reliability of the results due to the oversimplifications made in finding solutions. The complex response of the cement to different mechanical and thermal loading scenarios cannot be simulated by elastic theory. The obtained stress-strain curves from the isotropic drained compression tests on the cementitious specimens by Bois, Garnier, Rodot, Sain-Marc and Aimard [36] clearly indicate non-linear behaviour. In addition, the existence of the permanent strains upon unloading [36] confirms the incompatibility of linear elastic theory and the necessity of employing plasticity theory in cement integrity evaluations again. Considering that, the elastic theory doesn't incorporate the time-dependency and materials hysteresis law [50].

The non-linear approaches including Von-Mises [51], Drucker-Prager [52], Ottosen model [5, 53], modified Cam-Clay [36], and Mohr-Coulomb / with smeared cracking [31, 44] were incorporated in the cement sheath integrity assessments to lessen the drawbacks of the applied linear models.

Fleckenstein, Eustes and Miller [51] employed the von-Mises criteria and showed that the magnitude of tangential stresses would be significantly reduced if the cement sheath acts as a ductile material with lower Young's modulus and higher Poisson's ratio. The lack of pressure dependency of the von Mises criteria is however problematic in modelling cementitious materials.

Zhang, Yan, Yang and Zhao [52] utilised Drucker-Prager failure criterion in a 2-D model to verify their proposed analytical model. Pattillo and Kristiansen [68] also employed Drucker-Prager criterion on their 2-D model to investigate the integrity of Valhal horizontal wellbores. In both studies, the sources of constitutive model parameters are not detailed. The studies carried out on the performance of Drucker-Prager model shows this model does not provide accurate predictions while one or more principle stresses are tensile stress. Additionally, considering the same effect for $\sigma_2$ and $\sigma_3$ leads to overestimation of rocks' strength and it is not verified by laboratory experimental data [69, 70].

Asamoto, Le Guen, Poupard and Capra [5], Guen, Asamoto, Houdu and Poupard [53] developed a 2-D model using the Ottosen model [71] as a smeared crack model to investigate the softening post-peak behaviour of the cement sheath and the estimation of the crack width in a wellbore subjected to thermal and mechanical loads. In both studies, the details of the constitutive model performance and the relevance of the constitutive parameters to the experimental data are not described.

The modified Cam-Clay model has been suggested as a method to incorporate cement micro cracking mechanisms by Bois, Garnier, Rodot, Sain-Marc and Aimard [36] owing to the nonlinearity of stress-strain curve achieved from the isotropic drained compression tests [72] and heterogeneous nature of cement at the microscale. Although important aspects of materials behaviour (material strength, compression or dilatancy, and critical state of elements under high distortion) are considered in this model, the tensile post-peak material is not incorporated into this framework.

Mohr-Coulomb criterion alone or combined with the smeared cracking model has been used in some studies which are reviewed as follows. One of the models was proposed by Bosma, Ravi, van Driel and Schreppers [44]. They developed a 2-D model considering symmetry geometry for the wellbore. Mohr-Coulomb plasticity combined with smeared cracking description was used to model the cement sheath under compression/shear and tension. The cement sheath interfaces were modelled using interface elements applying a coulomb friction criterion. According to this study, considering only the cement failure envelope in compression as a quality indicator is not acceptable in wellbore integrity modelling. The cement Young's modulus, Poisson's ratio, tensile strength, shear strength, and bonding properties are to be incorporated into the wellbore integrity modelling.

Ravi, Bosma and Gastebled [31] developed a 2-D model to investigate the wellbores integrity subjected to operational procedures. To model the stress state within the cement sheath, the Hookean model was incorporated for undamaged state and combined Mohr-Coulomb plasticity with smeared cracking after exceeding the compressive shear and tensile strength state. According to their findings, the integrity of the cement sheath is highly dependent on the cement and mechanical rock properties, and well-operating parameters. Cement sheath with less stiffness shows more resilient and helps to reduce the risk of cement sheath failure. Petty, Gastineau, Bour and Ravi [73] also used Mohr-Coulomb plasticity combined with smeared cracking in their 2-D model to determine the advantageous cement system with respect to the integrity of the cement sheath within a geothermal well. They showed that foamed cement performs better than the conventional cement while being exposed to pressure-temperature stresses and the effect of shrinkage is also minimised by using foamed cement.

Mohr-Coulomb criterion was also used by Feng, Podnos and Gray [50], Nygaard, Salehi, Weideman and Lavoie [74], and Zhu, Deng, Zhao, Zhao, Liu and Wang [75] to predict the plastic behaviour of the cement sheaths subjected to mechanical and thermal loads.

The combination of Mohr-Coulomb with smeared cracking is one of a few suitable approaches for modelling the real conditions in the cement integrity numerical simulations. However, despite the broad application of Mohr-Coulomb criteria, it has its own limitations. The model assumes a linear relationship between $\sqrt{J_2}$ and $I_1$ in the meridian plane, while this relationship has been experimentally shown to be curved [36, 72, 76, 77], for cementitious materials, particularly at low confinement. The major principal stress $\sigma_1$ and intermediate principal stress $\sigma_2$ are defined independently in Mohr-Coulomb model which results in an underestimation of the yield strength of the material and, it is not in a good agreement with experiments in which the effect of $\sigma_2$ is being considered. The shape of the yield surface in the deviatoric plane is an asymmetrical hexagon, whereby the sharp corners can hinder convergence in numerical simulations [70, 78]. Moreover, quasi-brittle materials experience a huge volume change due to a large amount of inelastic strains (dilatancy) which has been overlooked so far by using associated flow rules in the aforementioned modelling approaches of the cement. The associative plastic flow rules tend to lead to poor results in dilatancy evolution [55].

The application of plasticity theory in compression (Mohr-Coulomb) combined with the fracture mechanics models such as smeared cracking presents some drawbacks as well. Given that, smeared crack models in finite element analysis can often be problematic in terms of "mesh alignment sensitivity" or "mesh orientation bias" which indicates that the orientation of smeared crack depends on the discretization orientation [79]. It is worth adding that the mesh regularization approach proposed by [56] (crack band theory) in the smeared cracking model has been successful for predicting mode I fractures while the extension of this approach to mixed-mode failure and three-dimensional stress state is hard [79].

Considering the limitations, it would be more practical to employ more suitable models with respect to their accuracy (enrichment) and reliability (capability to reproduce the experimental data) along with their efficiency (mesh orientation and mesh size objectivity) [79].

The observed non-linearity in cement behaviour [36, 72] results from two different microstructural changes which happen in the materials while subjected to different loading conditions. One is plastic flow causes the permanent deformation and the second is the development of microcracks which leads to elastic stiffness degradation [80]. Therefore, it a necessary to apply a model which combines plasticity and damage mechanics. For this reason, the formation of microcracks which is also characterized by softening behaviour of the materials is difficult to explain using classical plasticity models [55]. The damage mechanism is described by two physical aspects corresponding to the two modes of cracking ( hardening and softening) [80].

Therefore, in this study, Concrete Damage Plasticity (CDP) model developed by [54] and then modified by [55] has been employed. The Concrete Damage Plasticity model combines plasticity and damage mechanics and uses the concept of fracture-based damage. In the modified revision, two damage variables one for compressive damage and one for tensile damage incorporated to consider different states of damage. This feature is capable of describing the induced anisotropy of microcracking which also facilitates the numerical implementation procedures [80]. The pressure-sensitive yield criterion accompanied by employing the dilatancy (non-associated flow rule), makes this model more suitable than the others that have been employed in the assessment of cement sheath integrity.

### 3.1.3. Cement Sheath Interfaces Modelling

The cement sheath interfaces with the casing and the formation are recognized as the weakest link and the most potential area for defects and debonding issues which leads to losing the cement sheath integrity [37, 81].

The delamination mechanism is one of the most uncertain aspects of wellbore integrity simulations due to its complex nature [82]. So far, different modelling approaches have been undertaken to simulate the behaviour of the cement sheath interfaces. Bosma, Ravi, van Driel and Schreppers [44] modelled the behaviour of the interface by interface elements using the Coulomb friction failure criterion, and the elastic stiffness of the contact elements was chosen considerably higher than that of the surrounding material. Guen, Asamoto, Houdu and Poupard [53] employed Mohr-coulomb failure criterion for the interface modelling. The details of obtaining the process of the corresponding parameters for the interfaces are not elaborated upon. The use of Mohr-Coulomb criterion may not be substantially appropriate due to the complicated behaviour of the interfaces. The delamination may occur at the mixed-mode conditions and not only within pure compression/shear condition.

Zhang, Yan, Yang and Zhao [52] incorporated the non-linear criterion knows as Joint Roughness Coefficient- Joint Compressive Strength (JRC-JCS) which was originally developed by Barton and Choubey [83] for joint rock analysis. The corresponding parameters were taken from the literature from the rock analysis which may not be accurate to be used at the cement sheath interfaces modelling.

The most recent and successful cement sheath interface modelling was carried out by Wang and Taleghani [37]. They modelled the interfaces by incorporating the cohesive theory to simulate the initiation and propagation of debonding at the interfaces. They performed an inverse analysis on the experimental results performed by Carter and Evans [84], Ladva, Craster, Jones, Goldsmith

and Scott [85], Evans and Carter [86] to determine the corresponding parameters of the cohesive criterion.

Evans and Carter [86] designed a push-out test setup to measure the cement shear bond and hydraulic bond to the casing and the formation. Carter and Evans [84] continued their experimental work and identified more influential factors on the cement bonding properties to the casing. They designed cylindrical chambers in which shear bond is determined by applying force to instigate the movements of the casing surrounded by cement. The shear bond measured as dividing the force to the contact surface area. The cement hydraulic bond is determined as the cement bond to the casing and the formation which prevent the fluid migration. Hydraulic bond is determined by applying pressure to the cement interfaces until leakage happens.

As mentioned, the approach proposed by Wang and Taleghani [37] to model the cement sheath interfaces behaviour with cohesive elements has been very successful in numerical simulations. Therefore, their approach has been applied in this thesis along with minor alterations. In this research. the interfaces are modelled using "surface-based cohesive behaviour" instead of cohesive elements. The surface-based cohesive behaviour defines as a surface interaction property with traction transferring capacity between master and slave surfaces. The cohesive constraint is enforced at each slave node for cohesive surfaces. Therefore, for cohesive surfaces, refining the slave surface in comparison with the master surface will result in the improved constraint satisfaction and more accurate results than using cohesive elements [87]. In addition to providing mesh generation flexibility at each side of the interfaces. Moreover, the employment of surface-based cohesive behaviour instead of cohesive elements complies with the incorporation of the temperature transmitting capabilities at the interfaces to overcome the limitation of the nonexistence of temperature degree of freedom in cohesive elements.

## 3.2. Laboratory Experiments on Cement Properties

In 1992, Goodwin and Crook [32] performed laboratory investigations to simulate conditions at which the cement sheath failure occurs. They built a prototype consisting of an inner casing, outer casing, and the annulus filled with cement. They observed sudden exposure to excessive internal pressure and temperature result in radial and circumferential casing expansion. The diametrical and circumferential forces create radial and shear forces within the cement sheath and at the interface of cement with the casing.

Afterwards, the researchers attempted to incorporate the predictive models to simulate the failure scenarios. However, the incompleteness of cement class G mechanical parameters inventory corresponding to curing condition was an obstacle for them to carry on with their

modelling approaches. Considering that, the mechanical properties of the cement are significantly dependent on the curing conditions, which vary along its depth and its exposure to formation fluids [20, 88, 89]. Subsequently, many laboratory tests have been carried out on well cement to determine the key parameters for modelling purposes reviewed in the following sections.

### 3.2.1. **Cement Mechanical Properties**

Thiercelin, Dargaud, Baret and Rodriquez [63] presented an experimental study utilising cement class G with varieties of additives to determine the material's flexural and compression strength, and Young's modulus in flexion and compression. The tensile properties were obtained using three-point bending tests on 30×30×120 mm prisms, with a loading rate of 0.01 cm/min. The compressive properties were measured via uniaxial compression tests on 50.8×50.8×50.8 mm (2×2×2 in) cubes. The volume of additives, curing conditions, and slurry density were different for each test. Therefore, it is difficult to associate any differences in mechanical properties with one specific factor.

Bosma, Ravi, van Driel and Schreppers [44] carried out confined and unconfined compression tests to obtain cement mechanical properties for their modelling. However, they did not publish the experimental details and the outcomes.

Reddy, Santra, McMechan, Gray, Brenneis and Dunn [90] used acoustic measurements to compare dynamic cement mechanical properties with static mechanical properties. They used cylindrical samples with the size of 50.8×102 mm (2×4 in) and cured them under pressure of 20.7 MPa (3000 psi) and temperature of $88^{o}C$ for 72 hrs in an autoclave and cooled down to room temperature and also depressurized slowly. They performed confined and unconfined compression tests. However, the results of confined compression tests haven't been published. Their observations showed the importance of the time period to achieve long-term mechanical properties and found a correlation between static and dynamic mechanical properties, i.e. dynamic modulus values were 1.6 times higher than the static values.

Roy-Delage, Baumgarte, Thiercelin and Vidick [91] planned a slurry formulation with cement class G to achieve highly durable cement. They cured the samples at $77^{o}C$ and $114^{o}C$ with a pressure of 20.7 MPa (3000 psi) for three days or upon reaching a constant compressive strength. Three-point bending tests and crushing tests were performed on 30×30×120 mm and 50.8× 50.8× 50.8 mm (2× 2× 2 in) cubes, respectively. This study showed that cement cured at the higher temperature ($114^{o}C$) has a higher Young's modulus and uniaxial compressive strength but a lower Modulus of rupture in flexure.

Nasvi, Ranjith and Sanjayan [92] used cylindrical samples with the size of 50 ×100 mm to measure the uniaxial compression strength of cement class G. The samples were oven cured at different temperatures between $30^0$C to $80^0$C for 24 hours excluding the samples required to be cured at room temperature. Afterwards, all of the samples were kept at ambient temperature for another 48 hours. Their results demonstrated that samples that cured at $60^0$C had the maximum uniaxial compressive strength of 53 MPa, but that samples cured above this temperature presented a lower uniaxial compressive strength. The Young's modulus of cement class G is higher at lower curing temperatures and reaches its maximum value at the curing temperature of $40^0\ C$.

James and Boukhelifa [93] provided a comprehensive review on the published experimental studies and recommended a set of measurements methods to determine cement mechanical parameters (Young's modulus, Poisson's ratio, unconfined compressive stress (UCS), and tensile strength) as inputs for wellbore integrity models and they validated their approach by filed evaluation at actual wells. They suggested using suitable load frame equipment with controllable load and displacement rates. Based on their results Young's modulus and the Poisson's ratio are independent of confining stress. They believed that Brazilian tests estimate the cement tensile strength 50%-75% higher than the actual value. Therefore, the commonly employed rule-of-thumb estimation for tensile strength (tensile strength= 10% of UCS) substantially adds more safety factor to the estimations.

Guner and Ozturk [94] measured both uniaxial compressive strength and Young's modulus at different cement curing periods of 2, 7, and 14 days. They concluded increasing the curing time enhances the mechanical properties of cement by 2-3 times.

Teodoriu and Asamba [95] investigated the effect of salt concentration on cement class G properties by performing uniaxial compression tests on cubic samples with the size of 50.8× 50.8× 50.8 mm (2× 2× 2 in). They cured samples in water in atmospheric condition for 24hrs and then was placed in an autoclave for curing period of one to seven days under two different conditions ($30^o$C and 10 MPa / $150^o$C and 20 MPa). They also measured the compressive strength of samples cured at the atmospheric condition at the age of 21 days. Their results of the batch without salt (0% BWOW-By weight of Water) with respect to the first curing condition were summarised in Table 3.1 for comparison purposes. They showed the samples with 5% ± 2.5% salt concentration curing at atmosphere to moderate temperature yield the maximum compressive strength among all the other samples with different salt concentration curing at different conditions.

Romanowski, Ichim and Teodoriu [96] compared two methods for measuring the cement compressive strength (ultrasonic pulse velocity versus mechanical method). The tests were

performed at different curing times on cement class G, cement class G with bentonite, and cement class G with other additives. They demonstrated that the outcomes of ultrasonic methods should be calibrated using the mechanical (destructive) measuring methods. The importance of achieving an extensive database on wellbore cement was emphasised as well.

Latest studies in oil and gas cementing technology emphasis that cement sheath mechanical failure occurs not only because of imposed compressive stresses but also because of tensile stresses [97]. However, there are no API guidelines for measuring the tensile properties of cement, and ASTM standards for the measurement of tensile properties of concrete present various weaknesses when applied to cement tensile tests. As, these standards have been designed for cement at locations only a few meters down the ground and they don't incorporate the curing conditions with respect to high pressure and high temperature in harsh conditions, i.e. downhole conditions [97, 98].

Heinold, Dillenbeck and Rogers [97] cured samples made of cement class G plus additives in a standard high-pressure high-temperature (HPHT) curing chamber, under a pressure of 20.7 MPa at two different temperatures of $37.8^{o}C$ and $93.3^{o}C$ for 72 hours. They performed uniaxial compression tests, flexural strength tests, and tensile strength tests on 50.8×50.8×50.8 mm (2×2×2 in) cubes., 40.6×40.6×160.02 mm (1.6×1.6×6.3 in) prismatic specimens, and dog bone specimens, respectively. They showed that the correlation between unconfined compression strength and tensile strength (empirical relations) does not always apply. According to their results, samples cured at a higher temperature ($93.3^{o}C$) demonstrated lower flexural strength and higher tensile strength. Heinold, Dillenbeck, Bray and Rogers [99] continued this study by curing samples at two different temperatures of $54.4^{0}C$ or $82.2^{0}C$ for 48 hours in an atmospheric water bath. The authors compared the results of splitting tensile strength (STS) tests with direct tensile tests on the dog-bone sample. The splitting tensile strength test results overestimated the tensile properties of cement class G by order of 1.5 to 2.5. However, direct tensile test measurements were also impacted by stress concentrations on the samples at or near grip points, which may cause the premature breakage of the samples.

Dillenbeck, Boncan, Clemente and Rogers [98] performed uniaxial tensile tests on dog-bone samples made of cement class H and additives to measure its uniaxial tensile strength. They developed a new testing machine to simulate downhole conditions in a wellbore during curing and performed tensile tests on dog-bone samples. The results showed that the uniaxial tensile strength of the cement samples was highly dependent on the stress loading rate. Therefore, the authors

addressed the necessity of developing a standard loading rate at which to perform cement tensile tests.

Quercia, Chan and Luke [100] characterised the tensile strength of cement class G using the Weibull statistics method [101], by performing direct tensile tests on dog-bone samples, and Brazilian tests on cylindrical samples. Weibull statistics is a characterization tool which defines the scatter in strengths along with strength variations due to sample size and provides more confidence and reliability in risk analysis. The samples were made of cement class G and micro-fibres. The samples were initially cured in a pressurised chamber for 24 hours at $25^0C$ and 10.34 MPa (1500 psi) and then demolded and cured underwater for six days. The authors also used modified dog-bone molds, which act as holders to avoid grip concentration points.

Table 3.1 and 3.2 respectively summarises the results of unconfined compression tests and tensile tests studied on cement class G and H available in the literature.

*Table 3.1: Compressive Measurements Retrieved from the Available Literature*

| Reference | Sample shape | Curing Temperature ( $^0$ C) | Curing Pressure (MPa) | Curing Time (days) | Compressive Strength (MPa) |
|---|---|---|---|---|---|
| Roy-Delage, Baumgarte, Thiercelin and Vidick [91] |  | 77 | 27 | 3 | 37 |
| Roy-Delage, Baumgarte, Thiercelin and Vidick [91] |  | 114 | 20.7 | 3 | 39.2 |
| Morris, Criado, Robles and Bianchi [102] |  | 84 | 27 | 2 | 36.9 |
| Guner and Ozturk [94] |  | ambient | ambient | 3 | 49 |
| Nasvi, Ranjith and Sanjayan [92] |  | 60 | – | 3 | 53 |
| Nasvi, Ranjith and Sanjayan [92] |  | ambient | ambient | 3 | 27 |
| Teodoriu, Kosinowski, Amani, Schubert and Shadravan [20] |  | 65 | – | 1 | 36 |
| Teodoriu, Kosinowski, Amani, Schubert and Shadravan [20] |  | ambient | ambient | 3 | 48 |
| Teodoriu, Kosinowski, Amani, Schubert and Shadravan [20] |  | 65 | – | 14 | 64 |
| Teodoriu, Kosinowski, Amani, Schubert and Shadravan [20] |  | 100 | 18 | 14 | 47 |
| Yuan, Teodoriu and Schubert [103] |  | ambient | ambient | 14 | 55.7 |
| Yuan, Teodoriu and Schubert [103] |  | 75 | ambient | 14 | 60.8 |
| Yuan, Teodoriu and Schubert [103] |  | 100 | 18 | 14 | 56.7 |
| Labibzadeh, Zahabizadeh and Khajehdezfuly [104] |  | ambient | ambient | 1 | 10.95 |
| Labibzadeh, Zahabizadeh and Khajehdezfuly [104] |  | ambient | ambient | 2 | 16.55 |

| | | | | | |
|---|---|---|---|---|---|
| Labibzadeh, Zahabizadeh and Khajehdezfuly [104] |  | 38 | 2.8 | 2 | 14.24 |
| Labibzadeh, Zahabizadeh and Khajehdezfuly [104] |  | 68 | 17.2 | 2 | 12.72 |
| Labibzadeh, Zahabizadeh and Khajehdezfuly [104] |  | 82 | 41.4 | 2 | 18.82 |
| Labibzadeh, Zahabizadeh and Khajehdezfuly [104] |  | 121 | 51.7 | 2 | 16.4 |
| Labibzadeh, Zahabizadeh and Khajehdezfuly [104] |  | 149 | 51.7 | 2 | 4.59 |
| Teodoriu and Asamba [95] |  | 30 | 10 | 1 | 2 |
| Teodoriu and Asamba [95] |  | 30 | 10 | 3 | 18 |
| Teodoriu and Asamba [95] |  | 30 | 10 | 7 | 28 |
| Teodoriu and Asamba [95] |  | ambient | ambient | 21 | 42 |

As can be seen in Table 3.1, the cement class G mechanical inventory lacks triaxial compressive properties in general and uniaxial compressive properties corresponding to the different curing temperatures, particularly in long-term curing periods.

It is also should be noted that the pre-peak and post-peak behaviour in the stress-strain graphs vary according to different specimen size and shape [105]. Table 3.1 shows the majority of studies were performed on cubic samples. While cylindrical specimens might be more suitable to be employed since cube tests provide higher values (the uniaxial strength measured using sufficiently slender specimens is usually around 70%-90% of the cube strength [106]). In cubic samples, the restraining effect of the platens spreads over the total height of a specimen, but in cylindrical samples, some parts of specimens stay unaffected [107]. Another problem regarding experiments using cubes is that the post-peak behaviour is milder, therefore, requires more energy consumption than using cylinders. The effect of size specimen is also larger for cubic samples [105].

Consequently, the experimental aspect of this thesis (Chapter 6), aims to add the discussed missing values to the cement class G mechanical inventory; the uniaxial and triaxial compression tests were performed on cylindrical samples cured at two different curing temperatures.

*Table 3.2: Tensile Measurements Retrieved from the Available Literature*

| Reference | Sample shape | Additives | Curing Temperature ($^0C$) | Curing Pressure (MPa) | Curing Time (days) | Flexural Tensile strength (MPa) | Tensile strength (MPa) | Splitting Tensile (MPa) |
|---|---|---|---|---|---|---|---|---|
| Thiercelin, Dargaud, Baret and Rodriguez [108] |  | Latex (2 gps) | 134.4 | 20.68 | 3 | 7.24 | – | – |
| Roy-Delage, Baumgarte, Thiercelin and Vidick [91] |  | – | 77 | 20.68 | 3 | 8.46 | – | – |
| Heinold, Dillenbeck and Rogers [97] |  | – | 37.8 | 20.68 | 3 | 3.43 | 1.83 | – |
| Heinold, Dillenbeck and Rogers [97] |  | Defoamer 0.02 gal/sk | 93.33 | 20.68 | 3 | 1.4 | 2.31 | – |
| Heinold, Dillenbeck, Bray and Rogers [99] |  | Defoamer 0.02 gal/sk | 54.4 | Ambient Pressure | 2 | 7.48 | 2.75 | 4.68 |
| |  | | | | | – | – | – |
| Heinold, Dillenbeck, Bray and Rogers [99] |  | Defoamer 0.02 gal/sk | 82.2 | Ambient Pressure | 2 | 7.52 | 2.58 | 5.75 |
| |  | | | | | – | – | – |
| Quercia, Chan and Luke [100] | 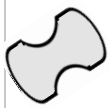 | Defoamer 0.02 gal/sk | 25 | 10.34 | 1 | – | 2.88 | 3.38 |
| |  | | Ambient Temperature | Ambient Pressure | 6 | – | – | – |

The main problem with performing tensile measurement test is there are no API guidelines for measuring the tensile properties of cement, and ASTM standards for the measurement of tensile properties of concrete present various weaknesses when applied to cement tensile tests. This is because, these standards have been designed for cement at locations only a few meters down the ground and they do not incorporate the curing conditions considering downhole conditions in

regards to high pressure and high temperature in harsh conditions, i.e. downhole conditions [97, 98].

Table 3.2 demonstrates that the measurement of tensile strength and particularly the fracture energy of cement class G, in particular over long-term periods, were simply overlooked in many experimental studies.

Subsequently, in the experimental aspect of this study, three-point bending tests were performed on notched and un-notched beams to measure the tensile strength and fracture energy. The splitting tests and direct tensile tests were avoided due to their overestimated results and stress concentrations issue on the direct test samples at or near grip points (point loading), which provides high potential for immature breakage of the samples [97].

### 3.2.2. **Cement Thermal Properties**

Bentz [109] measured heat capacity and thermal conductivity of hydrated cement paste with the help of a transient plane source method as a function of water to cement ratio, curing condition, and degree of hydration. Samples were cured under sealed and saturated conditions. The pattern for both is almost the same. In the early stages of hydration, heat capacity was decreased and then stabilized to a constant value. Additionally, it can be understood that there is a little deviation in the thermal conductivity of samples due to the degree of hydration and curing condition.

Because of the enhanced oil recovery process, i.e. steam-assisted gravity drainage or cyclic steam stimulation, the temperature of wells can raise to $350^0$ C [95]. Considering this situation, the linear coefficient of thermal expansion (LCTE) is an important factor to simulate the coupling effect of thermal and mechanical effects on the well integrity failure. Based on this factor the position of the cement-failure zone and cement integrity zone can be varied [110]. According to Loiseau [110], LCTE is a function of chemical components and oil well cement curing temperature. Additionally, the LCTE becomes more of an influential factor as the temperature of the bottom hole of wells changes drastically. They stated some precautions to measure LCTE precisely and also investigate the effects of chemical compositions and temperature on LCTE. The LCTE of net cement was measured as 9.10 $\mu/{}^{o}C$ .

Nygaard, Salehi, Weideman and Lavoie [74] measured the cement thermal conductivity using divided-bar apparatus and the cement specific heat capacity using steel-frame equipment consisted of one LVDT and a glass beaker filled with water.

Considering the limitations in the literature review, it would be more realistic to perform the three-dimensional simulations to be able to predict the fracture initiation and propagation in

different directions along with employing more suitable model for the cement sheath as a geo-material, and the implementation of detrimental factors. Figure 3.1 shows these factors which have influential contributions on the cement sheath integrity assessment.

Thus, in this study, Concrete Damage Plasticity model will be employed to predict the non-linear behaviour of the cement sheath while subjected to pressure and temperature variations by differentiating the response of the material in compression and tension state. The pressure-sensitive yield criterion accompanied by incorporation of the dilatancy (non-associated flow rule), stiffness degradation, and capability to reproduce experimental data make this model a more appropriate than the rest ones in cement sheath integrity assessments (Chapter 5 and 7). Experimental investigations were carried out to determine the constitutive model parameters on cement class G mechanical properties missing in the inventory (Chapter 6).

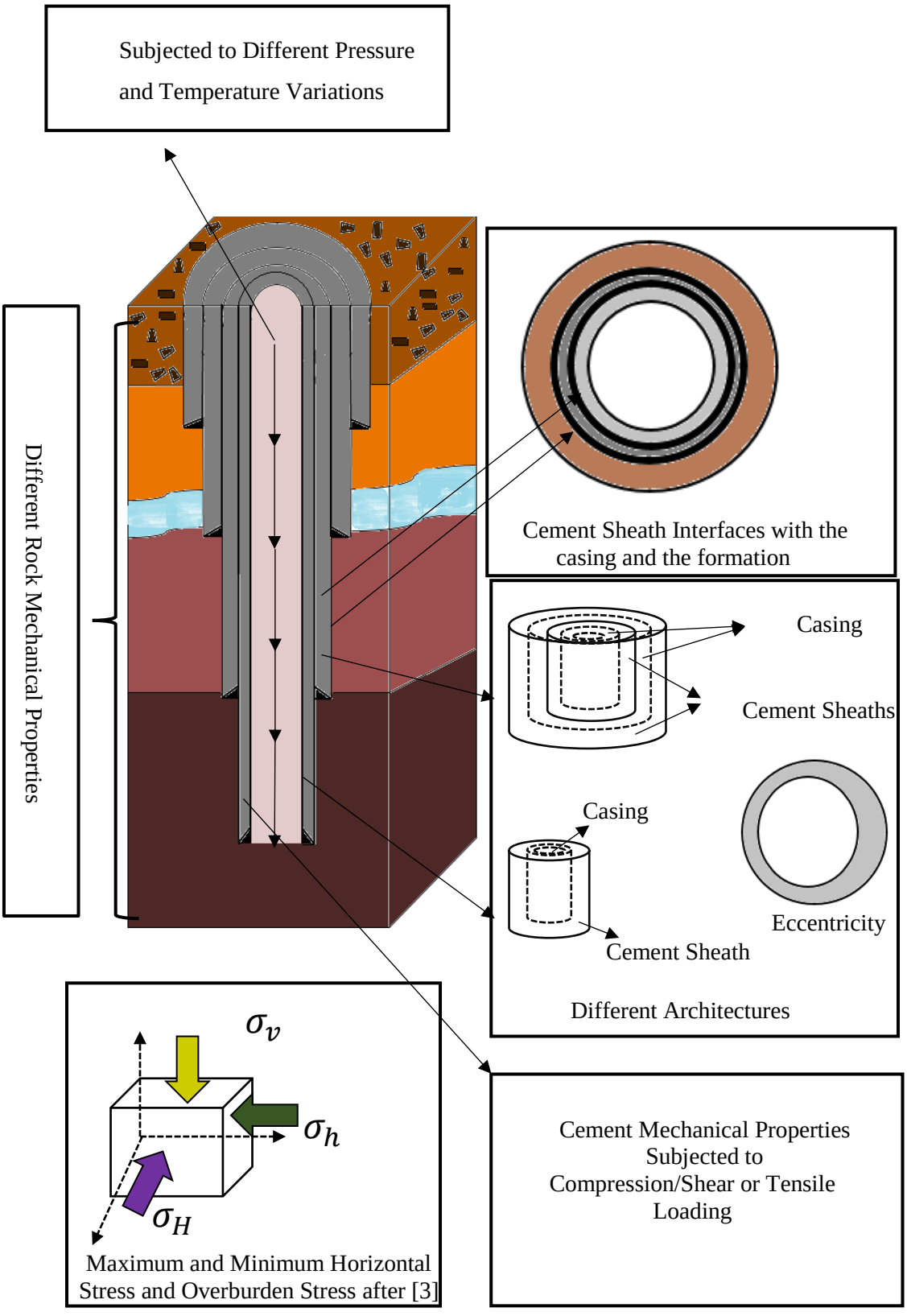


Figure 3.1: Different Contributing Factors in Well (wellbore schematic is after [2]) Integrity Simulations

# 4. Research Objectives

The overall objective of this study is to improve the modelling capabilities to assess cement sheath integrity by employing a more suitable constitutive model for the cement sheath. The experimental outcomes on the behaviour of the cement-based specimens under compression tests showed a strong non-linearity in the obtained stress-strain curve which confirms the necessity of applying plasticity theories. However, it is difficult to describe the elastic stiffness degradation of the cement-based materials which occurs during experiments by using the classical plasticity theories. Therefore, in this study, Concrete Damage Plasticity (CDP) model developed by [54] and then modified by [55] has been applied. The Concrete Damage Plasticity model combines plasticity and damage mechanisms and is particularly formulated for modelling geo-materials such as rocks, concrete, and cementitious materials by considering two different tensile and compressive damage variables. Considering that, the response of geo-materials in compression and tension is very different. The yield criterion in the CDP model also represents the pressure-dependency of the materials behaviour under shearing at different levels of confinement in addition to the incorporation of non-associated flow rule (material dilatancy). Based on the above discussion, the CDP model can be considered a very suitable model for the wells cement under different loading conditions in wellbore integrity assessments.

However, the incompleteness of cement class G mechanical parameters inventory, e.g. lack of experimental data under different confining pressure and tensile properties, was an obstacle to perform accurate simulations. For instance, the confined (triaxial) compression tests data are required to approximate the shape of the shape of yield / and failure surfaces. The measurement procedures of cement tensile strength properties and fracture energy required to simulate the tensile behaviour mechanism are not consistent. Moreover, the effect of curing temperature on the cement long-term mechanical properties was also missing from the literature.

Therefore, this study aims to add these cement mechanical properties to the cement class G inventory as well. The data and analyses added to the cement class G inventory are as follows. The investigations of the curing temperature and pressure confinements effects on the strength and post-peak response of the cement class G under compression. In addition, in the absence of API guidelines for measuring the cement tensile properties, the methods for measuring cement tensile and / flexural strength were not consistent, and the measurement of cement fracture energy was mostly overlooked.

As a final point, this research leads to better cement sheath integrity evaluations subjected to pressure and temperature variations using the CDP model along with the incorporation of

calibrated constitutive parameters obtained from the experimental data. The connections between the research aims and the associated publications are discussed as follows.

## 4.1. Objective 1:

**Evaluation of Cement Sheath Integrity Subject to Enhanced Pressure (Paper-1)**

The cement sheath should be designed and placed in a way to resist the imposed stresses from wellbore operational procedures. In this paper, the effect of elevated pressure on the cement sheath integrity was investigated.

The key objective of this paper was the incorporation of a suitable constitutive model (Concrete Damage Plasticity) for the cement sheath in wellbores. The CDP model especially formulated for modelling geo-materials including rocks, and cement-based materials by considering the difference in tensile and compressive material responses, the pressure-dependent material behaviour under shearing at different levels of confinement, and the martial dilatancy. Therefore, it is advantageous in terms of its capabilities to predict both cement sheath compression/shear and tensile mechanical failure in wellbores.

To determine the corresponding constitutive model parameters, uniaxial compression tests, three-point bending tests on specimens manufactured from class G well cement, and experimental data calibration and validation should be performed.

The integrity of the cement sheath should be assessed in relation to the local and global compression (crushing) or tensile (cracking) damage indicators within the cement sheath.

The interfaces should be properly modelled to investigate the effect of elevated pressure on the creation of micro-annulus (de-bonding occurrence) as well. Thus, the surface-based cohesive approach was employed.

To investigate the effect of different influential factors including the orientation and the anisotropy of in-situ stresses, and different stiffness's of rocks on the cement sheath integrity, sensitivity analyses should be performed.

## 4.2. Objective 2:

**Effect of Curing Conditions on the Mechanical Properties of Cement Class G with the Application to Wellbore Integrity (Paper-2)**

The paucity of experimental data is an obstacle for cement sheath integrity modelling, for instance, to determine the shape of yield / and failure surfaces the experimental data obtained from confined (triaxial tests) over a wide range of confinement are required. Additionally, the cement tensile properties including the tensile/flexural strength and fracture energy are required to

simulate the tensile behaviour mechanism. However, in the absence of API guidelines for measuring the cement tensile properties, the methods for measuring cement tensile and / flexural strength were not consistent, and the measurement of cement fracture energy was mostly ignored. The effect of curing temperature on the cement long-term mechanical properties was also missing from the available literature. This paper aims to fill these gaps and expand the cement class G mechanical inventory.

The specimens made out of cement class G cured at two different temperatures ($30^{o}$ C and $70^{o}$ C). The unconfined (uniaxial), confined (triaxial) compression tests and three-point bending tests were performed to measure the corresponding cement mechanical properties.

The suitability and reliability of the intended parameters should be calibrated and validated by the numerical simulations of experiments.

### 4.3. Objective 3:

**Evaluation of Cement Sheath Integrity Reflecting Thermo-Plastic Behaviour of the Cement Sheath in Downhole Conditions (Paper-3)**

The objective of this study was to investigate the effect of pressure and temperature variations on the cement sheath integrity employing CDP model along with the determined corresponding constitutive parameters from the previous experimental studies for the cement sheath.

The integrity of the cement sheath should be assessed in relation to the creation of compression (crushing) / tensile (cracking) damage within the cement sheath considering different thermal-mechanical loading scenarios.

The interfaces should be modelled in a way to convey the traction-separation capacity (cohesive behaviour and damage evolution law) and thermal conduction simultaneously.

The effect of different heating/cooling rates along with different wellbore architectures and different degrees of eccentricities should be investigated to reflect the realistic situations in wellbores.

The connections between the research aims and associated publication are summarised in Figure 4.1.

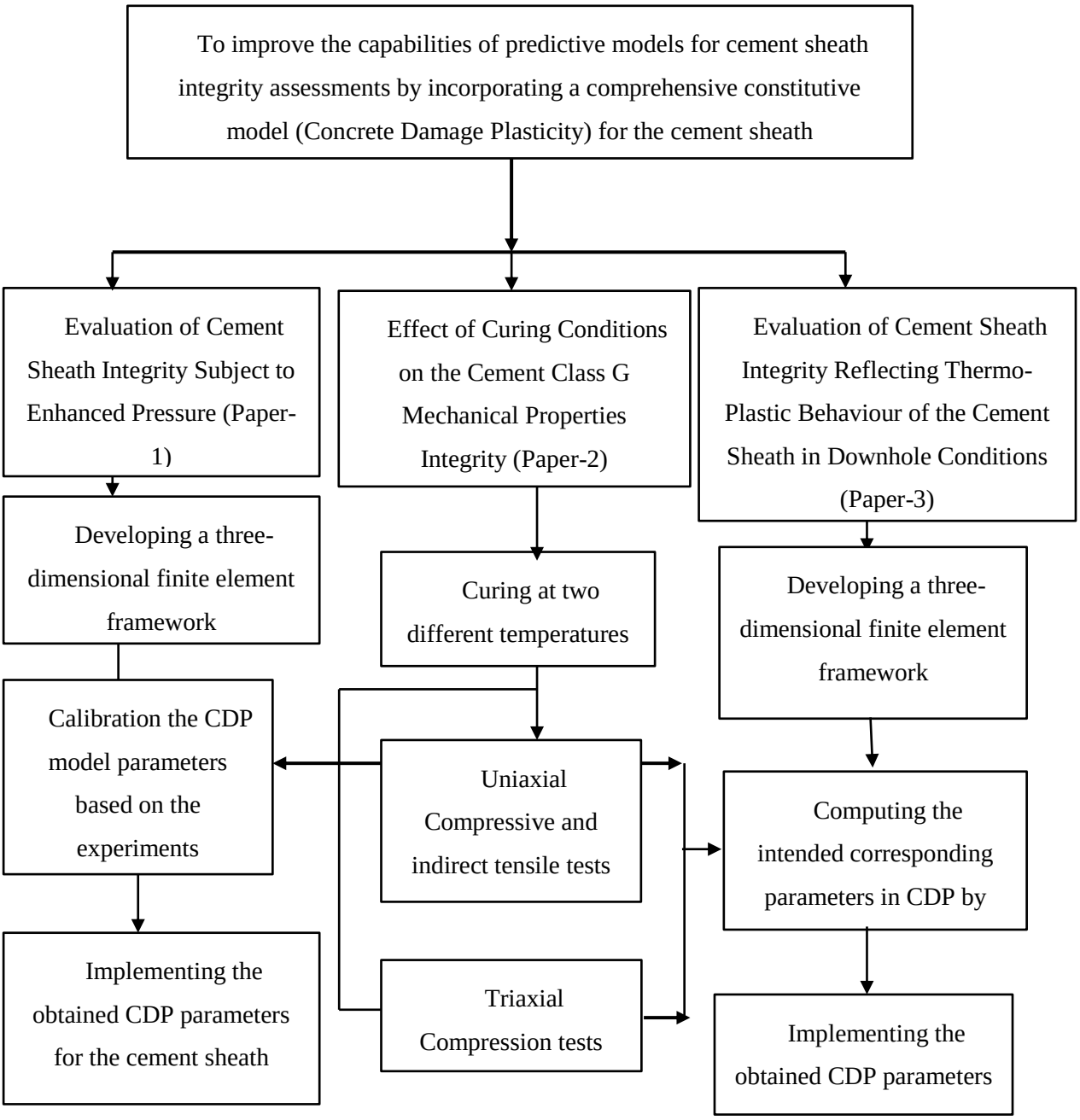


Figure 4.1: The Linkage between Research Objectives (Publications)

# 5. Evaluation of Cement Sheath Integrity Subject to Enhanced Pressure (PAPER-1)

E. Arjomand, T. Bennett, G.D. Nguyen, Evaluation of cement sheath integrity subject to enhanced pressure, Journal of Petroleum Science and Engineering, 170 (2018) 1-13.

# Statement of Authorship

| | |
|---|---|
| Title of Paper | Evaluation of Cement Sheath Integrity Subject to Enhanced Pressure |
| Publication Status | ☑ Published ☐ Accepted for Publication<br>☐ Submitted for Publication ☐ Unpublished and Unsubmitted work written in manuscript style |
| Publication Details | E. Arjomand, T. Bennett, G.D. Nguyen, Evaluation of cement sheath integrity subject to enhanced pressure, Journal of Petroleum Science and Engineering, 170 (2018) 1-13. |

## Principal Author

| | | | |
|---|---|---|---|
| Name of Principal Author (Candidate) | Elaheh Arjomand | | |
| Contribution to the Paper | Development of finite element frameworks, implementation of constitutive modelling, results interpretation, and manuscript preparation. | | |
| Overall percentage (%) | 85% | | |
| Certification: | This paper reports on original research I conducted during the period of my Higher Degree by Research candidature and is not subject to any obligations or contractual agreements with a third party that would constrain its inclusion in this thesis. I am the primary author of this paper. | | |
| Signature | | Date | 25-06-2018 |

## Co-Author Contributions

By signing the Statement of Authorship, each author certifies that:

i. the candidate's stated contribution to the publication is accurate (as detailed above);

ii. permission is granted for the candidate in include the publication in the thesis; and

iii. the sum of all co-author contributions is equal to 100% less the candidate's stated contribution.

| | | | |
|---|---|---|---|
| Name of Co-Author | T. Bennett. | | |
| Contribution to the Paper | Conception of the research<br>Analysis of the results<br>Drafting and editing of the manuscript | | |
| Signature | | Date | 25/6/2018. |

| | | | |
|---|---|---|---|
| Name of Co-Author | G. Nguyen | | |
| Contribution to the Paper | Analysis of results & editing the manuscript | | |
| Signature | | Date | 25/06/2018. |

Please cut and paste additional co-author panels here as required.

# Evaluation of Cement Sheath Integrity Subject to Enhanced Pressure (PAPER-1)


## ABSTRACT

Well-cementing (cementation) is an influential stage of a wellbore completion, as the cement sheath is responsible for providing complete zonal isolation. Therefore, it is of utmost importance to understand the cement mechanical failure mechanisms since well cement failure and interfacial debonding between the cement and casing and cement and rock formations can lead to a barrier failure. During the wellbore lifetime, a cement sheath is subjected to pressure loading variations. This paper demonstrates the results of an experimental-numerical study to investigate the cement sheath integrity after being subjected to an enhanced pressure. A constitutive model specifically formulated for the modelling of quasi-brittle materials is applied to the investigation of cement sheath integrity, incorporating both compression and tensile damage mechanisms. Laboratory experiments are carried out to obtain strength properties of cement class G followed by calibration of the model parameters based on the obtained experimental results. A three-dimensional finite element framework employing the constitutive model for cement sheath and a surface-based cohesive behaviour for the interfaces is developed for integrity investigations. The effects of different orientations of in-situ stresses, different stiffness's of surrounding rock, and the eccentricity of the casing within the wellbore on the integrity of the cement and interfaces are investigated. The significance of cement sheath centralisation and elevated risk of cement mechanical failure caused by wellbore operations in anisotropic fields with soft rocks formation were highlighted. Furthermore, the relatively high magnitude of tensile damage (cracking index) within the cement sheath confirms the importance of tensile properties to be incorporated into the constitutive modelling.



Keywords: cement sheath integrity, concrete damage plasticity model, casing eccentricity, anisotropic in-situ stresses, compression damage, tensile damage


### 5.1. Introduction

Four million onshore hydrocarbon wells have been drilled worldwide [9], with nearly 10000 in Australia alone (from data retrieved from Geoscience Australia) [9]. The cement placed in the annular gaps between casing strings and the formation is a key barrier to provide zonal isolation and maintain the integrity of the wellbore [111]. The integrity of the annular cement and cement interfaces has the potential to be compromised in each of the wellbore operations, including but not limited to, continuous drilling operations, completion operations, stimulation treatments, pressure integrity testing (PIT), and production processes [112]. Therefore, understanding of

cement failure mechanisms under different operating conditions is of the utmost importance for better assessment of wellbore integrity.

Failure of the cement sheath within a wellbore is affected and governed by material mechanical properties (cement compressive strength [31, 44, 45], Young's modulus [31, 44, 45], tensile strength [46], and bond strength [47]), loading conditions (in-situ stresses [44, 46, 48]), cement history (cement shrinkage) [8], and also wellbore architecture (cement sheath diameter, formation properties, cement sheath eccentricity, and wellbore deviation [8, 37]).

Mechanical integrity models investigated to this point can be categorised into analytical models and numerical models. Analytical methods are generally performed by applying simplified assumptions to facilitate finding solutions. The accuracy of analytical models and subsequently their solutions are limited to the correctness and suitability of their initial assumptions and simplifications. Thiercelin, Baumgarte and Guillot [113] modelled the stress state within the cement sheath assuming the linear-elastic properties for cement, axisymmetric geometry, and fully bonded or unbound situations for the interfaces. Shi, Li, Guo, Guan and Li [65] estimated the initial radial and tangential stresses at cementing interfaces with the assumption of axisymmetric geometry, isotropic horizontal in-situ stresses and elastic properties for the cement sheath and interfaces. Honglin, Zhang, Shi and Xiong [64] proposed a model using Mohr-Coulomb criterion and multi-layer thick wall theory assuming plane strain conditions, and all the wellbore components are deemed as thick-walled cylinders and completely bonded. However, some of these assumptions and simplifications may lead to unrealistic results. For instance, failure modes in all directions would not be captured in two-dimensional models (plane strain), and the axisymmetric geometry and assumed isotropic in-situ stresses do not correctly reflect the real conditions.

Numerical modelling can be very advantageous regarding its ability to incorporate material non-linearity, different types of geometry and boundary conditions, and in-situ stress conditions [47]. The accuracy of these numerical models is reliant on the validation and verification of experimental data.

Nabipour, Joodi and Sarmadivaleh [28] simulated downhole stresses using FEM along with sensitivity analysis on casing internal pressure, anisotropic horizontal in-situ stresses, and casing eccentricity. They have used a plane strain model with thermo-elastic material properties, and the interfaces are assumed to be fully bonded. Wang and Taleghani [37] performed three-dimensional (3-D) poroelastic simulations to assess the integrity of the cement sheath around wellbores. The interfaces have been modelled using porous cohesive elements. The cohesive parameters were

determined by running inverse analyses on the bonding studies carried out by Evans and Carter [86]. Despite, the massive progress regarding interface modelling, the use of elastic behaviour for cement sheath is an over-simplification that can affect the accuracy and reliability of the results.

Fleckenstein, Eustes and Miller [51] employing von-Mises criteria, they demonstrated that the magnitude of tangential stresses would be greatly decreased if the cement sheath acts as a ductile material with lower Young's modulus and higher Poisson's ratio which is in agreement with Goodwin and Crook [32]. The lack of pressure dependency of the von Mises criteria is however problematic in modelling cementitious materials. To overcome this shortcoming, a number of researchers have adopted the Mohr-Coulomb criteria in their work.

Bosma, Ravi, van Driel and Schreppers [44] used a two-dimensional model considering symmetry geometry for the wellbore. Mohr-Coulomb plasticity combined with smeared cracking description was used to model the cement sheath under compression / shear and tension. The cement sheath interfaces were modelled using interface elements applying a coulomb friction criterion. Nygaard, Salehi, Weideman and Lavoie [74] performed an experimental-numerical study using Mohr-Coulomb plasticity model for the cement and formation to investigate the effect of dynamic loading on wellbore leakage. Their parametric study showed that cement with higher Young's modulus and Poisson's ratio are detrimental factors causing radial fractures, tensile failure and debonding. However, utilising cement with low strength mechanical properties increases the risk of shear failure within the cement sheath.

The Mohr-Coulomb model assumes a linear relationship between $\sqrt{J_2}$ and $I_1$ in the meridian plane, while this relationship has been experimentally shown to be non-linear [76, 77], for cementitious materials, particularly at low confinement. The major principal stress $\sigma_1$ and intermediate principal stress $\sigma_2$ are defined independently in Mohr-Coulomb model which results in underestimation of the yield strength of the material and, it is not in a good agreement with experiments in which the effect of $\sigma_2$ is being considered. The shape of yield surface in the deviatoric plane is an asymmetrical hexagon, whereby the sharp corners can hinder convergence in numerical simulations [70, 78]. Moreover, quasi-brittle materials experience a huge volume change due to a large amount of inelastic strains (dilatancy) which has been overlooked so far by using associated flow rules in the modelling of the cement. The associative plastic flow rules tend to lead to poor results in dilatancy evolution [55].

The use of the modified Cam-Clay model has been suggested as a method to incorporate cement micro cracking mechanisms by Bois, Garnier, Rodot, Sain-Marc and Aimard [36] owing to the nonlinearity of stress-strain curve achieved from the isotropic drained compression tests [72] and

heterogeneous nature of cement at the microscale. Although important aspects of materials behaviour (material strength, compression or dilatancy, and critical state of elements under high distortion) are considered in this model, the tensile post-peak material is not incorporated into this framework.

Numerical modelling has been significantly improved regarding complexity and ability to model wellbore integrity assessment with a high degree of accuracy. The incorporation of appropriate material constitutive law, particularly with regards to cracking behaviour, and consequently the evolution of corresponding constitutive parameters still requires attention. Bosma, Ravi, van Driel and Schreppers [44] advocated the used of smeared cracking models in combination with plasticity and Salehi [114] have employed a discrete crack methodology via the use of nonlinear fracture mechanics for cohesive cracks. Therefore, in this study, the concrete damage plasticity (CDP) model [54, 115] was used to investigate cement mechanical failure. This model incorporates a non-associative flow rule and damage under both tensile and compressive stress states, which is more appropriate for the characterisation of cementitious materials.

This paper is organised as follows; Section 5.2 describes cement constitutive modelling including the experimental procedures to achieve mechanical properties, the concrete damage plasticity model as the appropriate constitutive model to be utilised, and the calibration of the model parameters according to the performed experiments. Surface-based cohesive behaviour is introduced for interface modelling and followed by determination of cohesive model parameters in section 5.3. Section 5.4 describes finite element modelling including model components, material properties, geometry and discretisation, initial and boundary conditions. Section 5.5 describes the results of cement sheath and the interfaces integrity investigations for the different initial state of in-situ stresses followed by conclusion in section 5.6.

## 5.2. Cement Constitutive Modelling

Portland Class G (API rating) well cement is predominantly utilised as the basis of well cement blends [34], additives are incorporated to obtain certain properties such as enhanced strength or reduced weight [34]. In general, the permeability of cement used in oil and gas industry (cement class G) is very low usually less than 0.1 mDarcy [11]. Therefore, hydraulic isolation will be achieved, and any probable leakage pathways can be created only through flaws resulting from issues in cement placement procedures or mechanical failure due to the variation of pressure during wellbore operations.

### 5.2.1. **Experimental Procedures**

The concrete damage plasticity model (CDP) has been calibrated and verified according to the experiments have been performed by Arjomand, Bennett and Nguyen [116]. The specimens were made of cement class G cured at $30^0$C for 28 days in a pre-heated water tank with a manageable thermostat. The slurry density was 1.9 g/cc corresponding to water to cement mass ratio of 0.44. Prior to testing, the surfaces of samples were ground to obtain smooth ends, so the ends were perfectly orthogonal to the longitudinal cylinder axis [77].

In this study, relatively slender cylindrical specimens were employed to avoid problems with platen restraint that are encountered using squat cube specimens [35]. The uniaxial strength measured using sufficiently slender specimens is usually around 70%-90% of the cube strength [106]. The uniaxial compressive strength was determined using 42 mm diameter, 100 mm long cylindrical specimens which deliver aspect ratio of 2.4. It also helps to minimise the effect of specimen shape on the determination of the modulus of elasticity [117].

To investigate the effect of displacement rate on the cement uniaxial compressive behaviour three displacement rates of 0.2 mm/min, 0.1 mm/min and 0.04 mm/min were investigated. The samples showed highly brittle behaviour at displacement rates of 0.2 mm/min and 0.1 mm/min. To capture post-peak behaviour, the displacement rate was reduced to 0.04 mm/min at which the specimen displayed less brittle behaviour.

Figure 5.1 demonstrates the uniaxial compressive behaviour of the specimens were subjected to a constant displacement rate of 0.04 mm/min. The axial displacement of the loading platen was measured by two external 25 mm span linear variables differential transformers (LVDT) were installed at the bottom platen on the sides of the specimen. The obtained results are in a good agreement a subset of the data detailed in Teodoriu, Asamba and Ichim [118], Teodoriu, Amani, Yuan, Schubert and Kosinowski [119]'s for compressive strength of class G without additives at the age of 28 days.

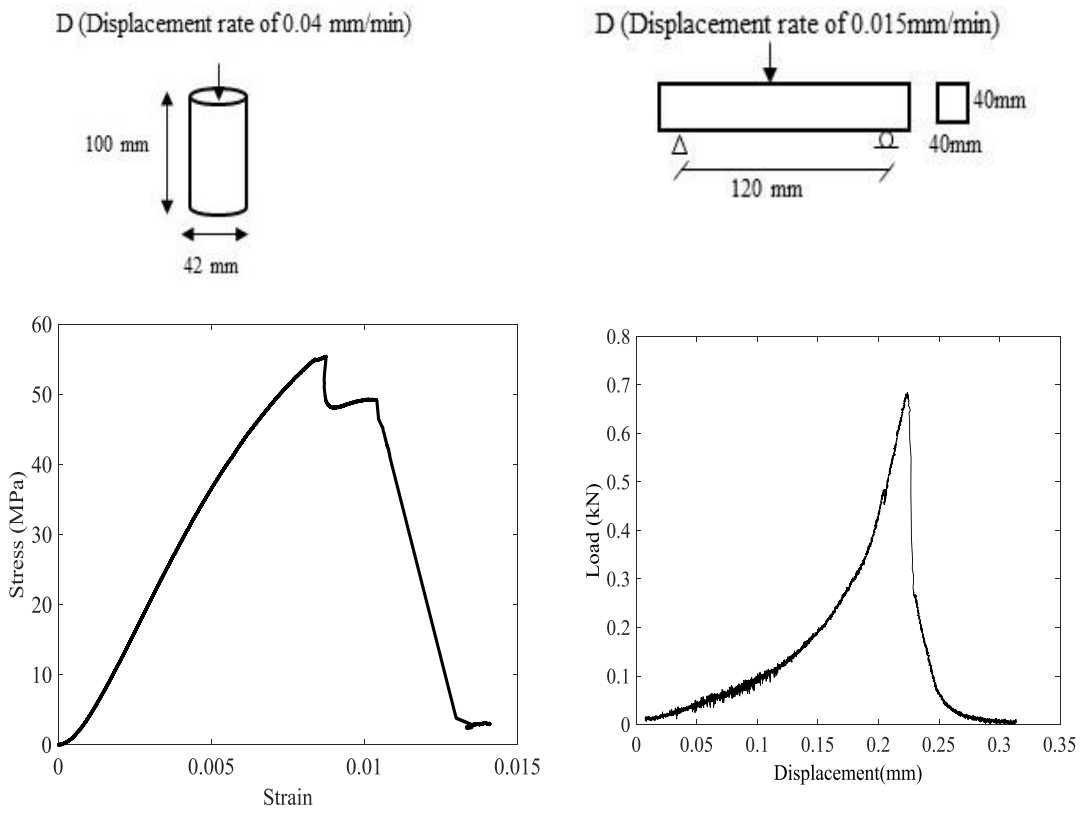


Figure 5.1: Cement Class G Compressive and Tensile Response Respectively

To determine the tensile stress of the cement according to ASTM standard C348-02 "Standard Test Method for Flexural Strength of Hydraulic-Cement Mortars" [120] three-point bending tests were run on beams with dimensions of 160×40×40 mm. The suggested loading rate by the standard was 2640±110 N (600±25 lbf/min) was very fast. Therefore, the tests were performed by applying displacement rate of 0.015mm/min. The axial displacement of the loading platen was measured via using of two LVDTs installed on both sides of the beam specimens. The corresponding load-displacement is shown in Figure 5.1. The tensile strength $\sigma_t$ for prisms was calculated, from the bending tests as:

$$\sigma_t = \frac{3Fs}{2bd^2} \tag{5.1}$$

where F is the applied load, s in the span of the beam, b and d are width and depth of the specimen respectively.

### 5.2.2. **Concrete Damage Plasticity Model Description**

A continuum model based on damage mechanics and plasticity theory can be used to better describe the behaviour of class G cement, from initial yield to failure. In this study, we employ

the concrete damage plasticity (CDP) model initially developed by Lubliner et al. (1989) and expanded by Lee and Fenves (1998). This model includes two damage variables for tensile and compressive failure, taking into account unilateral effects. The elastoplastic behaviour is decoupled from degradation damage response which leads to easier implementation [54, 55, 115, 121].

The uniaxial tension response is characterised by a linear elastic relationship until reaching the failure stress ($\sigma_t$) which corresponds to the beginning of micro-cracking in the material as calculated based on equation 5.1 and 5.2. Beyond the failure stress, the effects of micro-cracking is taken into account in the model using a softening stress-strain response. The uniaxial compression response is also characterised by a linear elastic relationship until reaching the initial compressive strength ($\sigma_c$) followed by stress hardening in the plastic region up to the ultimate stress ($\sigma_{cu}$). Strain softening occurs subsequent to reaching the ultimate stress.

The stress-strain relations under uniaxial tension and compression are defined as follows respectively.

$$\sigma_t = (1 - d_t)E_0\left(\varepsilon_t - \tilde{\varepsilon}_{pl}^t\right) \tag{5.2}$$

$$\sigma_c = (1 - d_c)E_0\left(\varepsilon_c - \tilde{\varepsilon}_{pl}^c\right) \tag{5.3}$$

where $d_t$ and $d_c$ are tensile and compression damage variables; $E_0$ is initial undamaged stiffness; $\tilde{\varepsilon}_{pl}^t$ , $\tilde{\varepsilon}_{pl}^c$ are tensile and compressive equivalent plastic strains respectively.

The shape of yield surface in the deviatoric plane changes according to the ratio of the second stress invariant on the tensile meridian to the compressive meridian which allows better capture of material behaviour. This yield function was defined by Lubliner, Oliver, Oller and Onate [54] with some modifications made by Lee and Fenves [115] afterwards to interpret the evolution of strength under tension and compression. It is defined as follows.

$$F = \frac{1}{1-\alpha}\left(\bar{q} - 3.\alpha.\bar{p} + \beta\left(\tilde{\varepsilon}_{pl}\right)\langle\bar{\sigma}_{max}\rangle - \gamma\langle-\bar{\sigma}_{max}\rangle\right) - \bar{\sigma}_c\left(\tilde{\varepsilon}_{pl}^c\right) = 0 \tag{5.4}$$

where $\langle \quad \rangle$ is the Macaulay bracket, $\bar{\sigma}_{max}$ is the maximum principle effective stress, $\bar{p} = -\frac{1}{3}\bar{\sigma}\,.I$ is the effective hydrostatic stress and $\bar{q} = \sqrt{\frac{3}{2}\bar{S}.\bar{S}}$ is the Mises equivalent effective stress with $\bar{S} = \bar{p}I + \bar{\sigma}$ being the deviatoric part of the effective stress tensor. The function $\beta\left(\tilde{\varepsilon}_{pl}\right)$ in (5.4) is defined as follows.

$$\beta\left(\tilde{\varepsilon}_{pl}\right) = \frac{\bar{\sigma}_c\left(\tilde{\varepsilon}_{pl}^c\right)}{\bar{\sigma}_t\left(\tilde{\varepsilon}_{pl}^t\right)}(1-\alpha) - (1+\alpha) \tag{5.5}$$

in which two cohesion stresses are employed for the modelling of cyclic behaviour.

$$\alpha = \frac{\left(\frac{\sigma_{bo}}{\sigma_c}\right) - 1}{2\left(\frac{\sigma_{bo}}{\sigma_c}\right) - 1} \tag{5.6}$$

where $\frac{\sigma_{bo}}{\sigma_c}$ is the ratio of biaxial compressive yield stress to uniaxial compressive yield stress. Experimental values used for concretes for $\frac{\sigma_{bo}}{\sigma_c}$ vary between 1.10 and 1.16 which result in parameter $\alpha$ in the range of $0.08 \leq \alpha \leq 0.1212$ [54, 122].

The shape of loading surface in the deviatoric plane is controlled by parameter $\gamma$ in Equation (5.4) [123] and define as

$$\gamma = \frac{3(1 - K_c)}{2K_c + 3} \tag{5.7}$$

where $K_c = \frac{(\sqrt{J_2})_{TM}}{(\sqrt{J_2})_{CM}}$ is a coefficient determined at a given state $\bar{p}$ , $J_2$ is the second invariant of stress with the subscripts TM and CM employed for the tensile and compressive meridians respectively and must satisfy the condition $0.5 \leq K_c \leq 1$ . Typical values of $K_c$ for concrete have been suggested from 0.64 by Schickert and Winkler [124] and 0.66 by Richart, Brandtzaeg and Brown [125] to 0.8 by Mills and Zimmerman [126]. Lubliner, Oliver, Oller and Onate [54] used $K_c = 2/3$ for plain concrete which results in γ=3.

For the non-associated flow rule, the plastic potential $G$ in the form of the Drucker-Prager hyperbolic function is used.

$$G = \sqrt{(\epsilon\sigma_{to} \tan\psi)^2 + \bar{q}^2} - \bar{p}.\tan\psi \tag{5.8}$$

In which $\sigma_{to}$ is the uniaxial tensile stress at failure, the dilation angle $\psi$ is measured in a p-q plane at high confining pressure, and $\epsilon$ is an indicator for the eccentricity of the plastic potential surface.

### 5.2.3. **Calibration of Concrete Damage Plasticity Parameters for Cement Class G**

Determination of constitutive parameters is significantly important in FE analysis to minimise the error of the models in the analyses [127]. The constitutive parameters have to be calibrated in a way to have a good connection with experimental data [128]. To calibrate the corresponding parameters in the concrete damage plasticity model for cement class G, the values for cement Young's modulus $E_0$, cement initial compressive stress $\sigma_c$, ultimate compressive stress $\sigma_{cu}$, and tensile strength $\sigma_{to}$ were extracted from the uniaxial compression tests and three-point bending tests respectively detailed in section 5.2.1.

Some data pertaining to the confinement dependent strength of well cements is available in the open literature, for example [129, 130]. However, the biaxial to uniaxial strength ratio required for the characterisation Lubliner, Oliver, Oller and Onate [54] plasticity model is difficult to extract from triaxial data. In addition, the post-peak material behaviour is less well reported, even for simple stress states. Therefore, the ${}^{\sigma_{bo}}/_{\sigma_c}$ , $\gamma$ , $\psi$, and $\epsilon$ parameters are calibrated for cement class G in this section.

A three-dimensional uniaxial compressive test was simulated in ABAQUS/standard to find the best match between the performed uniaxial compression experiment test in the laboratory and numerical one. The geometry and the boundary conditions are depicted in Figure 5.2. A finite element mesh was considered for the simulation purposes consisting of 42456 8-noded hexahedral elements. The simulations were performed using a reasonable range for each parameter to obtain the best fit to experimental data. The trial range of dilation angle $\psi$ was between $25^0$ to $45^0$, the eccentricity $\epsilon$ was examined between a range of 0.01 to 0.1, the ratio of biaxial compressive yield stress to uniaxial compressive yield stress was tried between 1.1 to 1.17, and the $K_c$ which is the ratio of $\sqrt{J_2}$ in tensile meridian to compressive meridian were tried from 0.5 to 1.

The closest match to the experimental results found by using dilation angle $\psi$=$42^0$, eccentricity $\epsilon$=0.1, $\frac{\sigma_{bo}}{\sigma_c}$ =1.16, and $K_c$=0.8. The results and corresponding failure patterns in the laboratory and ABAQUS are shown in Figures 5.2 and 5.3. It can be seen that the simulation results can match the experimental counterparts in terms of both macro responses and failure pattern, indicating that the calibrated set of parameters are appropriate for the modelling of this class G cement.

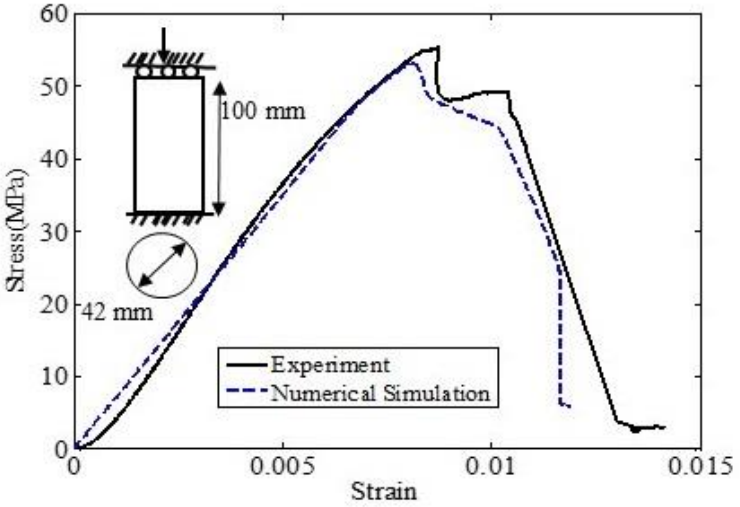


Figure 5.2: Concrete Damage Plasticity Calibration

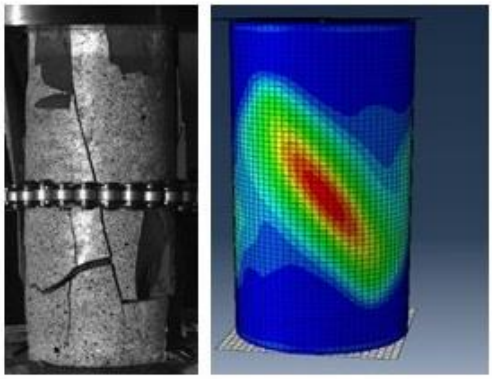

Figure 5.3: Failure Patterns in Uniaxial Compression Test

The compression damage $d_c$ was computed using Equation (5.9) [4] as shown in Figure 5.4.

$$d_c = 1 - \frac{\sigma_c'}{\sigma_{cu}} \tag{5.9}$$

where $\sigma_c'$ is the axial stress of the cement on the descending branch, and $\sigma_{cu}$ is the peak point of stress-strain curve in Figure 5.1.

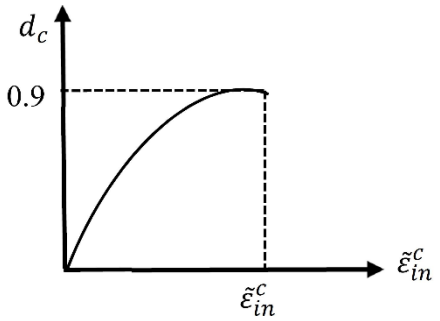


Figure 5.4: Compression Damage vs. Inelastic Strain

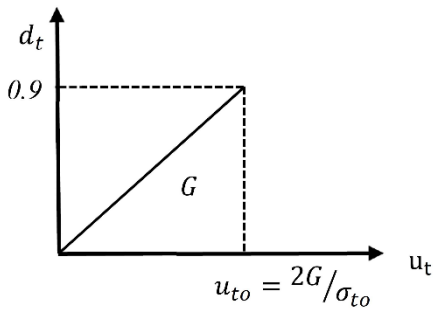


Figure 5.5: Tensile Damage vs. Cracking Displacement

Tensile damage $d_t$ were defined using a linear relationship [131] between cement tensile strength and cracking displacement via assuming cement fracture energy of 55 N/mm (Figure 5.5). Table 5.1 summarised all the cement class G mechanical properties utilised in the integrity simulations in this paper.

*Table 5.1: Cement Class G Mechanical Properties Obtained from the Experiments and Calibration Process*

| ***Young's modulus*** $E_0$ ***(GPa)*** | ***Dilation angle*** $\psi$ ***(degrees)*** | ***Fracture energy*** $G_f$ ***(N/mm)*** | |
|---|---|---|---|
| *6.8* | *42* | *35* | |
| ***Eccentricity*** $\varepsilon$ | $K_c$ | ***Initial compressive stress*** $\sigma_c$ ***(MPa)*** | ***Inelastic strain*** $\widetilde{\varepsilon_{in}^{c}}$ |
| *0.1* | *0.8* | *50* | *0.007353* |
| ***Ultimate compressive stress*** $\sigma_{cu}$ ***(MPa)*** | ***Tensile stress*** $\sigma_t$ ***(MPa)*** | ***Cracking Strain*** $\widetilde{\varepsilon_{ck}^{t}}$ | |
| *55* | *1.92* | *0.0000485* | |

This calibration procedure has enabled us to identify the remaining model parameters required, however there remain large uncertainties in applying these parameters to real world scenarios. The cement curing (duration, temperature, pressure), the cement mix design, operating temperature and stress history that a wellbore has experienced will all effect the state of the material.

## 5.3. Interface Modelling

The interfaces of the cement with the casing and the formation are recognised as the weakest link in providing an effective barrier to leakage [37, 81]. Its behaviour and failure can be described by a cohesive model for interfaces between two different materials [81]. In this study, the cement sheath interfaces are represented by surface-based cohesive behaviour defined as surface interaction property with traction transferring capacity. The relationship between tractions $t$ and separation $\delta$ can be described using a traction – separation law (Equation 5.10).

$$\{t\} = \begin{Bmatrix} t_n \\ t_s \\ t_t \end{Bmatrix} = \begin{bmatrix} K_{nn} & K_{ns} & K_{nt} \\ K_{sn} & K_{ss} & K_{st} \\ K_{tn} & K_{ts} & K_{tt} \end{bmatrix} \begin{Bmatrix} \delta_n \\ \delta_s \\ \delta_t \end{Bmatrix} = K\{\delta\} \tag{5.10}$$

where the subscripts n, s, t refer to the normal and shear directions along the interface. K are stiffness components, which are coupled in all directions.

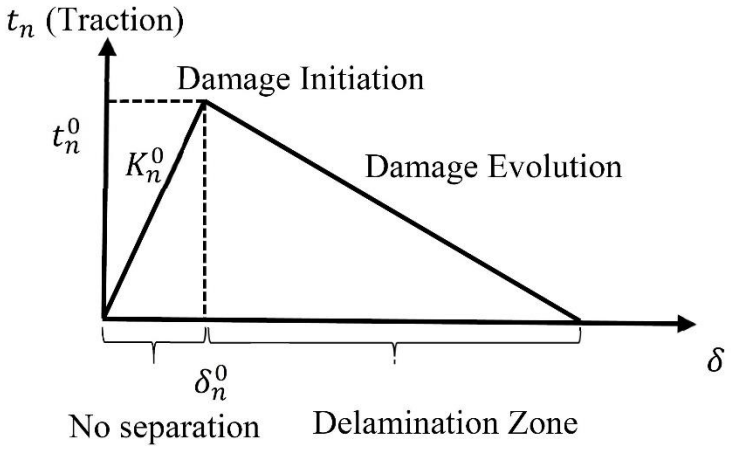


Figure 5.6: Linear Softening Traction-Separation Law

The cohesive constraint is enforced at each slave node for cohesive surfaces. Contact separation is expressed as the relative displacements between the slave surface nodes and their matching opposite nodes on the master surfaces along the contact normal and shear directions. Stresses are defined for the surface-based cohesive surfaces as the cohesive forces acting along the contact normal and shear directions divided by the contact area at each contact point.

The degradation and eventual failure of the bond between two cohesive surfaces are described by a damage law. The damage mechanism is defined based on damage initiation criterion and damage evolution law as shown in Figure 5.6 for the normal direction. In this study, a quadratic nominal stress criterion was used to incorporate mixed mode conditions; this criterion is shown to be successful in regards to prediction of delamination [132]. The criterion is defined as

$$\left\{\frac{\langle t_n \rangle}{t_n^0}\right\}^2 + \left\{\frac{t_s}{t_s^0}\right\}^2 + \left\{\frac{t_t}{t_t^0}\right\}^2 = 1 \tag{5.11}$$

where the superscript 0 denotes the maximum traction or initiation traction value.

The Benzeggagh-Kenane (BK) [133] fracture energy criterion is used here with the assumption that the critical fracture energy during separation along the first and the second shear direction are the same i.e. $G_s^C = G_t^C$.

$$G_n^C + (G_s^C - G_n^C)\left\{\frac{G_S}{G_T}\right\}^\eta = G^C \tag{5.12}$$

where $G_S$=$G_s + G_t$ and $G_n^C$ is the fracture energy in normal direction, $G_s^C$ is the fracture energy purely in the first shear direction ($G_s^C$ and $G_t^C$ are assumed to be equal). The total fracture energy in the mixed mode condition defines as $G_T = G_n + G_S$ and $\eta$ is a cohesive property parameter [82, 87, 134].

### 5.3.1. **Determination of Cohesive Model Parameters**

Carter and Evans [84] designed experimental setups to measure cement shear bond and the hydraulic bond between casing and cement and demonstrated that the bond properties were both pressure and temperature dependent. Shear bond is essential to support the pipe mechanically, whereas the hydraulic bond prevents the formation of micro-annuli. Hydraulic bond failure may happen due to casing expansion and contraction of a wellbore because of different wellbore operations. They also designed another setup to measure the bonding properties between cement and rock formation [82]. Evans and Carter [86] presented the push-out test which repeated by Ladva, Craster, Jones, Goldsmith and Scott [85] using cement class G to measure the shear bonding between cement and formation.

In the analyses performed in this contribution, we have adopted the cohesive parameters determined by Wang and Taleghani [37]. They performed an inverse analysis on the experimental results of [84-86] which are summarised in Table 5.2.

*Table 5.2: Cohesive properties of cement / casing and cement/rock [37]*

| **Cohesive Properties Interfaces** | **Shear Strength (kPa)** | **Normal Strength (kPa)** | **Cohesive Stiffness (kPa)** | **Critical energy $(J/m^2)$** |
|---|---|---|---|---|
| Casing/Cement Interface | 2000 | 500 | $30E^6$ | 100 |
| Cement/Formation Interface | 420 | 420 | $30E^6$ | 100 |

Whilst the parameters adopted have been determined from a number of experimental studies, there remains great uncertainty regarding these parameters. Carter and Evans [84], Evans and Carter [86] demonstrate that the cement shear bond to the casing is dependent on the curing temperature, the pipe condition, and variations of different cement formulations. The adherence degree of well cement to rock is highly variable and site dependent. The cement hydraulic bond to the casing and formation is dependent on type of the formation, surface finish of the pipe, type of mud layer, and degree of mud removal [85, 135].

## 5.4. Finite Element Modelling

A three-dimensional finite element framework is utilised to investigate the effect of pressure increasing events such as pressure integrity testing on the cement sheath integrity using ABAQUS

/ Standard software package [57]. Pressure tests are performed after the casing cementation, such as casing integrity tests or formation integrity tests (leak-off test) by applying pressure upon recently set cement [26]. In order to have more realistic simulations, stress-related factors which induce wellbore failure in the fields especially during drilling operations were incorporated within the framework including eccentricity and applying anisotropic in-situ stresses.

### 5.4.1. **Material Properties**

The cement sheath was modelled by using CDP model and calibrated according to experiments performed on cement class G, as addressed in section 5.2.1. The interfaces of cement sheath with casing and rock formation were modelled using surface-based cohesive behaviour feature using cohesive parameters mentioned in Table 5.2. Elastic mechanical properties of the steel casing and four different rock formations are defined as shown in Table 5.3. For ease of comparisons the rocks' stiffness were normalised with respect to the cement's stiffness detailed in Table 5.3.

*Table 5.3: Mechanical Properties of Casing and Rock Formation*

| **Casing Properties** | **Young's Modulus E (GPa)** | **Poisson's ratio $\nu$** | **Casing Grade** | **Reference** |
|---|---|---|---|---|
| Steel Casing | 210 | 0.3 | C-75 | [37] |
| **Formation Properties** | **Young's Modulus E (GPa)** | **Poisson's ratio $\nu$** | **$E_N$ (Normalised)** | **Reference** |
| Soft Rock | 0.807 | 0.4 | 0.12 | [136] |
| Shale | 3.25 | 0.26 | 0.47 | [37] |
| Hard Rock-1 | 17.2 | 0.2 | 2.51 | [47] |
| Hard Rock-2 | 27.2 | 0.2 | 3.96 | [47] |

### 5.4.2. **Geometry and Discretisation**

The model consists of a casing, cement sheath with eccentricity, formation rock and the interfaces of cement sheath with casing and formation shown in Figure 5.7. To reduce the computational cost of the model, half symmetry has been exploited and a 5 in. horizontal slice considered. The casing outside and inside diameter is chosen according to Schlumberger's i-Handbook [137] 7.625 in. and 6.625 in. respectively [47]. The borehole size is 8.5 in. The total extent of the modelling of the surrounding formation is important to avoid any artificial effects in the stress distributions and to assure that far-field stresses are applied from a reasonable distance from the wellbore. According to Salehi [114], the model size should be at least four times bigger

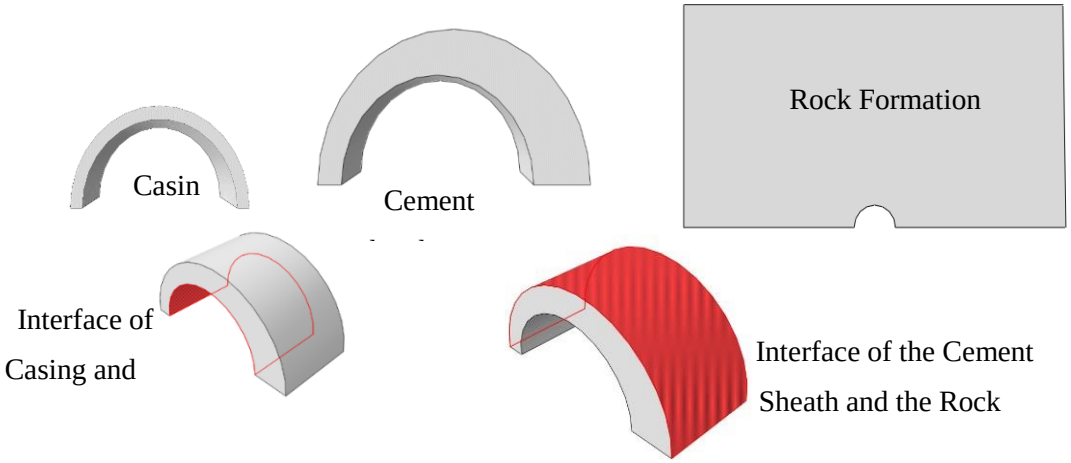


Figure 5.7: Casing, Cement Sheath With 70% Eccentricity, Formation Rock and the Cement Interfaces with The Casing and Rock Formation

than the borehole size. Furthermore, the section near the wellbore has to mesh finer than the rest of the formation. This finer section should be at least 2-3 times bigger than the borehole size to improve accuracy [114]. Therefore, the formation rock was partitioned into two sections and meshed with finer mesh near the wellbore area and coarser mesh in the far field area.

A mesh sensitivity analysis was performed to obtain a pragmatic element size in terms of accuracy and computation time. The damage formulation in ABAQUS [57] alleviates the well-known mesh dependency problem associated with local damage models by incorporating the concept of characteristic length [56] into the formulation.

### 5.4.3. **Initial State of Stress and Boundary Conditions**

Initial geo-stress components were defined as $\sigma_H$ and, $\sigma_h$ in the initial step of the analyses. Maximum and minimum horizontal stresses were applied parallel to X-axis and Y-axis in an exchangeable way. The anisotropy of geo-stresses would cause shear stresses to the wellbore [82] and is required to be considered in cement integrity modelling. The formation density and drilling fluid density is assumed as 2000 kg/m$^3$ and 1557.74 kg/m$^3$ respectively [47]. The model thickness (height of the model) in comparatively small to the width of the model, hence, the variation of overburden (vertical) initial stress in depth is negligible and not considered in the model. The corresponding overburden effective stress at the surface casing shoe with the vertical depth of 560 m was computed as $\sigma_v$=20 MPa, and all shear components are zero as shown in Figure 5.8. Displacement constrains were applied to the normal direction of bottom surface, outer surface of formation, and symmetric surfaces.

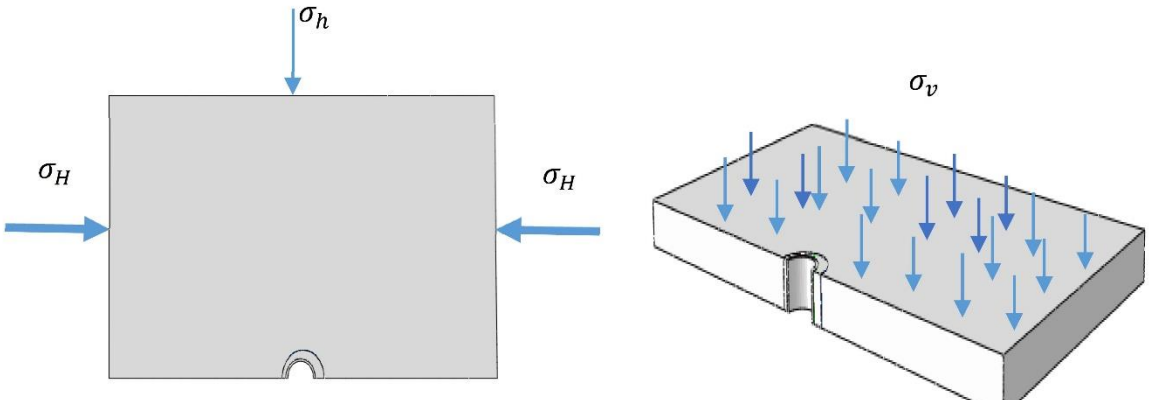


Figure 5.8: Applying Anisotropic In-situ Stresses

## 5.5. Results and Discussions

A pressurized eccentric wellbore is subjected to isotropic and anisotropic in-situ stresses. Table 5.4 describes the three arrangements of applied in-situ stresses. The isotropic in-situ stresses were applied as $\sigma_H = \sigma_h$ to have a basis results for comparison purposes and the anisotropic in-situ stresses applied in Case-1 and Case-2.

The stress state, plastic deformations, and debonding within the cement sheath corresponding to the different scenarios were analysed. The cement mechanical properties (given in Table 5.1), the degree of eccentricity and the overburden pressure of 20 MPa are maintained constant for all the scenarios. The contribution of surrounding rock formations' properties along with in-situ stress

confinement effects on cement mechanical failure was analysed by varying four different rock formations' stiffness given in Table 5.3 (sections 5.5.1 and 5.5.2).

*Table 5.4: In-situ Stress Arrangements*

| **In-situ stress arrangements** | $\boldsymbol{\sigma_{XX}}$ | $\boldsymbol{\sigma_{YY}}$ | $\boldsymbol{\sigma_{XX} = \sigma_H}$ **(MPa)** | $\boldsymbol{\sigma_{YY} = \sigma_h}$ **(MPa)** |
|---|---|---|---|---|
| Basis Case (Isotropic) | $\sigma_H$ | $\sigma_H$ | 12.6 | 12.6 |
| Case-1 (Anisotropic) | $\sigma_H$ | $\sigma_h$ | 12.6 | 8.82 |
| Case-2 (Anisotropic) | $\sigma_h$ | $\sigma_H$ | 8.82 | 12.6 |

The effect of applied pressure along with different cases of in-situ stresses confinement and different rock properties were analysed through interpretation of compression damage (crushing index) and tensile damage (cracking index). The potential debonding occurrences were investigated by using surface-based cohesive behaviour interaction property at the interfaces without any pre-assumption of the crack initialisation or localisation propensity.

### 5.5.1. **Compression Damage**

The potential crushing caused by pressuring the wellbore along with in-situ stress within the cement sheath is examined through the compression damage contours, local compression damage paths and a global compression damage indicator in the following sections. Figure 5.9 illustrates the compression damage contours within the cement sheath. The compression damage contour within the cement sheath applying isotropic in-situ stresses (Basis-Case) for all the scenarios. with different rocks' properties shows the dominant effect of eccentricity on the stress distribution within the cement sheath regardless of in-situ stress arrangements.

The effect of in-situ stress anisotropy is examined in Case-1 and Case-2 along with different rock's properties. As can be seen in Figure 5.9, the compression damage is mainly distributed at the narrower side of the cement sheath. Due to different arrangements of in-situ stresses the compression damage magnitude and the localisation of cracks bands changes for each case. This effect is better visualised for scenarios case. This effect is better visualised for scenarios with softer rocks $E_N<1$) in Case-1 and Case-2. As shown in the contour plots the magnitude and propagation of compression damage for stiffer rocks ($E_N>1$) are similar for anisotropic cases.

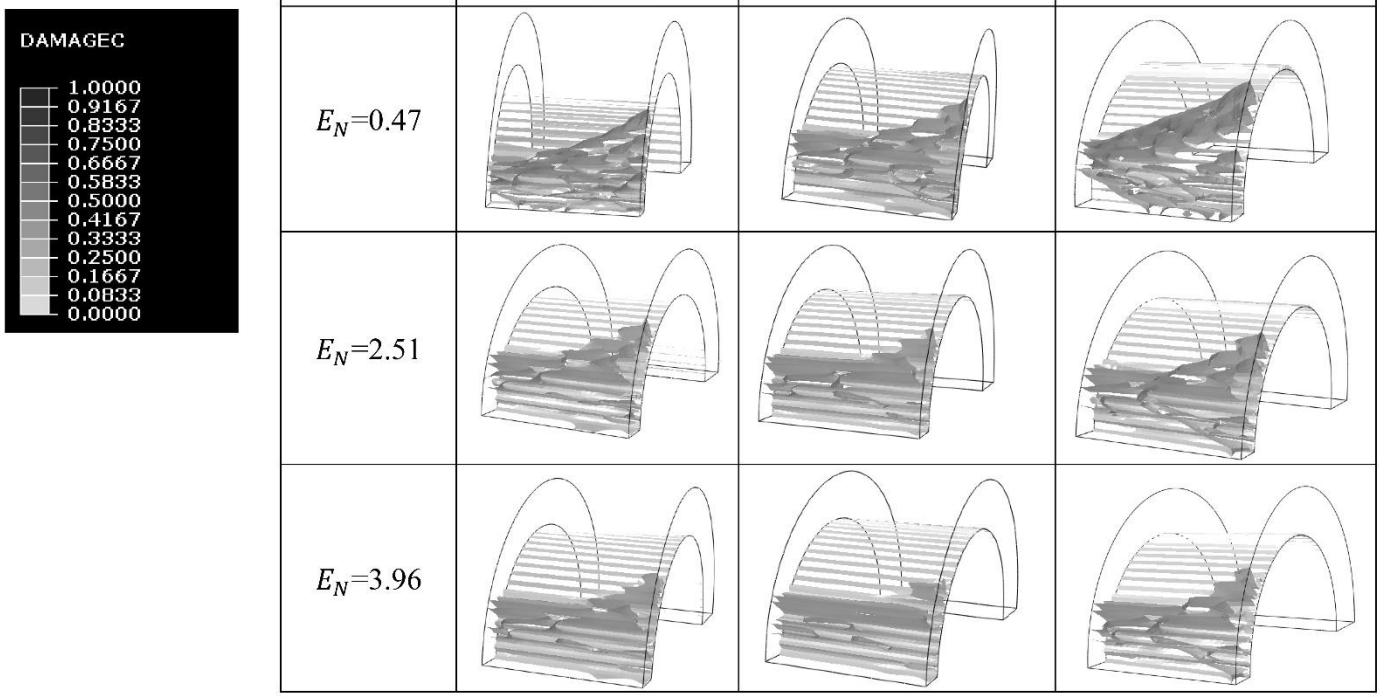


Figure 5.9: Compression Damage Contours within the Cement Sheath

To perform a more precise comparison of the local compression damage magnitude and its localisation, three cross-sectional paths as shown in Figure 5.10 were selected. The cross-sectional paths start at the inner wall of the cement sheath (cement sheath interface with the casing) and go around the thickness and come back to the starting points. Three cross-sectional paths were selected at three different locations to cover the narrower side, the middle side, and the widest side of the cement sheath.

Figure 5.11 shows compression damage along the cross-sectional paths for rocks' stiffness simulations at which $E_N$<1 (Soft rock $E_N$=0.12, Shale $E_N$=0.47) considering three cases of applying in-situ stresses. As can be seen in all the scenarios considering two different rocks' mechanical properties, the highest level of damage occurred within the path-1 (a) and path-1 (d) located at the narrowest side of the cement sheath. The localisation and distribution of local compression damage within the cement sheath for anisotropic cases surrounded by soft rock

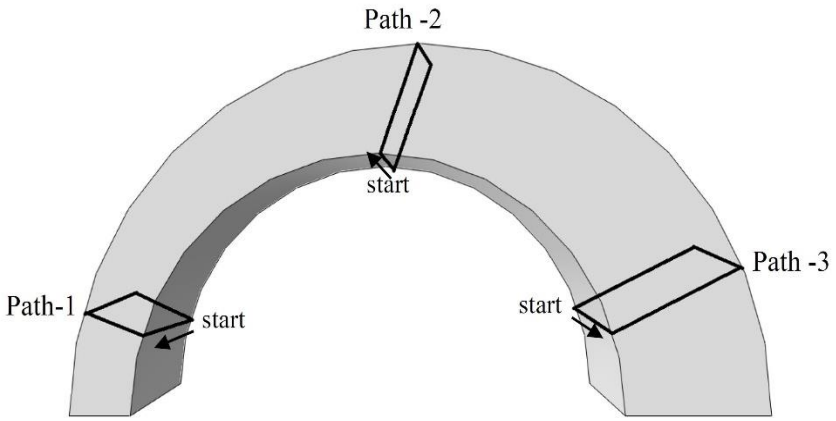


Figure 5.10: Three Different Cross-Sectional Paths within the Cement Sheath

($E_N$=0.12) and the shale formation ($E_N$=0.47) are similar. However, the magnitude of maximum compression damage is relatively higher for the softest rock and the local maximum compression damage occurred within the first segment of the path-1 (a) which is the inner wall of the cement sheath at one isolated node. Crushing failure potential in such a case ($E_N$=0.12) can be considered higher than the case of shale formation ($E_N$=0.47). The shale formation is stiffer than the soft rock, the resistance of the system becomes higher against pressure, therefore, the crushing damage index is lower.

The magnitude of damage decreases as the path goes on towards the outer wall of the cement sheath along the paths. Comparing graphs in Figure 5.11 shows the descending trend of the local compression damage from the narrow side (path-1) towards the widest side (path-3).

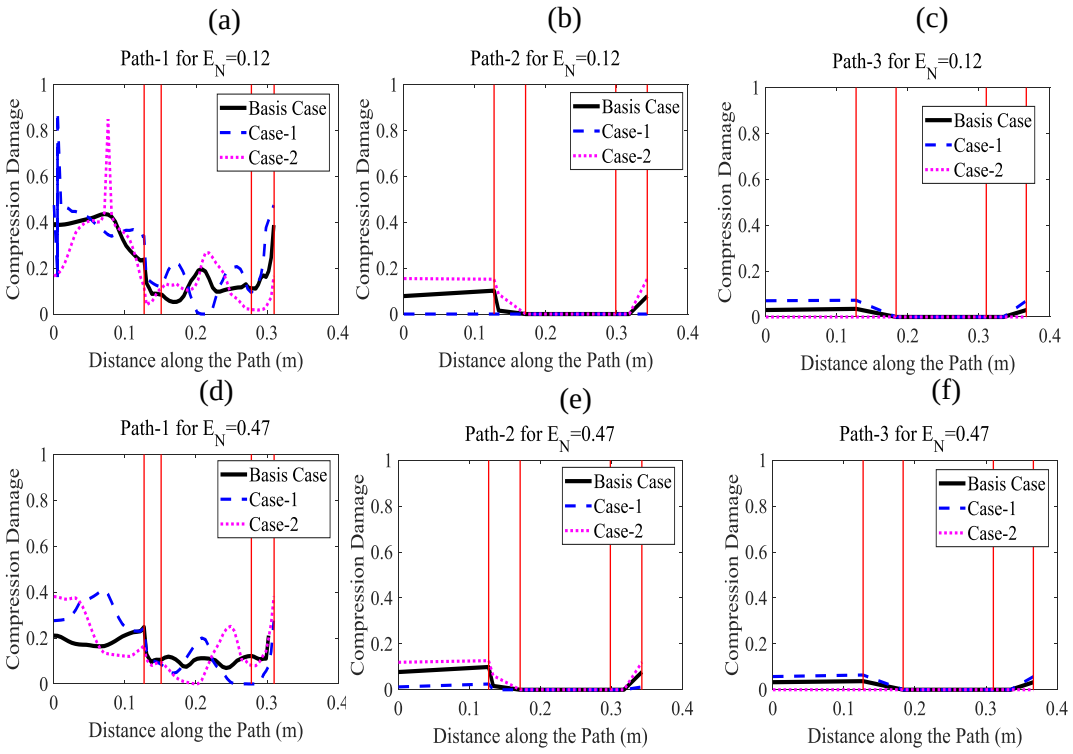


Figure 5.11: Compression Damage along the Three Paths for
Simulations with $E_N$ <1 (vertical red lines indicate the corners)

Figure 5.12 shows compression damage along the cross-sectional paths for rock's stiffness simulations at which $E_N$>1 (Hard Rock-1($E_N$=2.51), Hard Rock-2 ($E_N$=3.96) considering three cases of applying in-situ stresses.

Figures 5.12(a) and 5.12(d) demonstrate that the magnitude of maximum compression damage is considerably lower for the Basis-Case (isotropic cases) in comparison with Case-1 and Case-2 (anisotropic cases). The considerable difference in maximum compression damage magnitude is indicative of the destructive role of in-situ stress anisotropy on causing crushing damage within the cement sheath.

The response of the cement sheath with stiffer rock and anisotropic in-situ stresses to the elevated bore pressure for both rocks $E_N$=2.51 and $E_N$=3.96 was similar regarding local compression damage magnitude and localisation. The magnitude of maximum compression damage in situations in which rock is stiffer than cement ($E_N > 1$) in some nodes is quite considerable (≈0.6) as it can be seen in Figure 5.12 (a) and (d). The local maximum compression damage magnitude is still located within the narrower side but more distributed than the softer

rock in Figure 5.11. It is however difficult to make a strong conclusion on the severity of damage in these cases (of Figures 5.11 and 5.12), and other forms of damage indicators are hence needed.

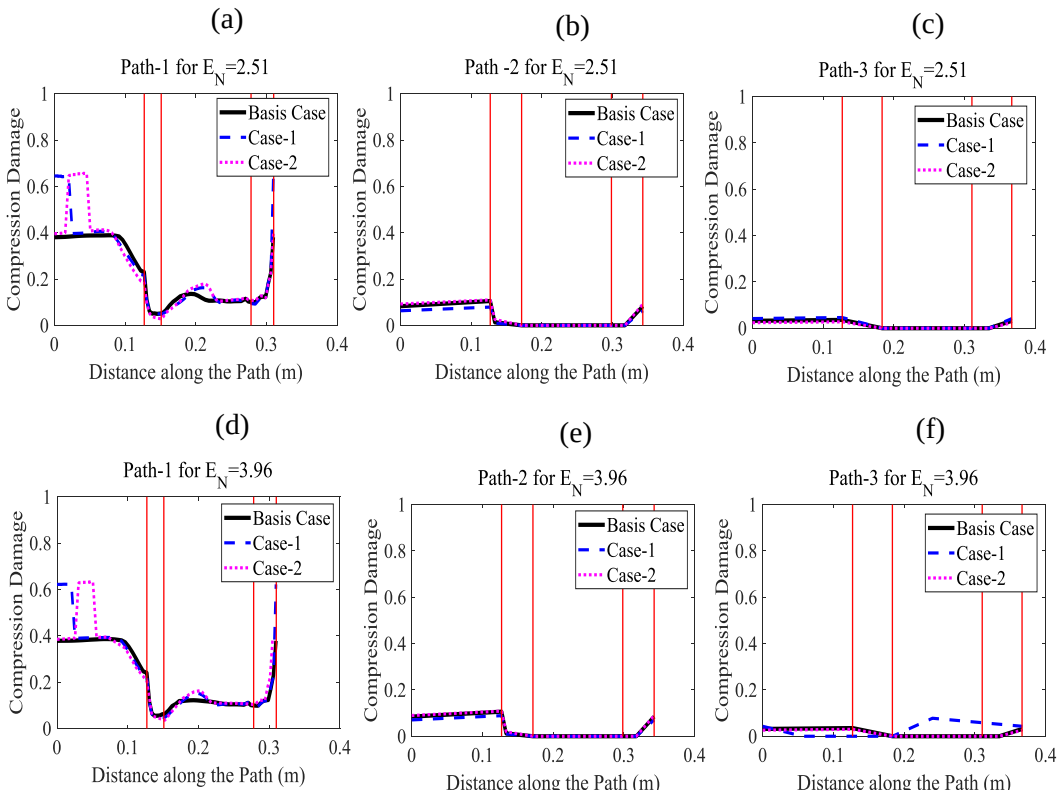


Figure 5.12: Compression Damage along the Three Paths for Simulations with $E_N$ >1(vertical red lines indicate the corners)

In order to have a more general indicator to compare all the different scenarios, we define a global compression damage indicator ($D_c$) as follows.

$$D_c = \sum_0^N \left(\frac{d_c}{N}\right) \tag{5.13}$$

where $d_c$ is the local compression damage magnitudes for all the nodes within the cement sheath, and N is the number of nodes with associated compression damage, i.e. excluding nodes where the damage is zero. Figure 5.13 shows the indicator values versus the normalised stiffness ($E_N$) for each case

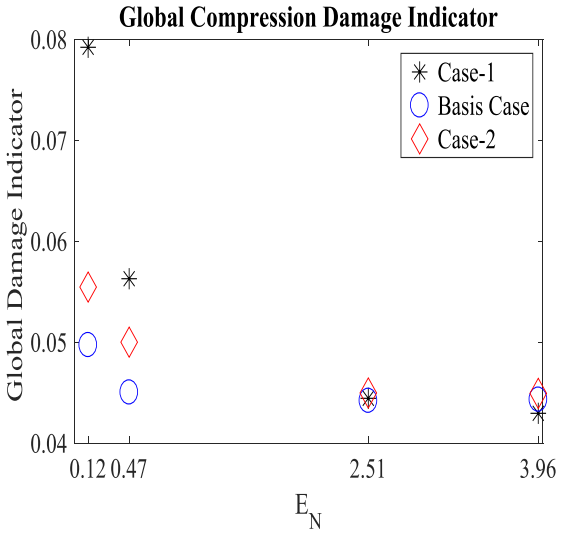


Figure 5.13: Global Compression Damage Indicator vs. $E_N$

Considering the contour plots, and the global compression damage indicator in Figure 5.13 confirms that compression damage was more distributed within the cement sheath in Case-1 and Case-2 in comparison with the Basis-Case for scenarios involving the softer rocks ($E_N$<1). While the global compression damage indicator for scenarios with stiffer rocks ($E_N$>1) was similar in all the cases regardless of in-situ stress arrangements. The different response of the systems with stiffer rocks ($E_N$>1) towards in-situ stress arrangements indicate that although the anisotropy of in-situ stresses in Case-1 and Case-2 imposes the additional shear stress to the system, the stiffer rocks possess higher resistance against the shear stress and don't transfer these stresses to the cement sheath.

### 5.5.2. **Tensile Damage**

The tensile cracking susceptibility is examined through the tensile damage contours and a global tensile damage indicator. The state of local tensile damage (cracking) contours within the cement sheath after applying isotropic and anisotropic in-situ stresses is shown in Figure 5.14. As can be seen, the tensile damage is more localised in comparison with compression damage shown in Figure 5.9. Considering the tensile damage contours of the Basis-Case demonstrates the important role of eccentricity in the distribution of tensile stress within the cement sheath again.

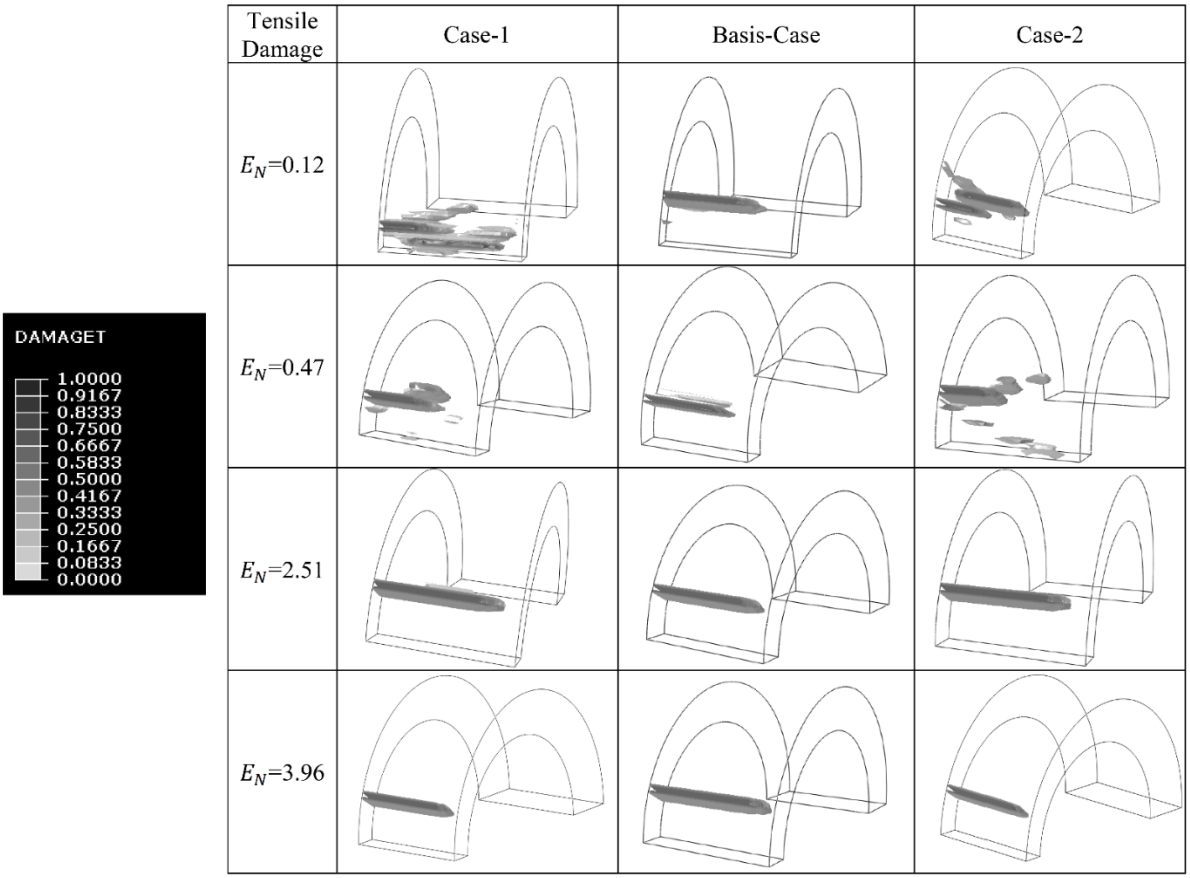


Figure 5.14: Tensile Damage Contours within the Cement Sheath

The maximum tensile damage for the Basis-Case reached 0.48 for the softest rock ($E_N$ =0.12). In contrast, the maximum tensile damage magnitude reached 0.67 and 0.58 for the softest rock in Case-1 and Case-2 respectively and covered a relatively large zone on the narrowest side. The high difference of tensile damage magnitude shows the critical effect of in-situ stresses anisotropy particularly in scenarios with softer rocks ($E_N$ <1). Tensile damage contours in Figure 5.14 show for stiffer rocks scenarios ($E_N$ >1), the tensile damage magnitude and its localisation are similar for all the scenarios.

The surface-based cohesive behaviour defined by means of the contact interaction property enables the interface of cement sheath to transmit normal and shear forces across the interface as described in Equation 10. The tangential slips of the interface are assumed elastic, and it is resisted by the cohesive strength of the bond while the cohesive stiffness is undamaged which leads to the creation of shear forces. The degradation of cohesive stiffness and evolution of damage in shear directions defined in Equations 5.11 and 5.12 as well. The simulations show high contact shear stresses at the interface of the cement and the rock formation is the driving force for initialisation

and propagation of tensile cracks through the whole thickness of the narrow side of the cement sheath.

To compare all the zones within the cement sheath experiencing tensile cracking, a global tensile damage indicator ($D_t$) was computed as follows.

$$D_t = \sum_0^N \left(\frac{d_t}{N}\right) \tag{5.14}$$

where $d_t$ is the local tensile damage magnitude for all the nodes within the cement sheath, and N is the number of nodes with associated tensile damage.

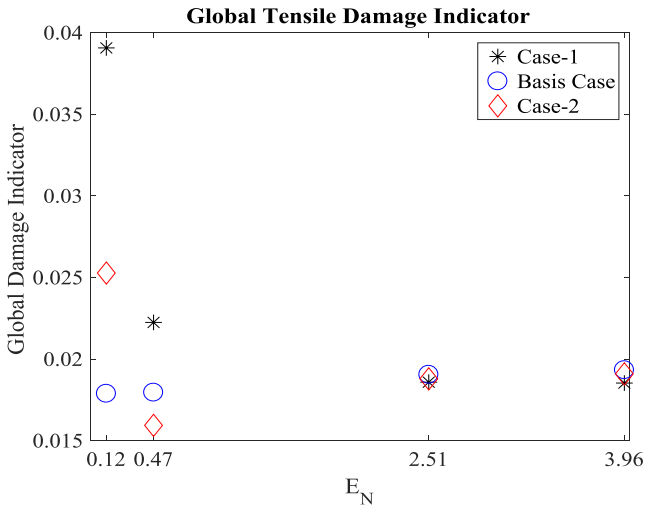


Figure 5.15: Global Tensile Damage Indicator vs. $E_N$

Figure 5.15 shows that the cement sheath surrounded by the softest rock ($E_N$ =0.12) experiences the highest level of tensile damage the in anisotropic cases (Case-1 and Case-2). The low stiffness of the rock makes the cement sheath more vulnerable to the additional shear stresses caused by anisotropic in-situ stresses and results in the formation of microcracking. While in situations with stiffer rocks ($E_N$ >1), the lower level of microcracking is seen in Figure 5.15 due to the high resistance of stiffer rocks against the shear stresses.

The simulations confirm the significance of tensile cracks and tensile properties to be incorporated into the constitutive modelling. In situations in which $E_N$ <1(softer rocks) as shown in Figure 5.14, the relatively high magnitude of tensile damage (above 0.5) means almost above 50% of tensile strength was degraded and significant tensile cracks initiated and propagated through the whole thickness of the cement sheath.

### 5.5.3. **Propensity of Forming Micro Annuli**

The soundness of the cement sheath bonds with the casing and the rock formation is examined through a contact stiffness degradation index. Figure 5.16 demonstrates the starting location of the selected paths along the cement sheath interfaces with the casing and rock formations.

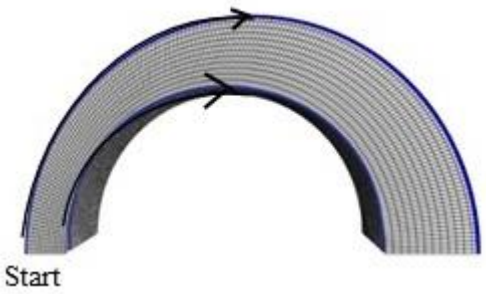


Figure 5.16: Cement Sheath Interfaces with the Casing and Rock Formation

The contact stiffness of the cement sheath with the casing is fully degraded for all the combinations of rock properties shown in Figure 5.17 regardless of in-situ stress arrangements. In contrast, the degradation of cement sheath bond with the rock formation is dependent contrast, the degradation of cement sheath bond with the rock formation is dependent on the rock‘s stiffness shown in Figure 5.18.

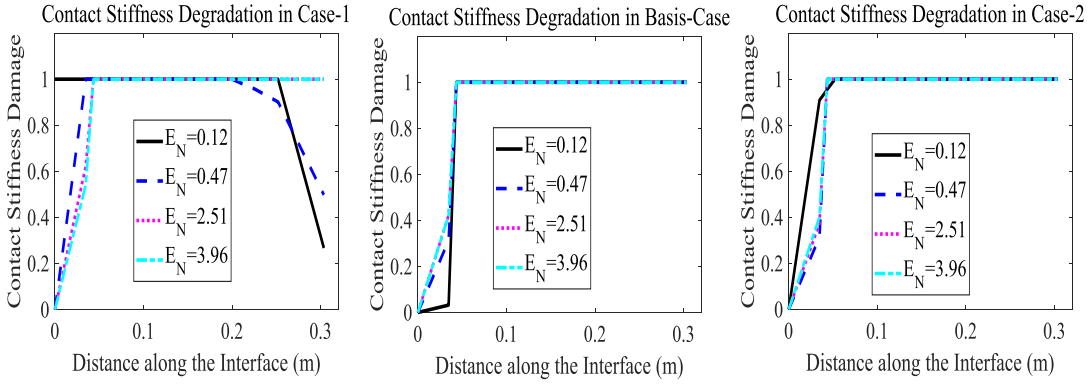


Figure 5.17: Contact Stiffness Degradation at Cement Sheath Interface with the Casing

The response of the cement sheath interface with rock formation for the softest rock ($E_N$=0.12) is different than the rest of the scenarios (Figure 5.18). In Case-1 the due to high confinement of in-situ stresses the narrower part show more resistance to sliding as can be seen at the beginning of the interface length while in Case-2 the effect of high confinement can be seen in the middle length of the interface. In the Basis-Case (Figure 5.18(b)) the contact stiffness is undamaged for some sections at the widest section of the cement sheath.

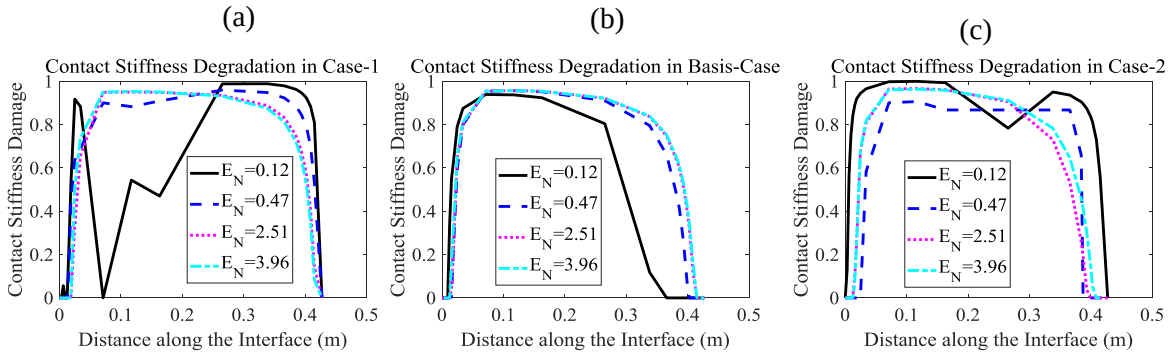


Figure 5.18: Contact Stiffness Degradation at Cement Sheath Interface with the Rock Formation

The interfaces are the most vulnerable part of a wellbore due to the high difference in the stiffness of surrounding materials, and high contact shear stresses in tangential and normal directions of the interface length in wellbore operations. The contact stiffness degradation, reaching near to one in all the simulations, indicates the high potential to debond. Cement sheath centralisation, remedial cementing and using expandable liners (at the interfaces of cement and casing) may mitigate these effects.

## 5.6. Conclusion

A systematic approach was taken to assess the integrity of cement sheath after being pressurised in relation to the creation of cracks within the cement sheath and microannulus made of class G well cement. The key point of the approach is the employment of a constitutive model taking into account the difference in tensile and compressive responses and the pressure-dependent of the behaviour under shearing at different levels of confinement. To obtain the corresponding model parameters, laboratory experiments, including uniaxial compression tests and three-point bending tests, were performed on specimens manufactured from class G well cement.

A three-dimensional finite element model including a casing, cement sheath with eccentricity, and rock formation was built to investigate the effect of enhancing pressure in a wellbore. The interfaces of cement sheath with the casing and the rock formation were modelled using surface-based cohesive behaviour to examine debonding. The integrity of the cement sheath and the interfaces were investigated through different scenarios of changing in-situ stress orientations and different rocks' stiffness.

The results show the dominant effect of eccentricity on the distribution of stress within the cement sheath which emphasises the importance of casing centralisation. Comparing the damaged area and geometry of cracks in anisotropic in-situ stresses scenarios with isotropic scenarios suggests that wellbore operations require more attention within the heterogenic geological fields.

The global damage indicator in crushing and cracking states shows a higher risk while operating in anisotropic in-situ stress fields with soft rocks. The high magnitude of cracking index (tensile damage) confirms the importance of incorporating tensile failure mechanisms into the constitutive modelling. The creation of micro-cracks can lead to increasing the permeability of the cement sheath. The simulations also demonstrate that the material interfaces are potential weak points.

The data required to populate complex constitutive models (for both materials and the interfaces between them) coupled with the variability of wellbore architectures, cement mix designs, cement curing regimes, and operating conditions suggests that the assessment of wellbore integrity remains a challenge.

**Acknowledgements**

The authors wish to express their appreciation to the laboratory technicians at the University of Adelaide for their assistance with the experimental study and to Adelaide Brighton Ltd for kindly supplying materials.

# 6. Effect of Curing Conditions on the Mechanical Properties of Cement Class G with the Application to Wellbore Integrity (PAPER-2)

E. Arjomand, T. Bennett, Effect of curing conditions on the mechanical properties of cement class G with the application to wellbore integrity, Australian Journal of Civil Engineering, (2018) 1-15.

# Statement of Authorship

| | |
|---|---|
| Title of Paper | Effect of curing conditions on the mechanical properties of cement class G with the application to wellbore integrity |
| Publication Status | ☑ Published ☐ Accepted for Publication<br>☐ Submitted for Publication ☐ Unpublished and Unsubmitted work written in manuscript style |
| Publication Details | Arjomand, E., & Bennett, T. (2018). Effect of curing conditions on the mechanical properties of cement class G with the application to wellbore integrity. *Australian Journal of Civil Engineering*, 1-15. |

## Principal Author

| | | | |
|---|---|---|---|
| Name of Principal Author (Candidate) | Elaheh Arjomand | | |
| Contribution to the Paper | Performing the experiments, results interpretation, and manuscript preparation. | | |
| Overall percentage (%) | 85% | | |
| Certification: | This paper reports on original research I conducted during the period of my Higher Degree by Research candidature and is not subject to any obligations or contractual agreements with a third party that would constrain its inclusion in this thesis. I am the primary author of this paper. | | |
| Signature | | Date | 3-12-2018 |

## Co-Author Contributions

By signing the Statement of Authorship, each author certifies that:

i. the candidate's stated contribution to the publication is accurate (as detailed above);

ii. permission is granted for the candidate in include the publication in the thesis; and

iii. the sum of all co-author contributions is equal to 100% less the candidate's stated contribution.

| | | | |
|---|---|---|---|
| Name of Co-Author | Terry Bennett | | |
| Contribution to the Paper | Conception, analysis and input into the manuscript. | | |
| Signature | | Date | 6/12/2018 |

| | | | |
|---|---|---|---|
| Name of Co-Author | | | |
| Contribution to the Paper | | | |
| Signature | | Date | |

Please cut and paste additional co-author panels here as required.

# Effect of Curing Conditions on the Mechanical Properties of Cement Class G with the Application to Wellbore Integrity


## ABSTRACT

Wellbore integrity is highly dependent on the cement sheath integrity. Cement sheaths play an essential role in preventing any communication between the formation fluids and the surrounding environment. Mechanical failure of the cement sheath within a wellbore is influenced and governed by many factors including cement mechanical properties. However, the paucity of cement class G mechanical parameters including lack of experimental data under different confining pressure, tensile properties, and the effect of curing temperatures on the long-term cement mechanical properties are impediments to the numerical simulations in wellbore integrity assessments. Therefore, this study aims to expand the cement class G mechanical properties inventory. This paper investigates the mechanical behaviour of cement class G at two different curing temperatures ($30^{o}$C and $70^{o}$C) at the age of 28 days. The effect of both the curing regime and confining pressures (15 MPa and 30 MPa) on the strength and post-peak response of the cement under compression are examined. The measurement of tensile capacity and fracture energy performing indirect three-point bending tests along with the challenges involved with measuring fracture energy and modifications incorporated to the three-point bending test set-up, to measure fracture energy properly, are explored. The results were validated by Digital Image Correlation (DIC) technique measurements. The obtained experimental were interpreted and subsequently utilised as input data for a constitutive model specifically formulated for modelling the geo-materials such as cementitious materials and validated by numerical analysis.


## 6.1. Introduction

Wellbores provide access to natural resources such as oil and gas and are encased in concentric layers of steel casing and cement sheaths. After drilling the borehole, steel casing is inserted and is held in place and protected by a sheath of cement which is pumped into the annular gaps. Although wellbores are sealed and block any interaction which may occur between formation fluid and geologic strata, the integrity of wellbores might still be compromised [9, 18]. At this stage, wellbores may turn into the high-permeability conduits for the formation fluids [19] which could pose a potential risk to the environment by contaminating groundwater and/or the atmosphere. The cement sheath is responsible for providing zonal isolation and preventing the leakage of formation fluids during the lifetime of a wellbore [31] and therefore the cement sheath should be

designed and placed so that it withstands the external conditions imposed upon it, including, in-situ stresses, high internal pressures and high temperature.

Portland Cement Class G is mostly utilised as the base of oil wells in the oil and gas industry. Additives may also be incorporated to achieve certain properties [34]. The general components of cement class G are general grinding Portland cement clinker, Dicalcium Silicate ($Ca_2SiO_4$) and water. During the manufacture of cement class G, only Calcium Sulfate ($CaSO_4$) and water can be added to the cement clinker [42]. The mechanical properties of the cement are highly dependent on the curing conditions, which vary along the wellbore depth and corresponding to the exposure to the formation fluids with different conditions [20, 88, 89]. It is worth noting that the cement used in the oil and gas industry has very low permeability, usually less than a 0.2 mD [38]. Therefore, hydraulic isolation is attained straightforwardly, and any probable leakage can only happen through mechanical failures of the cement sheath [11].

The behaviour of the cement sheath under different conditions should be properly simulated using an appropriate constitutive model to predict the mechanical damage of the cement sheath. The effect of pressure and temperature changes, which may result in shear/compression (crushing), and tensile (cracking) damage should be incorporated into the constitutive model. One of the most challenging parts of constitutive modelling is to determine the model parameters through performing experiments and interpretation of the experimental outcomes. Many laboratory tests have been carried out on well cement, simulating the wellbore condition, to determine the key parameters for modelling purposes.

Thiercelin, Dargaud, Baret and Rodriguez [108] performed a study on cement class G, with varieties of additives, to determine the material's flexural, compression strength, and Young's modulus in flexural and compression. The tensile properties were obtained using three-point bending tests on 30×30×120 mm prisms, with a loading rate of 0.01 cm/min. The compressive properties were measured via uniaxial compression tests on 50.8×50.8×50.8 mm (2×2×2 in) cubes. The volume of additives, curing conditions, and slurry density were different for each test. Therefore, it is hard to associate any change in mechanical properties with one specific factor.

Roy-Delage, Baumgarte, Thiercelin and Vidick [91] designed a slurry formulation with cement class G to achieve highly durable cement. They cured the samples at $77^{o}C$ and $114^{o}C$ with a pressure of 20.7 MPa (3000 psi) for three days or upon reaching a constant compressive strength. Three-point bending tests and crushing tests were performed on beams with the size of 30×30×120 mm and cubes with the size of 50.8× 50.8× 50.8 mm (2× 2× 2 in) respectively. They investigated

the interaction between flexible cement and expanding agents and concluded that the cement with both flexible and expanding additives shows more durability in long-term periods.

Cyclic pressure tests were run on hollow cylinders (50×100 mm) of cement class G by Yuan, Teodoriu and Schubert [103]. The samples were cured under three different conditions for 14 days: room conditions; atmospheric pressure 0.1 MPa (14.7 psi) at the temperature of $75^{o}$C in an oven; and under 18 MPa (2610 psi) at $100^{o}$C in an autoclave. They demonstrated the cement can endure more cycles as confining pressure increases. Additionally, the cement with a higher Poisson's ratio and lower Young's modulus is stronger encountering low cycle fatigue.

Nasvi, Ranjith and Sanjayan [92] used cylindrical samples of 50 ×100 mm to measure the uniaxial compression strength of cement class G. The samples were oven cured at different temperatures between $30^{0}$C to $80^{0}$C for 24 hours excluding the samples required to be cured at room temperature. Subsequently, all of the samples were kept at ambient temperature for another 48 hours. Their results demonstrated that samples that cured at $60^{0}$ C had the maximum uniaxial compressive strength of 53 MPa, but that samples cured above this temperature yielded a lower uniaxial compressive strength. The Young's modulus of cement class G is higher at lower curing temperatures and reaches its maximum value at the curing temperature of $40^{0}$ C.

Guner and Ozturk [94] measured both uniaxial compressive strength and Young's modulus at different cement curing periods of 2, 7, and 14 days. They concluded increasing the curing time increases the mechanical properties of cement by 2-3 times.

Teodoriu and Asamba [95] investigated the effect of salt concentration on cement class G properties by performing uniaxial compression tests on cubic samples with the size of 50.8× 50.8× 50.8 mm (2× 2× 2 in). They cured samples in water in atmospheric condition for 24hrs and then the samples were placed in an autoclave for curing period of one to seven days under two different conditions ($30^{o}$C and 10 MPa / $150^{o}$C and 20 MPa). They also measured the compressive strength of samples cured at the atmospheric condition at the age of 21 days. Their results of the batch without salt with respect to the first curing condition were summarised in Table 1 for comparison purposes. They showed the samples with 5% ± 2.5% salt concentration curing at ambient to moderate temperature, yield the maximum compressive strength among all the other samples with different salt concentration curing at different conditions.

Romanowski, Ichim and Teodoriu [96] compared two methods for measuring the cement compressive strength (ultrasonic pulse velocity versus mechanical method). The tests were performed at different curing times on cement class G, cement class G with bentonite, and cement class G with other additives. They demonstrated that the outcomes of ultrasonic methods should

be calibrated using the mechanical (destructive) measuring methods. The importance of achieving an extensive database on wellbore cement was emphasised in this study as well.

Table 6.1 summarises all of the results available in the literature including the aforementioned studies and studies by Morris, Criado, Robles and Bianchi [102], Labibzadeh, Zahabizadeh and Khajehdezfuly [104], from unconfined compression test studies on the cement class G to the best of our knowledge.

*Table 6.1: Compressive Measurements Retrieved from the Available Literature*

| Reference | Compressive Strength (MPa) | Curing Temperature ($^0$C) | Curing Pressure (MPa) | Curing Time (days) | Sample shape and size (mm) |
|---|---|---|---|---|---|
| Roy-Delage, Baumgarte, Thiercelin and Vidick [91] | 37 | 77 | 27 | 3 | Cube 50.8×50.8×50.8 mm |
| Roy-Delage, Baumgarte, Thiercelin and Vidick [91] | 39.2 | 114 | 20.7 | 3 | Cube 50.8×50.8×50.8 mm |
| Morris, Criado, Robles and Bianchi [102] | 36.9 | 84 | 27 | 2 | Cube 50.8×50.8×50.8 mm |
| Guner and Ozturk [94] | 49 | ambient | ambient | 3 | Cylinder 50 mm×100 mm |
| Nasvi, Ranjith and Sanjayan [92] | 53 | 60 | − | 3 | Cylinder 50 mm×100 mm |
| Nasvi, Ranjith and Sanjayan [92] | 27 | ambient | ambient | 3 | Cylinder 50 mm×100 mm |
| Teodoriu, Amani, Yuan, Schubert and Kosinowski [119] | 36 | 65 | − | 1 | Cube 50.8×50.8×50.8 mm |
| Teodoriu, Amani, Yuan, Schubert and Kosinowski [119] | 48 | ambient | ambient | 3 | Cube 50.8×50.8×50.8 mm |
| Teodoriu, Amani, Yuan, Schubert and Kosinowski [119] | 64 | 65 | − | 14 | Cube 50.8×50.8×50.8 mm |

| | | | | | |
|---|---|---|---|---|---|
| Teodoriu, Amani, Yuan, Schubert and Kosinowski [119] | 47 | 100 | 18 | 14 | Cube 50.8×50.8×50.8 mm |
| Yuan, Teodoriu and Schubert [103] | 55.7 | ambient | ambient | 14 | Hollow cylinder 110 mm×160 mm ($r_i = 40mm$) |
| Yuan, Teodoriu and Schubert [103] | 60.8 | 75 | ambient | 14 | Hollow cylinder 110 mm×160 mm ($r_i = 40mm$) |
| Yuan, Teodoriu and Schubert [103] | 56.7 | 100 | 18 | 14 | Hollow cylinder 110 mm×160 mm ($r_i = 40mm$) |
| Labibzadeh, Zahabizadeh and Khajehdezfuly [104] | 10.95 | ambient | ambient | 1 | Cube 50.8×50.8×50.8 mm |
| Labibzadeh, Zahabizadeh and Khajehdezfuly [104] | 16.55 | ambient | ambient | 2 | Cube 50.8×50.8×50.8 mm |
| Labibzadeh, Zahabizadeh and Khajehdezfuly [104] | 14.24 | 38 | 2.8 | 2 | Cube 50.8×50.8×50.8 mm |
| Labibzadeh, Zahabizadeh and Khajehdezfuly [104] | 12.72 | 68 | 17.2 | 2 | Cube 50.8×50.8×50.8 mm |

| | | | | | |
|---|---|---|---|---|---|
| Labibzadeh, Zahabizadeh and Khajehdezfuly [104] | 16.4 | 121 | 51.7 | 2 | Cube 50.8×50.8×50.8 mm |
| Labibzadeh, Zahabizadeh and Khajehdezfuly [98] | 4.59 | 149 | 51.7 | 2 | Cube 50.8×50.8×50.8 mm |
| Labibzadeh, Zahabizadeh and Khajehdezfuly [104] | 18.82 | 82 | 41.4 | 2 | Cube 50.8×50.8×50.8 mm |
| Teodoriu and Asamba [95] | 2 | 30 | 10 | 1 | Cube 50.8×50.8×50.8 mm |
| Teodoriu and Asamba [95] | 18 | 30 | 10 | 3 | Cube 50.8×50.8×50.8 mm |
| Teodoriu and Asamba [95] | 28 | 30 | 10 | 7 | Cube 50.8×50.8×50.8 mm |
| Teodoriu and Asamba [95] | 42 | ambient | ambient | 21 | Cube 50.8×50.8×50.8 mm |

Recent studies in oil and gas cementing technology indicate that cement sheath mechanical failure happens not only because of induced compressive stresses but also because of tensile stresses [97].

Heinold, Dillenbeck and Rogers [97] cured samples made of cement class G with additives in a standard high-pressure high-temperature (HPHT) curing chamber, under a pressure of 20.7 MPa at two different temperatures of 37.8°C and 93.3°C for 72 hours. They performed uniaxial compression tests, flexural strength tests, and tensile strength tests on cubes with the size of 50.8×50.8×50.8 mm (2×2×2 in), prismatic specimens with the size of 40.6×40.6×160.02 mm (1.6×1.6×6.3 in), and dog bone specimens, respectively. They showed that the correlation between unconfined compression strength and tensile strength (empirical relations) does not always apply. According to their results, samples cured at the higher temperature (93.3°C) demonstrated lower flexural strength and higher tensile strength. Heinold, Dillenbeck, Bray and

Rogers [99] continued their study by curing samples at two different temperatures of $54.4^0$C or $82.2^0$C for 48 hours in an atmospheric water bath. The authors compared the results of splitting tensile strength (STS) tests with direct tensile tests on the dog-bone sample. The splitting tensile strength test results overestimated the tensile properties of cement class G by order of 1.5 to 2.5. However, direct tensile test measurements can also be impacted by stress concentrations on the samples at or near grip points (point loading), which can lead to immature breakable of the samples.

Dillenbeck, Boncan, Clemente and Rogers [98] performed uniaxial tensile tests on dog-bone samples made of cement class H and additives to measure the cement uniaxial tensile strength. They developed a new testing machine to simulate downhole conditions in a wellbore for curing purposes and performed tensile tests on dog-bone samples. The results showed that the uniaxial tensile strength of the cement samples was highly dependent on the stress loading rate. Therefore, the authors addressed the necessity of developing a standard loading rate at which to perform cement tensile tests.

Quercia, Chan and Luke [100] characterised the tensile strength of cement class G using the Weibull method by performing direct tensile tests on dog-bone samples, and Brazilian tests on cylindrical samples. Weibull statistics is a characterization tool which describes the strengths spread along with strength variations due to sample size and provides more assurance and reliability in risk analysis [100]. The samples were made of cement class G and micro-fibres. The samples were initially cured in a pressurised chamber for 24 hours at $25^0$C and 10.34 MPa (1500 psi) and then demolded and cured underwater for six days. The authors also used modified dog-bone molds, which act as holders to avoid grip concentration points. Table 6.2 summarises the results of tensile test studies that are available in the literature to the best of our knowledge.

*Table 6.2: Tensile Measurements Retrieved from the Available Literature*

| Reference | Flexural Tensile strength (MPa) | Tensile strength (MPa) | Splitting Tensile (MPa) | Curing Temperature ($^0C$) | Curing Pressure (MPa) | Curing Time (days) | Sample shape and size (mm) | Additives |
|---|---|---|---|---|---|---|---|---|
| (Thiercelin et al. 1997) | 7.24 | – | – | 134.4 | 20.68 | 3 | Prisms 30×30×120 | Latex (2 gps) |
| (Roy-Delage et al. 2000) | 8.46 | – | – | 77 | 20.68 | 3 | Prisms 30×30×120 | – |
| (Heinold, Dillenbeck & Rogers 2002) | 3.43 | 1.83 | – | 37.8 | 20.68 | 3 | Prisms 40.64×40.6 ×160.02 | – |
| (Heinold, Dillenbeck & Rogers 2002) | 1.4 | 2.31 | – | 93.33 | 20.68 | 3 | Prisms 40.64×40.6 ×160.02 | – |
| (Heinold et al. 2003) | 7.48 | 2.75 | 4.68 | 54.4 | Atmospheric Pressure | 2 | Prisms 40.64×40.6 ×160.02 | Defoamer 0.02 gal/sk |
| | | | | | | | Cylinders 50.8 (D) ×50.8 (H) | |
| Heinold et al. (2003) | 7.52 | 2.58 | 5.75 | 82.2 | Atmospheric Pressure | 2 | Prisms 40.64×40.6 ×160.02 | Defoamer 0.02 gal/sk |
| | | | | | | | Cylinders 50.8 (D) ×50.8 (H) | |
| Quercia, Chan and Luke (2016) | | 2.88 | 3.38 | 25 | 10.34 | 1 | Dog-bone | – |
| | | | | Atmospheric Temperature | Atmospheric Pressure | 6 | Cylinders 50.8 (D)× 25.4 (H) | |

The data presented in Table 6.1 demonstrates that the cement class G mechanical inventory lacks uniaxial compressive strength and triaxial compressive properties corresponding to the different curing temperatures, particularly in long-term periods. It should be noted that the pre-peak and post-peak behaviour in the stress-strain graphs vary according to different specimen size and shape [105]. Table 6.1 shows the majority of studies were performed on cubic samples. While cylindrical specimens might be more suitable to be employed since cube tests provide higher

values (the uniaxial strength measured using sufficiently slender specimens is usually around 70%-90% of the cube strength [106]. In cubic samples, the restraining effect of the platens spreads over the total height of a specimen, but in cylindrical samples, some parts of specimens stay unaffected [107]. Another problem regarding using cubes is that the post-peak behaviour is milder in cubic specimens, therefore, requires more energy consumption than using cylinderial specimens. Additionally, the effect of specimen size is also larger for cubic samples [105].

Table 6.2 indicates that the measurement of tensile strength and particularly the fracture energy of cement class G, in particular over long-term periods, were simply overlooked in many experimental studies. The main problem with performing tensile measurement test is there are no API guidelines for measuring the tensile properties of cement, and ASTM standards for the measurement of tensile properties present various limitations when applied to cement tensile tests. This is because, these standards have been designed for cement cured at locations only a few meters down the ground and they do not incorporate the curing conditions considering downhole conditions in regards to high pressure and high temperature in harsh conditions, i.e. downhole conditions [97, 98]. This paucity of a complete inventory of cement class G mechanical properties can be an obstacle to performing precise integrity simulations. Subsequently, in this study, three-point bending tests were performed on notched and un-notched beams to measure the tensile strength and fracture energy.

The selection of an appropriate constitutive model for the cement as a geo-material and its corresponding failure surface parameters are the utmost of importance part of wellbore integrity modelling. This paper presents the results of an experimental study designed to fill the gaps above relating to the responses of cement class G in unconfined, confined compression tests, three-point bending tests. The results of the tests were interpreted to obtain the failure envelope of a constitutive model (Concrete Damage Plasticity Model [54, 115]) that was particularly formulated for quasi-brittle behaviour modelling. The model considers the differences in tensile and compression responses and the pressure-dependent nature of the cement's behaviour under shearing at different levels of confinement. In order to simulate the tensile response of the cement class G and address the gaps regarding fracture energy measurements, three-point bending tests were carried out using a modified method to obtain fracture energy by performing three-point bending tests.

This paper is organised as follows; section 6.2 describes the used material, the procedures curing and samples preparation. The effect of curing temperature on the cement mechanical properties is investigated in section 6.3 by performing the unconfined and confined tests on

samples cured at two different curing temperatures (30°C and 70°C). Section 3 also describes the execution of the three-point bending test on the prismatic samples cured at 30°C and the challenges involved with measuring fracture energy. Modifications are incorporated to the three-point bending test set-up, explained in section 6.4, to facilitate the measurement of fracture energy, followed by validation of the test performance by using Digital Image Correlations (DIC) cameras. In section 6.5 the outcomes of compression tests were interpreted to obtain the shape of yield surface of the Concrete Damage Plasticity (CDP) Model, followed by the curve fitting procedures to obtain the corresponding parameters and validation of them by the numerical analysis. Section 6.6 concludes the paper thereafter.

## 6.2. Material and Sample Preparation

The chemical and physical properties of the cement class G used in this study can be seen in Table 6.3. The slurry density was 1900 $kg/m^3$, corresponding to a water-to-cement mass ratio of 0.44. The slurry was prepared according to API-10 [138]. The cement class G samples were cured in a pre-heated water bath at two different curing temperatures (30°C and 70°C), for 28 days, to examine the effects of curing temperature on the mechanical properties of the cement class G.

*Table 6.3: Cement Class G Components*

| **Chemical Properties** | **Typical values %** |
|---|---|
| Sulfuric Anhydride (SO3) | 2.7 |
| Magnesia (MgO) | 1.1 |
| Tricalcium Aluminate (C3A)+ Tetra Calcium Alumino Ferrite (C4AF) | 15.5 |
| Tricalcium Aluminate (C3A) | 1.2 |
| Tricalcium Silicate (C3S) | 60 |
| **Physical Properties** | |
| Specific gravity | 3.18 |
| Free Fluid Content (%) | 4.5 |

### 6.2.1. Sample preparation

Samples were prepared in both cylindrical and prismatic shapes. The cylinder samples, at 42 mm diameter and a length of 100 mm, were used in compression tests. The prismatic samples, at

160×40×40 mm, were used in flexural tests. The specimens were cast in PVC moulds in the laboratory. They were then submerged in a water tank with an automatic thermostat, for curing at the specified temperature. The curing period began once the specimens were placed in the pre-heated curing bath and remained there for 28 days. Prior to testing, the surface of the cylindrical samples was ground to smoothness. For this purpose, the sample moulds were designed 3 mm taller than the desired sample length.

## 6.3. Investigation of the Effects of Curing Temperature on the Cement's Mechanical Properties

All of the experiments were carried out using a closed-loop, servo-controlled MTS machine, model 45, with a maximum load of 300 kN. In order to perform the triaxial tests 32-MPa-capacity 42 mm Hoek cell (ROCTEST, Model S/N 011S16004) was utilised. The lateral pressure was applied using a hand pump and controlled by a pressure gauge until the target lateral pressure was reached. The complete description of test set-ups and the corresponding test matrix is articulated in the Appendix I.

### 6.3.1. Unconfined compression test at curing temperature of 30°C

The first loading rate was determined according to API specifications [138] was applied as 72 kN ±7 kN per minute, converted to 0.2 mm/min, in which cement shows highly brittle behaviour. The effect of the displacement rate on the uniaxial compressive strength of the cement was

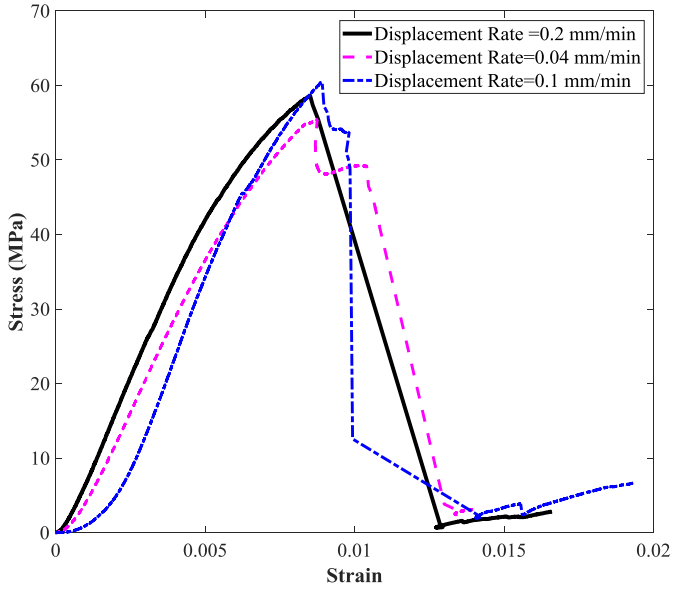


Figure 6.1: Axial Stress-Strain Response Using Three Different Strain Rates under Uniaxial Compression Test at Curing Temperature of 30°C

investigated by testing two slower rates: 0.1 mm/min and 0.04 mm/min, shown in Figure 6.1. The axial displacement of the loading platen was measured with the help of two external, linear, variable differential transformers (LVDT) that were installed $180^{o}$apart at the top platen.

As can be seen in Figure 6.1, the samples showed very brittle behaviour at a displacement rate of 0.2 mm/min and 0.1 mm/min. To capture post-peak behaviour, the displacement rate was reduced to 0.04 mm/min, at which rate the specimens showed less brittle behaviour. The slowest rate was therefore chosen as our settled displacement rate.

### 6.3.2. **Confined Compression Tests at the Curing Temperature of 30°C**

Triaxial compression tests with confining pressures ($P_c$) of 15 MPa and 30 MPa were performed after 28 days, on the samples that were cured at $30^{0}$C. The loading path was designed so that samples reached the desired confining pressure at the first step and were then loaded axially under displacement control until failure occurred. Figure 6.2 compares the results of two different confining pressures for specimens cured at $30^{0}$C.

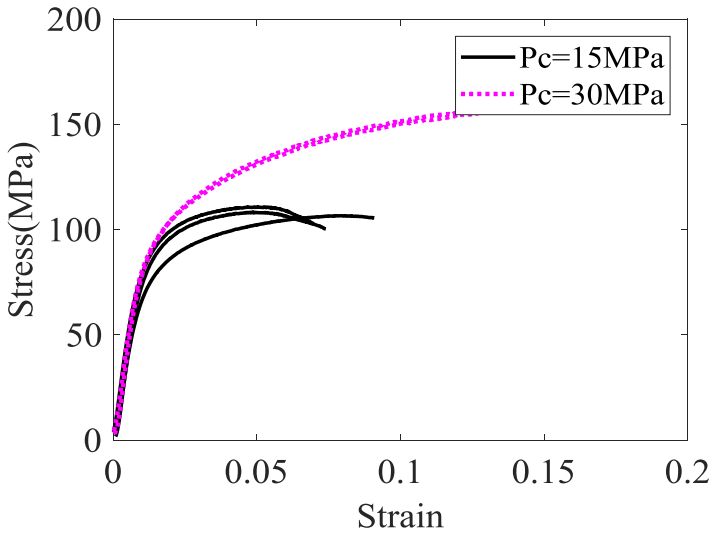


Figure 6.2: Axial Stress-Strain Response for Two Different Confining Pressures at Curing Temperature of 30°C

Figure 6.2 shows that the load-carrying capacity of the cement under higher confining pressure is significantly higher for the same axial strain. The response of the cement in the triaxial test does not illustrate a well-defined peak; the slope of the graph gradually decreased until it almost reached a plateau. The hardening process decreasing with an increased axial load is indicative of an increase in the effective compressive strength and ductility with confinement. This ductile behaviour at larger strains creates two macro-cracks without other distributed micro-cracks.

### 6.3.3. **Unconfined Compression Test at a Curing Temperature of 70°C**

To investigate the effects of curing temperatures on the mechanical properties of the cement, the samples were prepared as described in section 6.2.1 except for a change in curing temperature. For these tests, the temperature was set to $70^{o}$C. The rest of the test conditions, including the size of the samples, the curing period, and the water-to-cement ratio, were kept constant. Figure 6.3 shows the stress-strain curve obtained for three uniaxial compression tests on specimens cured at $70^{o}$C over 28 days.

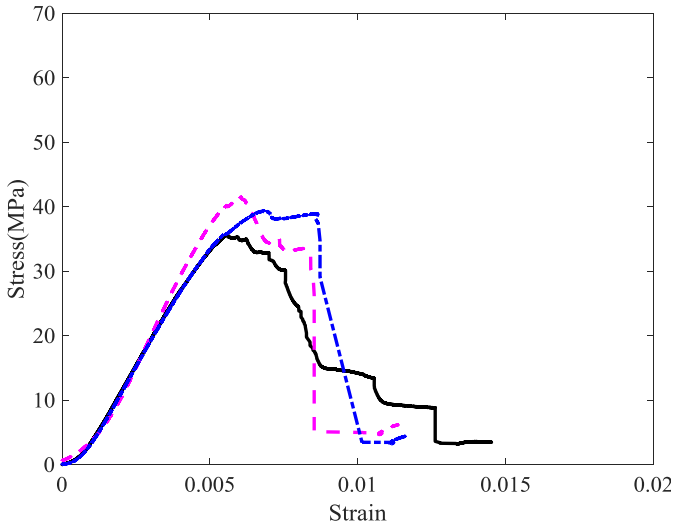


Figure 6.3: Axial Stress-Strain Response under Uniaxial Compression Test at Curing Temperature of 70°C

Comparing Figures 6.1 and 6.3 shows that increasing the curing temperature to $70^{o}$C, leads to an almost 27% strength reduction in uniaxial compression strength compared with curing at $30^{o}$C. The strength reduction at higher temperatures can be attributed to an increase in early strength, but a decrease in later strength (microstructural effect)[139]. Calcium Silicate Hydrates (C-S-H) is denser at higher temperatures, and thus occupies less volume, which leads to more porosity and less strength. Correspondingly, above 50°C ettringite becomes unstable and occupies less volume as well, which again leads to strength reduction [139].

### 6.3.4. **Confined Compression Tests at Curing Temperatures of 70°C**

Figure 6.4 shows the results obtained from triaxial tests with a confining pressure of 15 MPa on specimens cured at $70^{o}$C. The sudden termination of the plateau might be related to the quick propagation of macro-cracks, or to the breakage of the liner (membrane) within the Hoek cell, which leads to the entrance of oil and a loss of confinement.

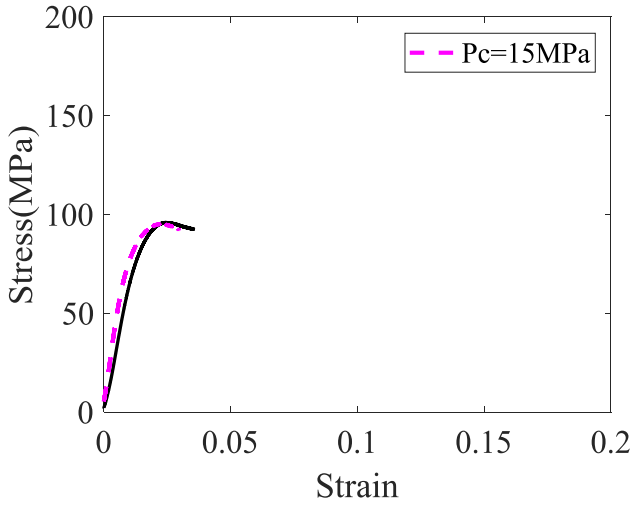


Figure 6.4: Axial Stress-Strain Response for Two Triaxial Tests with Confining Pressure of 15 MPa at Curing Temperature of 70°C

### 6.3.5. **Flexural Tensile Tests at a Curing Temperature of 30°C**

To determine the tensile stress of the cement according to ASTM standard C348-02, "Standard Test Method for Flexural Strength of Hydraulic-Cement Mortars" [120], three-point bending tests

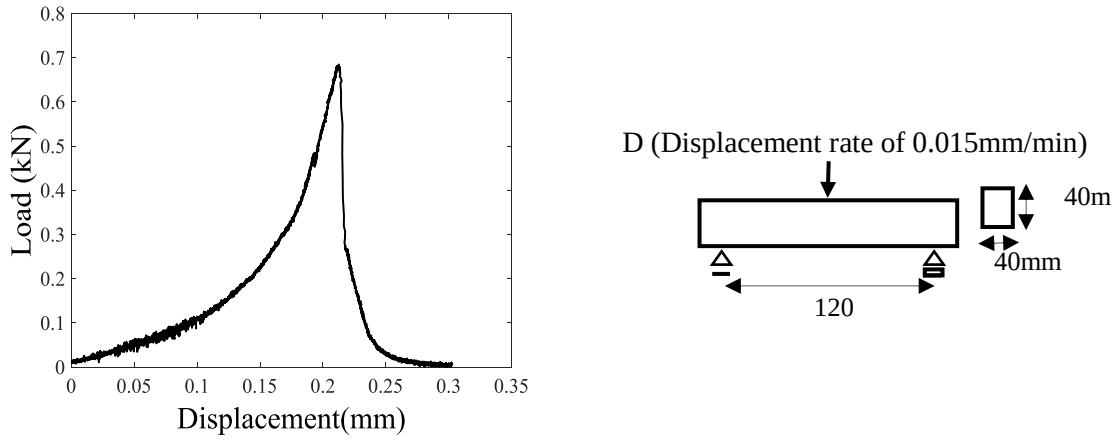


Figure 6.5: Measuring Flexural Strength of Cement Class G using Un-Notched Beams

were performed on un-notched and notched beams with dimensions of 160×40×40 mm, which cured at $30^{o}$C for 28 days. The loading rate of 2640 ±110 N (600 ±25 lbf/min) was suggested by the standards, however, according to RILEM recommendations [140] switching to displacement rate leads to more stable test. Therefore, the tests were performed by applying a displacement rate of 0.015 mm/min. The axial displacement of the loading platen was measured using one of two LVDTs installed on both sides of the beam specimens. The geometry of the un-notched samples,

and the graph obtained from the three-point bending test on one of the un-notched beams, are shown in Figure 6.5.

The tensile strength $\sigma_{t0}$ for prisms was calculated from the bending tests, as follows.

$$\sigma_{t0} = \frac{3FS}{2d_1 d_2^2} \tag{6.1}$$

where F is the maximum load, S is the span of the beam, $d_1$ is the width and $d_2$ is the depth of the beam [141]. As can be seen in Figure 6.5, the beam samples showed a highly brittle behaviour.

A notch of 5 ×15 mm was cut at the centre of the beams to measure the fracture energy according to the RILEM recommendations [140], on "Determination of the fracture energy of mortar and concrete by means of three-point bend tests on notched beams". The notch was cut 15 mm to meet the requirement of the RILEM standard, which states that the notch depth should be equal to half of the beam depth ± 5 mm. To record the load versus crack-mouth opening, a clip gauge (crack extensometer) was installed using two plastic plates glued to the bottom surface of the beam on each side of the notch. The rest of the test conditions, including the arrangement of LVDTs and the displacement rate, were kept identical to performing three-point bending tests on un-notched beams. The geometry of the notched beams, and the graph obtained from the three-point bending test on one of the notched beams is shown in Figure 6.6.

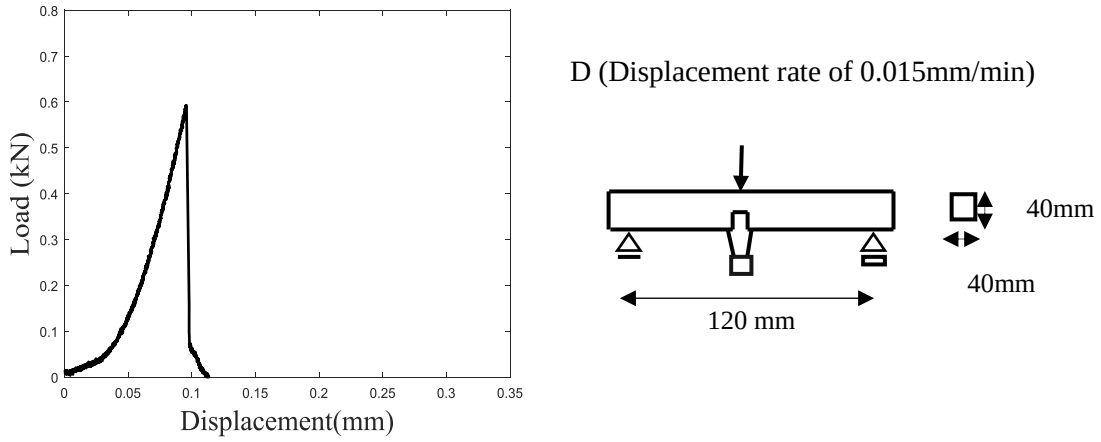


Figure 6.6: Measuring Fracture Energy of Cement Class G using Notched Beams

Fracture energy is calculated according to RILEM TC 50-FMC [140] using the below formulation.

$$G_f = \frac{U_o + mgd_o}{A} \tag{6.2}$$

where $U_o$is the area under the load-deflection is graph; A is the ligament area and defines as A = $B(W - a_o)$; B is the width of the beam; W is the depth of the beam; $a_o$ is the initial depth of the notch; mg is the weight of the beam; and $d_o$ is the final deflection at the load point.

As can be seen in Figure 6.6, the sample showed highly brittle behaviour, and the area under the load-displacement graph is very small.

The displacement rate was the slowest rate that the MTS machine could function. As the pattern repeated for all of the samples, the present authors concluded that there are some modifications required to be able to measure the fracture energy of cement class G.

## 6.4. Modification of the Three-Point Bending Test Configurations to Measure Fracture Energy

A different approach was undertaken to modify the test configuration so that we could capture the post-peak response. The testing device was a three-point bending set-up, mounted on a servo-hydraulic testing machine. The axial displacement of the loading platen was measured using two LVDTs installed on both sides of the beam specimens. To prevent post-peak, highly brittle crack propagation, the displacement rate was controlled by opening the crack mouth clip gauge instead of the crosshead displacement. The set-up configuration is shown in Figure 6.7.

Load Set Point= 0.1 kN

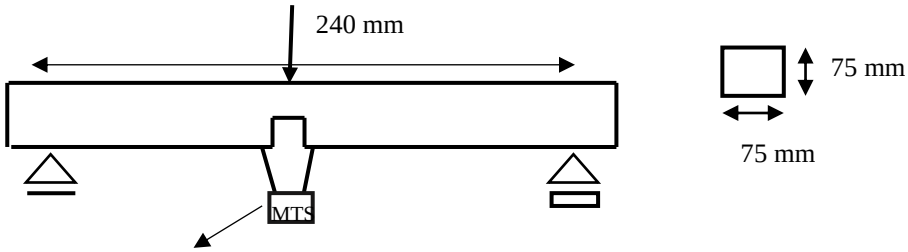


Clip Gauge Displacement Opening Rate = 0.001mm/min

Figure 6.7: Modification on Performing Three-point Bending Test

The clip gauge was installed between two plastic plates glued to the bottom surface of the beam, on each side of the notch. Until the applied load reached 0.1 kN the displacement rate was controlled by the crosshead, then the displacement rate was transferred to the opening of the crack mouth by the clip gauge. A non-contact strain measurement technique using two-dimensional digital image correlation (DIC) was applied simultaneously. The details of how we applied this optical technique are described in section 6.4.3.

For a beam in a three-point bending test, the load-deflection graph consists of three stages. In the first stage, the deflection rises linearly, as the load increases. A fracture process zone develops during the second stage, at which micro-cracks are created. In the third stage, which is a strain-softening zone, cracks grow quickly [33]. The fracture energy is calculated according to Equation (6.2).

### 6.4.1. Sample Preparation

The beam samples with the size of 280×75×75 mm were used. The specimens were cast in steel moulds in the laboratory. The slurry density and water-to-cement mass ratio were kept the same as the previous experiments. After casting, the samples were covered with a wet burlap for 24 hours. On the second day, all the samples were de-molded and transferred to a fog room. The samples were taken out of the fog room four hours prior to testing, and a saw-cut notch of 5 ×30 mm was made at the centre of the beams span.

### 6.4.2. Results

The obtained graph from one of the experiments is shown in the graph in Figure 6.8. The computed fracture energy, after three repeats of the test were performed, were 21, 24.64, and 23.44 N/m.

### 6.4.3. Digital Image Correlation (DIC)

Digital image correlation (DIC) is an optical and non-contact surface-displacement measurement technique. In this technique, surface images before and during the deformation are taken by digital cameras. Operating this technique allows the computation of any point displacements on the sample by the corresponding computer software using the taken images

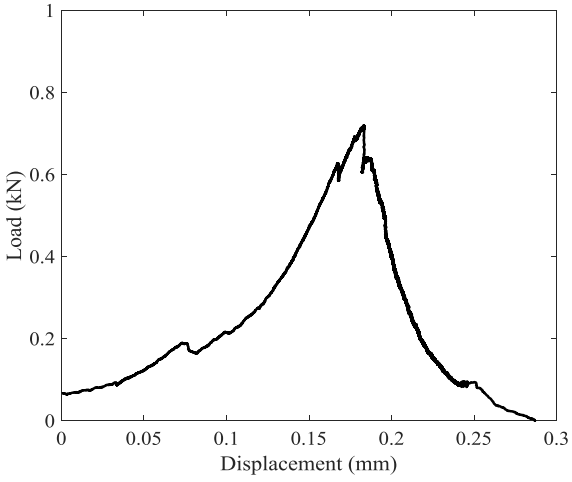




Figure 6.8: Measuring Fracture Energy of Cement Class G Undertaking the Modified Approach

before and during loading process [142-144]. The DIC system (3D) used in the experiments consisted of two monochrome 2.8-megapixel, conventional charge-coupled device (CCD) cameras. It had a sensor size of 1/1.8" and a maximum resolution of 1928×1448 pixels. The camera lens was a 75-mm Fujifilm prime lens with an aperture size range of 1/22-1/2.8. This lens has a minimal distortion, therefore, no correction for distortion was necessary. The camera body had a Universal Serial Bus (USB) 3 interface for the fast and reliable image transfer. The cameras were connected to a computer utilizing two software (Vic-Snap and Vic-2D) produced by Correlated Solutions. The Vic-Snap software arranges the process of capturing images while the specimens undergoes deformation. The Vic-snap software is utilised during calibration process and data analysing.

The deformation measurements were based on the displacements of random speckles spread over the surface of the sample. The speckle patterns should be applied in such a way to create contrast, by painting the whole surface of the sample with white, and then creating black speckles. The speckle pattern should be non-repetitive, well-distributed, and high contrast, to avoid any bias measurement, or sensitive defocus [142, 143, 145]. Figure 6.9 shows a typical speckle pattern on one the sample.

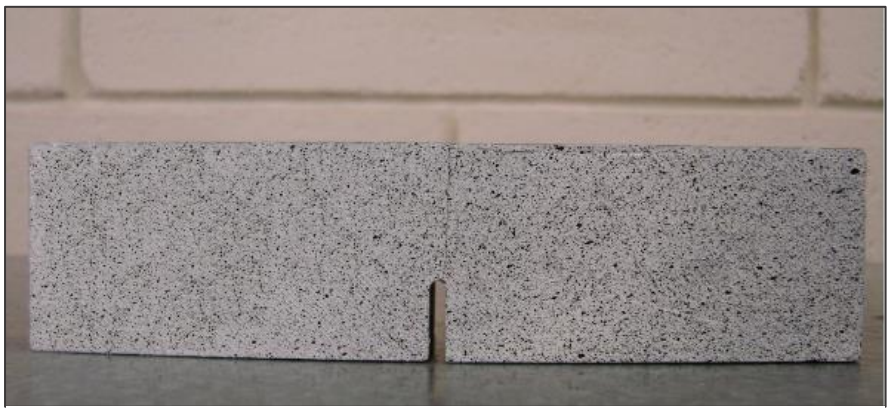

Figure 6.9: Speckle Pattern on a Prismatic Sample

To analyse the images after the test, an area of interest was chosen in which to detect the deformations and strain localizations. The surface displacement was computed by comparing the number of digital images taken during the test with the reference image (undeformed image). The correlation computations were based on tracing the same pixel points placed in different images. The displacement field inside a pattern is presumed to be homogenous [144]. The initial reference image, which is indicative of the undeformed body, is interpreted as a discrete function of $p(x_i, y_j)$; it is converted into another discrete function of $p'(x', y')$ after deformation. In order to compute the displacement of point p, a reference square subset of (2M+1)× (2M+1) pixels containing point

p $(x_o, y_o)$ from the reference image is selected and used for tracking the associated displacement in the deformed image [143]. The relationship between these two functions is defined as follows [144] .

$$p'(x', y') - p\big(x + u(x,y), y + v(x,y)\big) = 0 \tag{6.3}$$

where u(x, y) and v(x, y) are the displacement field for a pattern as shown in Figure 6.10. The $p'(x', y')$ coordination which is corresponding to the coordination of point $o(x_o, y_o)$ shown in Figure 6.10 in the reference image can be computed as follows.

$$x' = x_o + \Delta x + u + \frac{\partial u}{\partial x}\Delta x + \frac{\partial u}{\partial y}\Delta y \tag{6.4}$$

$$y' = y_o + \Delta y + v + \frac{\partial v}{\partial x}\Delta x + \frac{\partial v}{\partial y}\Delta y \tag{6.5}$$

where u, v are the displacements of the subset centre point o in x, y-direction, $\frac{\partial u}{\partial x}, \frac{\partial u}{\partial y}, \frac{\partial v}{\partial x}$, and $\frac{\partial v}{\partial y}$ are displacement gradients for the subset as shown in Figure 6.10.

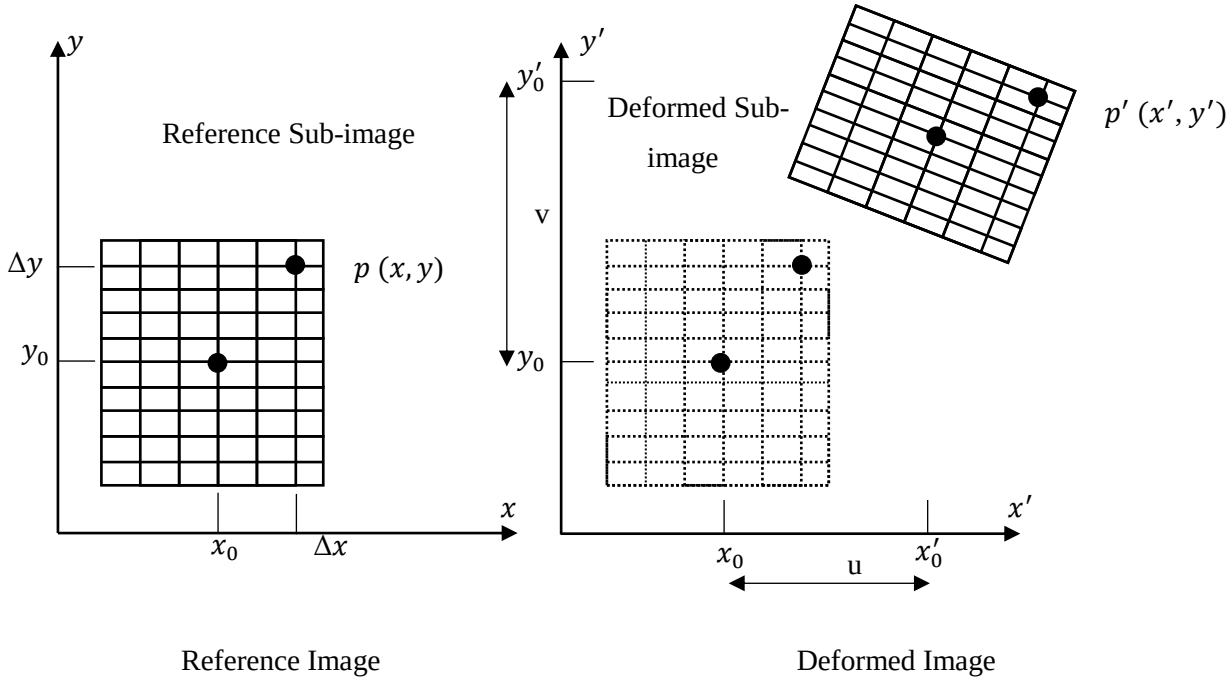


Figure 6.10: Reference image and deformed image schematics after [142]

A two-dimensional DIC technique was chosen for this study. To have an accurate 2D-image correlation, the alignment of the camera and specimen is crucial. The camera was set up planar and parallel to the specimen. The images were captured by Vic-snap software using an exposure time of 100 ms. Prior to the three-point bending test, the undeformed reference picture was taken,

along with a 20 mm pitch grid for calibration purposes. To examine the degrees of similarity between the reference and deformed image, a correlation criterion should be employed [143]. The default criterion is Normalised Sum of Square Difference (NSSD) [143] defines as follows.

$$C_{NSSD} = \sum_{i=-M}^{M} \sum_{j=-M}^{M} \left[ \frac{p(x_i, y_j)}{\bar{p}} - \frac{p'(x_i', y_i')}{\bar{p'}} \right]^2 \quad (i, j = -M{:}M) \tag{6.6}$$

where

$$\bar{p} = \sqrt{\sum_{i=-M}^{M} \sum_{j=-M}^{M} \left[ p(x_i, y_j) \right]^2} \text{ and } \bar{p'} = \sqrt{\sum_{i=-M}^{M} \sum_{j=-M}^{M} [\, p'(x_i', y_i')]^2} \tag{6.7}$$

The advantage of this DIC technique is that the displacement of crack openings can be measured in different directions on the surface. In this study, to validate the results obtained from the clip gauge (crack extensometer), the crack mouth opening displacements (CMOD) were also computed using a DIC technique (optical extensometer), as shown in Figure 6.11.

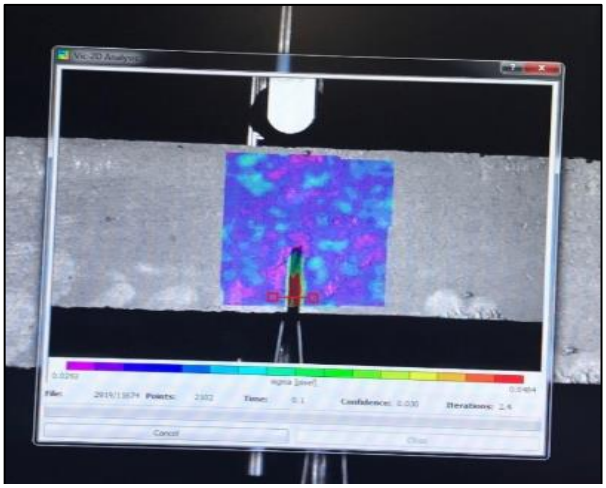

Figure 6.11: Optical Extensometer at the Crack Mouth using DIC Inspector Tool

Figure 6.12 demonstrates the results obtained from the clip gauge and DIC are in good agreement. However, the results from DIC show lesser displacement comparing to the clip gauge which seems possible. The clip gauge was installed at the centre of the beam along the beam thickness while DIC measurements are computed based on surface speckles displacements.

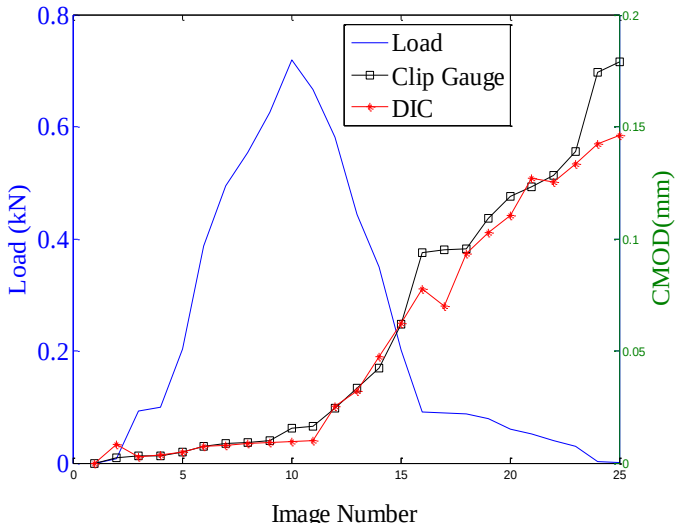


Figure 6.12: Load and CMOD versus DIC during the Three-point Bending Test

## 6.5. Interpretation of Results in the Concrete Damage Plasticity Model Framework

The non-linear behaviour of cement under compression can be modelled by plasticity or damage approaches, or a combination of both. Plasticity is described by means of the unrecoverable deformation after removing the load; damage is defined by the elastic stiffness reduction. Cement under compression exhibits both plasticity and damage [4]. Therefore, in order to simulate cement's mechanical behaviour under compression, it is of the utmost of importance to use a model in which both the plasticity and damage concepts have been embedded.

The stress-strain relationship subjected to uniaxial monotonic compression can be defined as:

$$\sigma = (1 - d)E_0(\varepsilon - \varepsilon_{pl}) \tag{6.8}$$

where d shows damage variable; $E_0$ is initial undamaged stiffness and is $\varepsilon_{pl}$ compressive equivalent plastic strains.

***Yield Criterion***

The yield function proposed by Lubliner, Oliver, Oller and Onate [54] and modified by Lee and Fenves [115] defines in $I_1$ and $\sqrt{J_2}$ plane as:

$$F(\sigma) = \frac{1}{1-\alpha}\left[\alpha I_1 + \sqrt{3J_2} + \beta\langle\sigma_{max}\rangle - \gamma\langle\sigma_{max}\rangle\right] = c(\kappa_c) \tag{6.9}$$

where α, β and γ are dimensionless constants calibrated by experiments; c is the compressive cohesion and its evolution is determined by uniaxial compression tests; $\kappa_c$ is the hardening-damage parameter; The cohesion stress c is to be scaled as its initial value is equal to initial yield strength in uniaxial compression ($f_{co}$). Subsequently, $c = f_{co}$ when $\kappa_c = 0$ and $c = 0$ when $\kappa_c =$

1; the Macaulay brackets < > are defined as $\langle x \rangle = (|x| + x)/2$ ; $I_1$ and $J_2$ are the first and second invariant of stress tensor in deviatoric stress state receptively.

The first two parameters α and β are calibrated according to uniaxial and biaxial tests as:

$$\alpha = \frac{(\frac{f_{bo}}{f_c}) - 1}{2(\frac{f_{bo}}{f_c}) - 1} \tag{6.10}$$

$f_{bo}$ is the biaxial compression strength;

$$\beta = (1 - \alpha)\left(\frac{f_{co}}{f_{to}}\right) + (1 + \alpha) \tag{6.11}$$

where $f_{to}$ is the initial uniaxial tensile yield stress.

The parameter γ appears in the yield function only in triaxial compression tests in which $\sigma_{max} < 0$ as follows.

$$\gamma = \frac{3(1 - K_C)}{2K_c - 1} \tag{6.12}$$

$K_c = \frac{(\sqrt{J_2})_{TM}}{(\sqrt{J_2})_{CM}}$ is a coefficient determined at a given state $I_1$ , $\sqrt{J_2}$ is the second invariant of stress with the subscripts TM and CM employed for the tensile and compressive meridians respectively. Figure 6.13 shows the initial and subsequent yield surfaces for triaxial compression in $I_1$and $\sqrt{J_2}$ plane and deviatoric plane.

On the yield surface $\sigma_{max}$ within tensile meridian (TM) in which $\sigma_1 > \sigma_2 = \sigma_3$ can be defined as:

$$\sigma_{max} = {}^1\!/_3\left(I_1 + 2\sqrt{3J_2}\right) \tag{6.13}$$

and $\sigma_{max}$ within compressive meridian (CM) in which $\sigma_1 = \sigma_2 > \sigma_3$ can be defined as:

$$\sigma_{max} = {}^1\!/_3\left(I_1 + \sqrt{3J_2}\right) \tag{6.14}$$

Therefore, the equations of TM and CM on the yield surface given that $\sigma_{max} < 0$ are shown below respectively.

$$(2\gamma + 3)\sqrt{3J_2} + (\gamma + 3\alpha)I_1 = 3(1 - \alpha)c(\kappa_c) \qquad \text{(TM)} \tag{6.15}$$

$$(\gamma + 3)\sqrt{3J_2} + (\gamma + 3\alpha)I_1 = 3(1 - \alpha)c(\kappa_c) \qquad \text{(CM)} \tag{6.16}$$

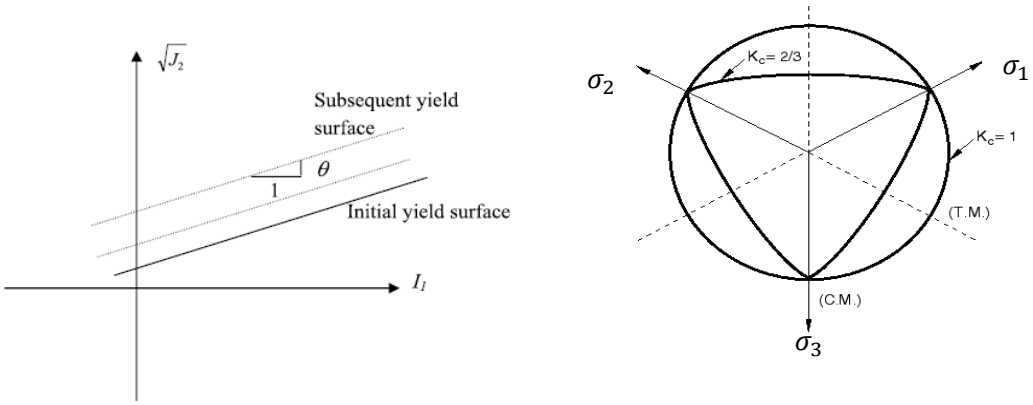


Figure 6.13: Yield Surfaces of the Concrete Damage Plasticity [4]

***Flow Rule***

The concrete damage plasticity model undertakes a non-associated plastic flow rule. The flow potential function G used in this model is the Drucker-Prager hyperbolic function as shown below [4].

$$G = \sqrt{\varepsilon \sigma_{to} \tan\psi + 3J_2} - \frac{I_1}{3}\tan\psi \qquad (6.17)$$

where ε defines as eccentricity, and it is indicative of the rate at which the function approaches the asymptote, $\sigma_{to}$ is the uniaxial tensile stress at failure, and ψ is the dilation angle measured in $I_1$-$\sqrt{J_2}$ plane.

A typical curve of the flow potential in the $I_1$-$\sqrt{J_2}$ plane is shown in Figure 6.14. When the concrete is under compression in all three direction results in the slope of the function to be very close to $\frac{\sqrt{3}}{9}\tan\psi$.

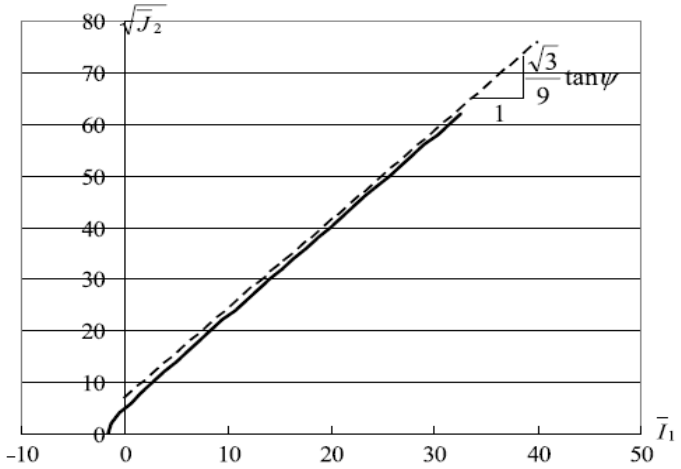


Figure 6.14: Drucker-Prager Flow Potential in the I1-√J2 Plane [4]

The parameters on the yield surface can be obtained using the experimental results. To approximate the shape of the loading/yield surface in $I_1$ and $\sqrt{3J_2}$ plane, the results of compression tests shown in Figure 6.15 (on samples cured at $30^o$C) at different confinements were used.

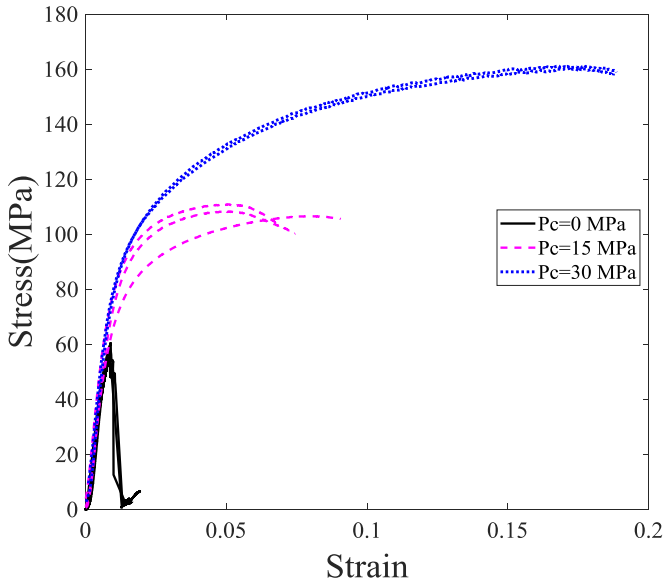


Figure 6.15: Compression Tests on Cylindrical Samples Cured at 30°C

The points in Figure 6.16 represent the initial yield strength (the turning point for each compression test in Figure 6.15). The points were fitted by the solid line in the graph to create the approximate shape of yield surface which delivers $\alpha = 0.08$ and $\gamma = 0.683$. Accordingly, $\frac{f_{bo}}{f_c}$ can be computed using Equation (6.10) which results in $\frac{f_{bo}}{f_c}$=1.10 and $\beta$ can be computed based on Equation (6.11) which yields to 27.8, and $K_c$ can be computed as 0.84 using Equation (6.12). Dilation angle $\psi$ can be computed using the slope of the line in the $I_1$-$\sqrt{J_2}$ plane as shown in Figure 6.14 using triaxial compression tests resulted $\psi$ =48.62$^o$.

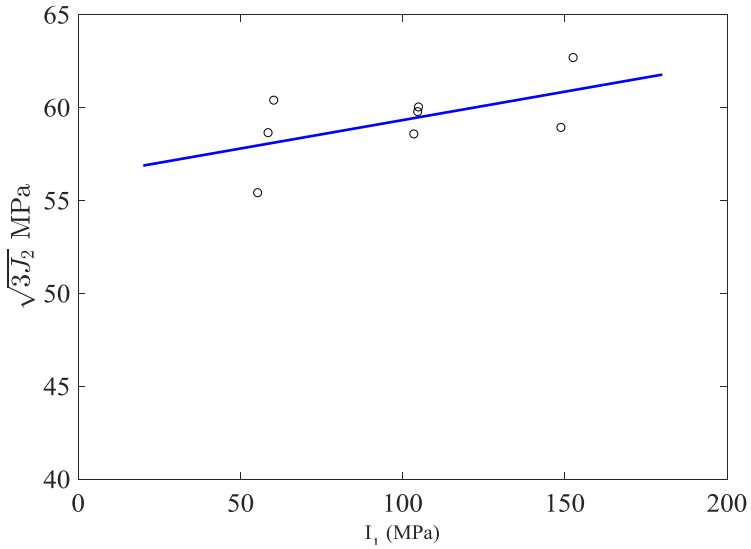


Figure 6.16: The Approximation of Yield Surface at 30°C in $I_1$ and $\sqrt{3}J_2$ Plane

### 6.5.1. **Concrete Damage Plasticity Parameters Validation for Cement Class G**

The obtained experimental parameters are to be calibrated and validated to ensure their suitability to predict the behaviour of cement class G. For this purpose; a three-dimensional uniaxial compressive test was simulated in ABAQUS / standard. The geometry and the boundary conditions are depicted in Figure 6.17. The size of the cylinder is defined the same as the size of the specimens used in the laboratory (D=42mm, L=100mm).

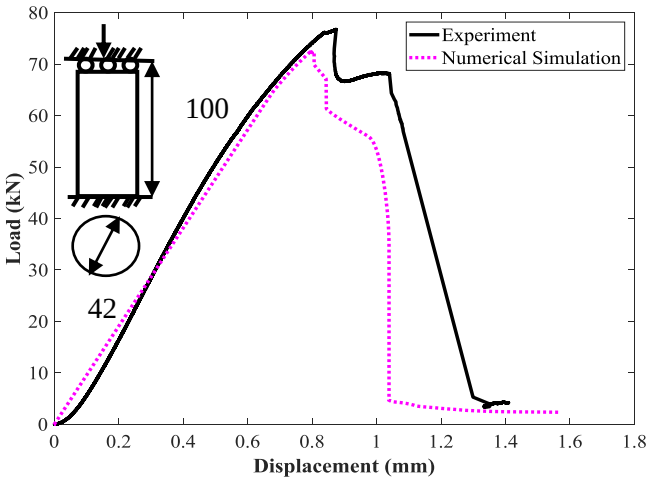


Figure 6.17: Concrete Damage Plasticity Parameters Validation

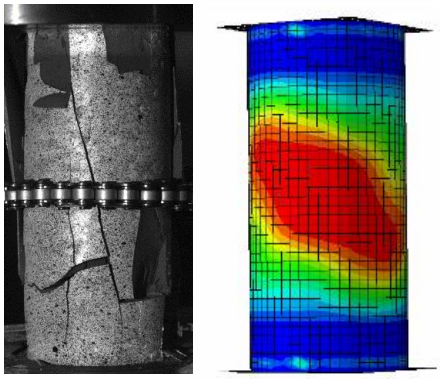

Figure 6.18: Failure Patterns in Uniaxial Compression Test

The cylinder was meshed using 17480 of 3-D triangular prisms elements. The platens were simulated by two discrete rigid parts with corresponding reference points; these rigid parts cannot

deform during the simulations. The defined boundary condition for the bottom surface constrains all the degrees of freedom, and the top surface displacement rate was applied in the direction of the cylinder axis.

The results and corresponding failure patterns in the laboratory and ABAQUS are shown in Figures 6.17 and 6.18. The displacement rate was applied in the normal direction of the upper surface. As can be seen, the simulation results can match the experimental counterparts in terms of both macro responses and failure pattern, demonstrating that the obtained set of parameters are appropriate for the modelling of the cement class G.

## 6.6. Conclusion

The cement sheath in wellbores is responsible for providing complete zonal isolation and maintaining the integrity of the wellbores. However, the cement class G inventory lacks some important aspects of cement mechanical properties which add uncertainty in the execution of numerical simulations of wellbore integrity assessments. This study intends to expand the inventory by performing compression tests considering different curing temperatures and indirect tensile tests.

The experimental results for confined and unconfined compression tests on cylindrical specimens of 42×100 mm, cured over 28 days at different temperatures ($30^{o}C$ and $70^{o}C$) were performed in this study. The key findings of the uniaxial compression tests were:

- A suitable loading rate was determined for uniaxial tests in order to achieve a converged post-peak response. The peak load was found to be dependent on the loading rate.
- Under uniaxial compression (unconfined), the response of the samples was accompanied with a well-defined peak load, followed by highly brittle, post-peak behaviour.

The triaxial testing of the cement properties revealed:

- The peak load was almost independent of the loading rate, within the range considered.
- The maximum strength of specimens increased significantly as the confining pressure increases.
- The specimens exhibited more ductile behaviour in confined compression tests in which the gradient of the load-displacement graph tends towards a plateau by the end of the test.

The effect of curing regime on the mechanical properties of the cement class G showed:

- The compressive strength of the material decreases significantly with increasing curing temperature. This can be attributed to the differences in the formation of calcium silicate hydrate (CSH) gels, due to an increase in the curing temperature.

Experimental results of three-point bending tests on prismatic samples demonstrate that it is possible to measure the fracture energy of the cement. A sufficiently slow test loading rate was controlled via the clip gauge measuring the crack mouth opening displacement. The results obtained from the clip gauge were validated by DIC technique measurements.

The approximate shape of the yield surface for elastoplastic models was obtained using the experimental data. The corresponding parameter intended for concrete damage plasticity was computed by the curve fitting process and were validated by numerical analyses. The incorporation of the obtained parameters leads to the more accurate implementation of concrete damage plasticity model in cement sheath integrity assessments.

**Acknowledgement**

The authors wish to express their gratitude to the laboratory technicians at the University of Adelaide for their assistance with the experimental work and to Leticia Mooney for her editorial assistance in improving this manuscript.

## 6.7. Appendix I

### MTS Criterion, Model 45 Description

The MTS machine (MTS Criterion, Model 45) was used with a maximum load capacity of 300 kN that was connected to a computer for command signals and data acquisition. The axial load was applied with displacement control. A 72-MPa-capacity 42 mm Hoek cell (ROCTEST, Model S/N 011S16004). The lateral pressure was applied using a hand pump and controlled by a pressure gauge until the target lateral pressure was reached. The axial displacement of the loading platen was measured with the help of two external, linear, variable differential transformers (LVDT) that were installed $180^{o}$apart at the top platen. For the three-point bending tests, in order to record the load versus crack-mouth opening, a clip gauge (crack extensometer) was installed using two plastic plates glued to the bottom surface of the beam on each side of the notch. The axial displacement of the loading platen was measured using one of two LVDTs installed on both sides of the beam specimens. Table 6.4 shows the test matrix with respect to all the performed experiments.

### Digital Image Correlation Cameras Description

The DIC system (3D) used in the experiments consisted of two monochrome 2.8-megapixel, conventional charge-coupled device (CCD) cameras. It had a sensor size of 1/1.8" and a maximum resolution of 1928×1448 pixels. The camera lens was a 75-mm Fujifilm prime lens with an aperture size range of 1/22-1/2.8. This lens has a minimal distortion, therefore, no correction for distortion was necessary. The camera body had a Universal Serial Bus (USB) 3 interface for the fast and reliable image transfer. The cameras were connected to a computer utilizing two software (Vic-Snap and Vic-2D) produced by Correlated Solutions. The Vic-Snap software arranges the process of capturing images while the specimens undergo deformation. The Vic-snap software is utilised during calibration and data analysing processes.

*Table 6.4: test matrix with respect to all the performed experiments.*

| Tests | Specimens (mm) | Number of specimens | Confining Pressure (MPa) | Instrumentation | Curing Condition ($^0C$) | Curing Time (days) |
|---|---|---|---|---|---|---|
| Uniaxial compression | Cylinder 42 ×100 | 3 | 0 | LVDTs | 30 | 28 |
| Triaxial compression | Cylinder 42 ×100 | 3 | 15 | LVDTs | 30 | 28 |
| Triaxial compression | Cylinder 42 ×100 | 2 | 30 | LVDTs | 30 | 28 |
| Three-point bending | Un-Notched Prism 40 ×40 ×160 | 3 | – | LVDTs | 30 | 28 |
| Three-point bending | Notched Prism 40 ×40 ×160 | 3 | – | LVDTs and clip gauge (crack extensometer) | 30 | 28 |
| Uniaxial compression | Cylinder 42 ×100 | 3 | 0 | LVDTs | 70 | 28 |
| Triaxial compression | Cylinder 42 ×100 | 3 | 15 | LVDTs | 70 | 28 |
| Three-point bending | Notched Prism 75 ×75 ×280 | 3 | – | LVDTs and clip gauge (crack extensometer) and DIC cameras | Ambient | 28 |

# 7. Evaluation of Cement Sheath Integrity Reflecting Thermo-Plastic Behaviour of the Cement in Downhole Conditions (PAPER-3)

E. Arjomand, T. Bennett., Evaluation of Cement Sheath Integrity Reflecting Thermo-Plastic Behaviour of the Cement in Downhole Conditions Prepared for Submission.

# Statement of Authorship

| | |
|---|---|
| Title of Paper | Evaluation of Cement Sheath Integrity Reflecting Thermo-Plastic Behavior of the Cement Sheath in Downhole Conditions |
| Publication Status | ☐ Published ☐ Accepted for Publication<br>☐ Submitted for Publication ☑ Unpublished and Unsubmitted work written in manuscript style |
| Publication Details | Arjomand, E., Bennett, T., Evaluation of Cement Sheath Integrity Reflecting Thermo-Plastic Behavior of the Cement Sheath in Downhole Conditions (2018). |

## Principal Author

| | | | |
|---|---|---|---|
| Name of Principal Author (Candidate) | Elaheh Arjomand | | |
| Contribution to the Paper | Development of finite element frameworks, implementation of constitutive modelling, results interpretation, and manuscript preparation. | | |
| Overall percentage (%) | 85% | | |
| Certification: | This paper reports on original research I conducted during the period of my Higher Degree by Research candidature and is not subject to any obligations or contractual agreements with a third party that would constrain its inclusion in this thesis. I am the primary author of this paper. | | |
| Signature | | Date | 25-06-2018 |

## Co-Author Contributions

By signing the Statement of Authorship, each author certifies that:

i. the candidate's statec contribution to the publication is accurate (as detailed above);

ii. permission is granted for the candidate in include the publication in the thesis; and

iii. the sum of all co-author contributions is equal to 100% less the candidate's stated contribution.

| | | | |
|---|---|---|---|
| Name of Co-Author | T. Bennett | | |
| Contribution to the Paper | • Conception & analyses.<br>• Analysis of results<br>• Drafting of manuscript | | |
| Signature | | Date | 25/6/2018. |

| | | | |
|---|---|---|---|
| Name of Co-Author | | | |
| Contribution to the Paper | | | |
| Signature | | Date | |

Please cut and paste additional co-author panels here as required.

# Evaluation of Cement Sheath Integrity Reflecting Thermo-Plastic Behaviour of the Cement in Downhole Conditions (PAPER-3)


## ABSTRACT

The cement sheaths play an important role to provide complete zonal isolation during the wellbores lifetime. The cement sheaths are subjected to pressure and temperature variations which may lead to different failure mechanisms and subsequently compromising the integrity of the wellbores. This paper demonstrates the results of three-dimensional finite element frameworks employing the Concrete Damage Plasticity (CDP) model for the cement sheath and a surface-based cohesive behaviour along with thermal conduction behaviour at the interfaces to assess the integrity of cement sheaths subjected to mechanical and thermal loads. The occurrence of the compression and tensile damage within the eccentric cement sheaths, and also the propensity of interfaces debonding were investigated considering different wellbore operational scenarios. Based on the simulations results controlled heating rates might lead to less potential compression damage. The tensile damage magnitude and its localisation are more dependent on the geometry of the wellbore instead of the heating rates, and the importance of casing centralisation was highlighted. The impacts of different cooling scenarios on the cement sheath damage were shown to be minimal due to the dominant effect of pressurizing the wellbore and the in-situ stresses confinement.



Keywords: cement sheath integrity, concrete damage plasticity model, wellbores architecture, thermal rates, compression damage, tensile damage


## 7.1.Introduction

The exploration and exploitation of hydrocarbon wells should be in agreement with the protection of the environment to prevent groundwater (aquifers) pollution [14, 15] and migration of fugitive emissions [16] into the atmosphere [9]. Groundwater sources are protected from the contents of well operational processes, i.e. drilling, pressure integrity tests (Leak-off tests), hydraulic fracturing, production operations, etc. by layers of steel casing, and cement sheaths which perform as multiple barriers to provide complete zonal isolation [17]. Although wellbores are sealed and block any interaction between formation fluid and geologic strata (which may contain groundwater), the integrity of wellbores might still be compromised [9, 18]. At this stage, wellbores may turn into the high-permeability conduits for the formation fluids [19] which induces a potential risk to the environment by contaminating the groundwater and atmosphere. To maintain the integrity of the wellbores, a wellbore barrier system should be designed in a way to endure the

mechanical and thermal operational procedures applied by the production and recovery phases during a well lifetime.

Well-cementing (cementation) is an important stage in the wellbore completion procedure as the cement sheath is responsible for maintaining the integrity of the wellbores [40]. The permeability of cement used in the oil and gas industry (cement class G) is very low, usually less than a 0.2 mD [38]. Therefore, the hydraulic isolation is straightforwardly achieved, and any probable leakage path can be created only through flaws in cement placement procedures or cement mechanical failures which result in the formation of cracks within the cement sheath /and formation of micro-annulus at the interfaces of cement sheath with the casing and the rock [11].

The mechanical and thermal stress state of a cement sheath is subjected to pressure and temperature variations due to different reasons for instances casing expansion/contraction [32], leak-off tests [23], hydraulic fracturing [33], loading from formation stresses such as tectonic stress, subsidence and formation creep [12], change of pore pressure or temperature [34], normal well production [12], injection of hot steam of cold water [35, 36], and cement hydration [146]. These operational procedures have significant effects on the integrity and failure mechanisms of cement sheaths. The integrity of the cement sheath is also dependent on cement mechanical properties [31, 44, 45], the cement bond strength [37, 47], cement history (cement shrinkage) [8], far-field stresses [48], and well architecture (cement sheath thickness, formation properties, cement sheath eccentricity, and wellbore deviation [8, 37]).

So far, different analytical and numerical modelling approaches were performed to achieve a better evaluation of cement sheath integrity in wells. The accuracy of analytical models and consequently their results are limited to the accuracy and suitability of their initial assumptions and employing simplifications to facilitate finding solutions [47]. On the other hand, numerical modelling including Finite Element Method (FEM) can be more practical with respect to its ability to incorporate material non-linearity, different types of geometry and boundary conditions, and in-situ stress conditions [47]. The reliability of these numerical models is conditional on the accessibility, validation, and verification of experimental data [47].

Up to now, the linear elastic approach was utilised in a few cement integrity analyses, i.e. [28, 37, 48, 49]. Li, Liu, Wang, Yuan and Qi [48] developed a coupled framework to investigate the effect of non-uniform in-situ stress filed, temperature, and pressure effects on wellbore integrity. The stress states evaluated assuming the linear elastic behaviour for all the materials. According to this study, the anisotropy of in situ stresses resulted in the creation of shear stresses and non-uniform stress distribution within the cement sheath. By increasing the casing temperature, the

tensile stresses develop and lead to the creation of fractures in the inner surface of the cement sheath.

Guo, Bu and Yan [49] presented a numerical study to investigate the effect of the heating period, cement thermal expansion, and overburden pressure on the cement integrity under steam stimulation conditions. All materials presumed to be linear elastic. They recommended a moderate heating rate and moderate cement thermal expansion coefficient is beneficial to maintain the cement sheath integrity.

De Andrade and Sangesland [66] conducted a numerical study with a particular focus on thermal-related load cases. They built a two-dimensional (2-D) model and assumed a linear elastic behaviour for all the materials, bonded contact between wellbore components and isotropic in-situ stresses. A utilisation factor based on Mogi-Coulomb criterion was defined to check the state of the stress and estimate cement sheath failure. The utilisation of Mogi-Coulomb criterion instead of Mohr-Coulomb was explained by considering the obtained experimental data by Al-Ajmi [67] which states Mogi-Coulomb criterion represents the state of shear failure in different types of rocks better than Mohr-Coulomb criterion. According to their results, during heating procedures, the failure of the cement sheath may occur due to shear stress, and the possibility of debonding failure during cooling procedures is high. Based on their results, the effect of casing centralisation and controlled heating/cooling rates seemed to be trivial.

Roy, Morris, Walsh, Iyer, Carroll, Todorovic, Gawel and Torsæter [60] carried out an experimental-numerical study to investigate the effect of wellbore size, cement Young's modulus, and different cooling rates on the imposed thermal stresses during $CO_2$ injections. They coupled a finite element solver assuming linear elastic materials with a finite volume heat equation solver to simulate the mechanical response of the materials exposed to thermal loading. Their observations showed the variation of cement Young's modulus effects the magnitude of maximum radial stress at the interface of cement and casing or the interface of cement with the formation. They also showed the overall stress within different wellbore components is more dependent on the temperature gradient rather than the temperature difference between the initial and ultimate state in materials.

Although the linear elastic approach has been used in some studies including the aforementioned studies, the obtained stress-strain curves from the isotropic drained compression tests on the cementitious specimens by [36, 72] are shown to be non-linear. Therefore, the employment of linear elastic theory in cement integrity simulations troubles the accuracy and reliability of the results. Additionally, the existence of the permanent strains upon unloading [36]

confirms the incompatibility of linear elastic theory in cement integrity evaluations again as the elastic theory does not incorporate the time-dependency and materials hysteresis law [50].

The non-linear approaches including those using Von-Mises [51], Ottosen model [5, 53], Drucker-Prager [52], modified Cam-Clay [36], and Mohr-Coulomb / with smeared cracking [31, 44] were incorporated in the cement sheath integrity evaluations to alleviate the shortcomings of the linear elastic models.

Fleckenstein, Eustes and Miller [51] employed the von-Mises criteria and showed that the magnitude of tangential stresses would be significantly reduced if the cement sheath acts as a ductile material with lower Young's modulus and higher Poisson's ratio. The lack of pressure dependency of the von Mises criteria is however problematic in modelling cementitious materials.

Asamoto, Le Guen, Poupard and Capra [5], Guen, Asamoto, Houdu and Poupard [53] developed a 2-D model using the Ottosen model [71] as a smeared crack model to investigate the softening post-peak behaviour of the cement sheath and the estimation of the crack width in a wellbore subjected to thermal and mechanical loads. Guen, Asamoto, Houdu and Poupard [53] examined the effect of temperature and pressure changes on the thermo-mechanical response of a wellbore for the application to Ketzin injection well using FEM. The interfaces of cement-casing and cement-rock were modelled using joint elements with Mohr-Coulomb failure criterion. They concluded that the possibility of debonding as a result of $CO_2$ injections is very low, except in the scenarios with a very high degree of eccentricity (85% eccentricity) in which the cement tangential stress would exceed the cement sheath tensile limit. In both studies, the details of the constitutive model performance and the relevance of the constitutive parameters to the experimental data are not described.

Zhang, Yan, Yang and Zhao [52] developed an analytical plain-strain model to evaluate the integrity of a wellbore under HPHT conditions coupling displacement and temperature approach. The Mises criterion, Drucker-Prager, and Joint Roughness Coefficient-Joint wall Compressive Strength (JRC-JCS) were utilised to model the casing, cement sheath and cement interfaces respectively. According to their parametric study, using cement with low Young's modulus and high Poisson's ratio improves wellbore ability to maintain its integrity. However, the studies carried out on the performance of Drucker-Prager model shows this model does not provide accurate predictions while one or more principle stresses are tensile stress. Additionally, considering the same effect for $\sigma_2$ and $\sigma_3$ leads to overestimation of rocks' strength and it is not verified by laboratory experimental data [69, 70].

The modified Cam-Clay model has been suggested as a method to incorporate cement micro cracking mechanisms by Bois, Garnier, Rodot, Sain-Marc and Aimard [36] owing to the nonlinearity of stress-strain curve achieved from the isotropic drained compression tests [72] and heterogeneous nature of cement at the microscale. Although important aspects of materials behaviour (material strength, compression or dilatancy, and critical state of elements under high distortion) are considered in this model, the tensile post-peak material is not incorporated into this framework.

Bosma, Ravi, van Driel and Schreppers [44] developed a two-dimensional (2-D) model incorporating Mohr-Coulomb plasticity combined with smeared cracking to model the cement sheath under compression/shear and tension along with heat transfer phenomena. The cement sheath interfaces were modelled using interface elements applying a coulomb friction criterion. Their results showed that cement sheath failure is happened because of shear stresses caused by in situ stresses or either due to tensile failure mechanisms which is more likely when the cement Young's modulus is higher than the rock.

Ravi, Bosma and Gastebled [31] developed a 2-D model to investigate the wellbores integrity subjected to operational procedures. To model the stress state within the cement sheath, the Hookean model was incorporated for undamaged state and combined Mohr-Coulomb plasticity with smeared cracking after exceeding the compressive shear and tensile strength state. According to their findings, the integrity of the cement sheath is highly dependent on the cement and mechanical rock properties, and well-operating parameters. Moreover, cement sheath with less stiffness shows more resilient and helps to reduce the risk of cement sheath failure.

Mohr-Coulomb criterion was also used by Feng, Podnos and Gray [50], Nygaard, Salehi, Weideman and Lavoie [74], and Zhu, Deng, Zhao, Zhao, Liu and Wang [75] to predict the plastic behaviour of the cement sheaths subjected to mechanical and thermal loads.

The combination of Mohr-Coulomb with smeared cracking is one of a few suitable approaches for modelling the real conditions in the cement integrity numerical simulations. However, despite the broad application of Mohr-Coulomb criteria, it has its own limitations. The model assumes a linear relationship between $\sqrt{J_2}$ and $I_1$ in the meridian plane, while this relationship has been experimentally shown to be curved [36, 72, 76, 77], for cementitious materials, particularly at low confinement. The major principal stress $\sigma_1$ and intermediate principal stress $\sigma_2$ are defined independently in Mohr-Coulomb model which results in an underestimation of the yield strength of the material and, it is not in a good agreement with experiments in which the effect of $\sigma_2$ is being considered. The shape of the yield surface in the deviatoric plane is an asymmetrical

hexagon, whereby the sharp corners can hinder convergence in numerical simulations [70, 78]. Moreover, quasi-brittle materials experience a huge volume change due to a large amount of inelastic strains (dilatancy) which has been overlooked so far by using associated flow rules in the aforementioned modelling approaches of the cement sheath. The associative plastic flow rules tend to lead to poor results in dilatancy evolution [55].

The application of plasticity theory in compression (Mohr-Coulomb) combined with the fracture mechanics models such as smeared cracking presents some drawbacks as well. Given that, smeared crack models in finite element analysis can often be problematic in terms of "mesh alignment sensitivity" or "mesh orientation bias" which indicates that the orientation of smeared crack depends on the discretization orientation [79]. It is worth adding that the mesh regularization approach proposed by [56] (crack band theory) in the smeared cracking model has been successful for predicting mode I fractures while the extension of this approach to mixed-mode failure and three-dimensional stress state is hard [79].

Wellbore integrity modelling has been significantly progressed regarding complexity and capacity to assess the integrity of wellbore barriers. However, some aspects of wellbore integrity modelling still require improvements, in particular, the incorporation of appropriate cement constitutive law. The softening aspects of constitutive models, and subsequently, the evolution of corresponding cement constitutive parameters requires more attention to achieve a reliable and efficient model. Considering these limitations, it would be practical to employ more suitable models with respect to their accuracy (enrichment) and reliability (capability to reproduce the experimental data) along with their efficiency (mesh orientation and mesh size objectivity) [79].

In this paper, the Concrete Damage Plasticity model (CDP) specifically formulated for the modelling of geo-materials developed and modified by [54, 55] is utilised. The major advantage of Concrete Damage Plasticity (CDP) model is coupling plasticity with damage mechanism which explains the elastic stiffness degradation of materials clearly during the experiments due to the formation of microcracking. The formation of microcracks which is also characterized as softening behaviour of the materials is difficult to describe applying classical plasticity models [55]. The modified version of CDP by [55] benefits from considering the difference in tensile and compressive responses of geo-materials as these materials undergo different states of damage while being subjected to different loading conditions. This model also takes into account the materials pressure-dependency behaviour under shearing at different levels of confinement. The non-associated flow rule which represents the dilatancy of the geo-materials is also embedded into this model. These features make this model a very suitable model to be applied to the range of

geo-materials including rocks, and cement-based materials [55] compared to the rest of model used . The corresponding CDP model parameters were obtained from the previous experimental-numerical study on cement class G by [116, 147].

In this paper, the susceptibility and magnitude of compression damage, tensile damage, and interfaces debonding in the cross-sectional slices of two wellbores are investigated considering different well-operating scenarios. The parametric study is carried out to assess the effect of wellbore architecture (e.g. eccentricity, different layers of cement sheath and casing), different heating and cooling rates on the integrity of cement sheath.

This paper is organised as follows; section 7.2 describes an overview of the finite element frameworks including wellbore geometries, initial states of the stresses, the mechanical and thermal behaviour of interfaces modelling, and material properties (i.e. cement constitutive modelling). The effect of enhanced pressure and temperature on wellbore-1 is investigated in section 7.3. Section 7.4 and 7.5 investigate the effect of heating and cooling scenarios along with an applied pressure respectively. The propensity of compression and tensile damage with respect to heating and cooling scenarios are examined and also compared in these two sections. Section 7.6 describes the susceptibility of forming micro-annuli at the interfaces of cement sheaths in wellbore-2 due to the heating and cooling operational procedures followed by conclusion in section 7.7.

## 7.2. Overview of Finite Element Modelling

Three-dimensional finite element frameworks were developed to investigate the effect of pressure and temperature variations events on the cement sheath integrity using ABAQUS / Standard software package. 8-node thermally coupled brick, trilinear displacement and temperature elements were utilised to mesh the system components. A fully coupled transient thermal-stress analyses procedures were undertaken. Different scenarios were chosen to investigate the effect of different well operational procedures in completion stages. Figure 7.1 demonstrates wellbore schematic sections. The information regarding wellbore-1 is based on an actual site on Ketzin, Germany [5, 148], while, wellbore-2 is a case study selected to examine the effect of different thermo-mechanical loading scenarios, and wellbore architecture (different degrees of eccentricity) on the cement sheaths integrity.

The heating and cooling scenarios represent the different operational procedures leading to pressure and temperature variations applied to wellbore-2. For instances, during the commencement of production procedures, the pressure and temperature are increased within the wellbores to enforce the hydrocarbon flow from the reservoir [66], and in the start of injection procedures, wellbores are cooled down for the fluid to flow into the reservoir [66].

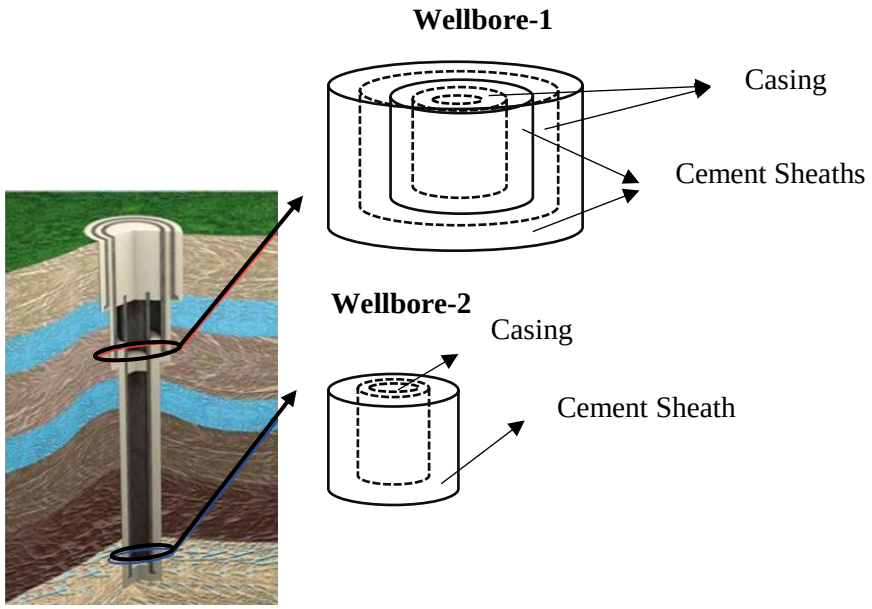


Figure 7.1: Wellbores Schematic Sections after [5]

In Abaqus/standard the temperatures are integrated utilising a backwards-difference scheme, and non-linear coupled system is solved using Newton's method. The exact implementation of Newton's method for fully coupled temperature-displacement was applied involving a non-symmetric Jacobian matrix as shown in the following equation [57].

$$\begin{bmatrix} K_{uu} & K_{u\theta} \\ K_{\theta u} & K_{\theta\theta} \end{bmatrix} \begin{Bmatrix} \Delta u \\ \Delta\theta \end{Bmatrix} = \begin{Bmatrix} R_u \\ R_\theta \end{Bmatrix} \tag{7.1}$$

where $\Delta u$ and $\Delta\theta$ are the respective corrections to the incremental displacement and temperature, $K_{ij}$ are submatrices of the fully coupled Jacobian matrix, and $R_u$ and $R_\theta$ are the mathematical and thermal residual vectors respectively.

Unsymmetrical matrix storage and solution scheme should be undertaken to solve the system equations. The mechanical and thermal equations must be solved simultaneously.

The governing equations are as follows [149].

Kinematic relation:

$$\varepsilon_{i,j} = \frac{1}{2}\left(u_{i,j} + u_{j,i}\right) \tag{7.2}$$

Motion equation:

$$\sigma_{ij,j} + \rho F_i = \rho \ddot{u}_i \quad , \quad \sigma_{i,j} = \sigma_{j,i} \tag{7.3}$$

where $\rho$ is the mas density, and $F_i$ is external force per unit mass, .

Energy-scale equation:

$$q_{i,i} + \rho(T_o \dot{s} - R) = 0 \tag{7.4}$$

where $q_i$ is the heat flux per unit area, $T_o$ is the initial temperature, s is entropy per unit mass, and $R$ is internal heat capacitance per unit mass.

Constitutive equations:

$$\sigma_{i,j} = C_{i,jkl}\varepsilon_{kl} + \beta\theta \tag{7.5}$$

where $C_{i,jkl}$ is the stiffness tensor, $\beta$ is thermal stress, and $\theta$ is the temperature difference.

$$q_i = -k_{i,j}\theta_{,j} \text{ and } \rho s = \frac{\rho c}{T_0}\theta - \beta\varepsilon_{i,j} \ , \beta = \frac{E\alpha}{(1-2\vartheta)} \tag{7.6}$$

where $k_{i,j}$ is the thermal conductivity tensor, c specific heat per unit mass at constant strain, $T_0$ is the initial temperature, $E$ and $\vartheta$ are Young's modulus and Poisson's ratio respectively, and $\alpha$ is coefficient of linear thermal expansion.

From the equation of motion (7.2) and the energy-scale equation (7.4) using the constitutive equations (7.5) -(7.6) the general basic equations will be obtained as follows.

$$(C_{i,jkl}\varepsilon_{kl})_{,j} + (\beta\theta)_{,j} + \rho F_i - \rho\ddot{u}_i = 0 \tag{7.7}$$

$$(k_{i,j}\theta_{,j})_{,i} + \rho c\dot{\theta} + \rho R - T_0\beta\dot{\varepsilon}_{i,j} = 0 \tag{7.8}$$

### 7.2.1. Initial State of Stress and Boundary Conditions

The anisotropic geo-stress components ($\sigma_H$ and $\sigma_h$) were applied in the initial step of the analyses. The geo-stresses information were extracted from a geo-mechanical study performed by Ouellet, Bérard, Desroches, Frykman, Welsh, Minton, Pamukcu, Hurter and Schmidt-Hattenberger [148] on the Ketzin site. The anisotropy of geo-stresses would cause further shear stresses to the wellbore [82] and is required to be considered in cement integrity modelling. An overburden stress gradient of 22.6 $\frac{\text{kPa}}{\text{m}}$ was assumed. The ratio of maximum horizontal stress to

overburden stress $\left(\frac{\sigma_H}{\sigma_V}\right)$ and the ratio of ansitropic in-situ stresses $\left(\frac{\sigma_H}{\sigma_V}\right)$ is assumed to be 0.8 and 0.7 respectively. The variation of overburden (vertical) initial stress in depth is negligible since the ratio of model height to the width is comparatively small. The corresponding overburden effective stress at the casing shoes were computed according to the located depth and formation density, and all shear components are assumed to be zero. The displacement constraints were applied to the normal direction of the bottom surface, the outer surface of the formation, and the symmetric surfaces.

### 7.2.2. Interface Modelling

The cement sheath interfaces with the casing and the formation are recognised as the weakest components to provide an effective leakage barrier [37, 81, 150]. The mechanical behaviour and failure of the interfaces can be described by a cohesive model for interfaces between two different materials [151]. In this study, the mechanical behaviour of cement sheath interfaces is represented by surface-based cohesive behaviour accompanied by the thermal interaction properties to model heat conduction at the interfaces.

#### 7.2.2.1. Mechanical Behaviour of the Interfaces

The mechanical behaviour of the cement sheath interfaces is modelled by defining surface-based cohesive behaviour as a surface interaction property with traction-separation capacity. Traction-separation $(t - \delta)$ law can be expressed by different relationships for various materials, and according to the studies by Hillerborg, Modéer and Petersson [131] bilinear or triangular traction separation law had successful applications on brittle materials such as cementitious

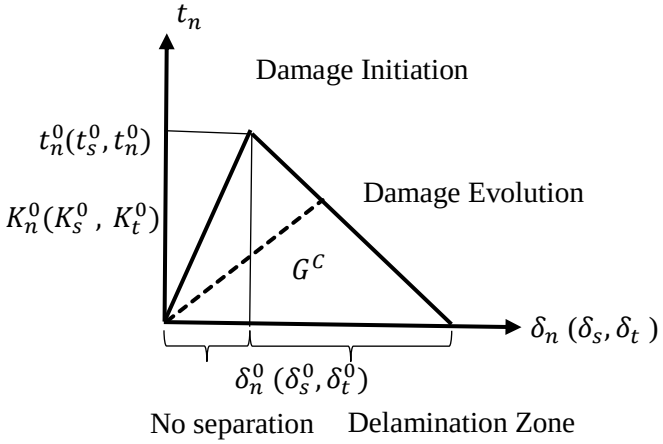


Figure 7.2: Linear Softening Traction-Separation Law

materials. Figure 7.2 shows the triangular traction separation law.

where the superscript 0 denotes the maximum traction or initiation traction value, $\mathrm{n}, \mathrm{s}, \mathrm{t}$ are representing the normal and shear directions respectively, and K represents the contact stiffness. The dashed-line demonstrates the stiffness degradation after the peak. Equation (7.9) describes a linear relationship traction-separation $(\mathrm{t}-\delta)$ law.

$$\{t\} = \begin{Bmatrix} t_n \\ t_s \\ t_t \end{Bmatrix} = \begin{bmatrix} K_{nn} & K_{ns} & K_{nt} \\ K_{sn} & K_{ss} & K_{st} \\ K_{tn} & K_{ts} & K_{tt} \end{bmatrix} \begin{Bmatrix} \delta_n \\ \delta_s \\ \delta_t \end{Bmatrix} = K\{\delta\} \tag{7.9}$$

The damage mechanism is defined based on damage initiation criterion and damage evolution law. The damage initiation between two different materials is usually described by mixed modes condition [152] via using quadratic nominal stress criterion.

Damage is assumed to initiate once a quadratic interaction function relating the nominal stress ratios (as defined in the expression below) reaches one. This criterion can be defined as:

$$\left\{\frac{\langle t_n \rangle}{t_n^0}\right\}^2 + \left\{\frac{t_s}{t_s^0}\right\}^2 + \left\{\frac{t_t}{t_t^0}\right\}^2 = 1 \tag{7.10}$$

where $t_n$ , $t_s$ , and $t_t$ are the normal and shear tractions across the interfaces and the superscript 0 denotes the maximum traction or initiation traction value.

Damage evolution law describes the process of failure and the rate at which the material stiffness is degraded when the corresponding initiation criterion is met. To study the mixed-mode condition, the Benzeggagh-Kenane (BK) [133] fracture energy criterion is used here with the assumption that the critical fracture energy during separation along the first and the second shear direction are the same; $G_s^C = G_t^C$.

$$G_n^C + (G_s^C - G_n^C)\left\{\frac{G_S}{G_T}\right\}^\eta = G^C \tag{7.11}$$

where $G_S$=$G_s + G_t$ , $G_T = G_n + G_S$ and $\eta$ is a cohesive property parameter [82, 87, 134].

***Determination of Cohesive Model Parameters***

Carter and Evans [84], Evans and Carter [86] designed a push-out test setup to measure cement shear bond and hydraulic bond. Shear bond is essential to support the pipe mechanically, whereas the hydraulic bond prevents the formation of micro-annuli. They designed cylindrical chambers in which shear bond is determined by applying force to instigate the movements of the pipe surrounded by cement. The shear bond measured as dividing the force to the contact surface area. The cement hydraulic bond was defined as the cement bond to the casing or the formation which prevent the fluid migration. Hydraulic bond was determined by applying pressure to the cement interfaces until leakage happens. Ladva, Craster, Jones, Goldsmith and Scott [85] repeated the above experimental procedures using cement class G to measure the shear bonding between

cement and formation. Afterwards, Wang and Taleghani [37] performed inverse analyses on the experimental results of [84-86] to determine the cohesive parameters. Table 7.1 summarised the obtained cohesive parameters by Wang and Taleghani [37] adopted in this study to model the mechanical behaviour of the interfaces.

*Table 7.1: Cohesive properties of cement / casing and cement/rock [37]*

| **Cohesive Properties Interfaces** | **Shear Strength (kPa)** | **Normal Strength (kPa)** | **Cohesive Stiffness (kPa)** | **Critical energy ($J/m^2$)** |
|---|---|---|---|---|
| Casing/Cement Interface | 2000 | 500 | $30E^6$ | 100 |
| Cement/Formation Interface | 420 | 420 | $30E^6$ | 100 |

Although the cohesive parameters have been determined from a number of experimental studies, uncertainty still remains in the utilisation of these parameters. Since as stated by Carter and Evans [84], Evans and Carter [86]'s studies the cement shear bond to the casing is dependent on curing temperature, the pipe condition, and variations of different cement brands. The adherence degree of well cement to rock is highly variable and site dependent. The cement hydraulic bond to the casing and formation is dependent on the type of the formation, the surface finish of the pipe, type of mud layer, and degree of mud removal [85, 135].

#### 7.2.2.2. Thermal Conduction Behaviour of the Interfaces

The defined thermal contact properties at the interfaces allow the conductive heat transfer between the surfaces. The thermal conductivity at the contact surfaces is formulated using Equation (7.12) :

$$q = k(T_A - T_B) \tag{7.12}$$

where q is the heat flux per unit area crossing the interface from node A on the slave surface to node B on the opposite surface (master surface), k is the gap conductance, and $T_A$ and $T_B$ are the temperatures of the nodes in the contact surfaces [153].

The gap conductance coefficient decreases linearly as the clearance increases due to the creation of gaps and flaws between the contact surfaces as shown in Figure 7.3. The effect of surrounding temperature on the gap conductance coefficient is not seen in this study also the

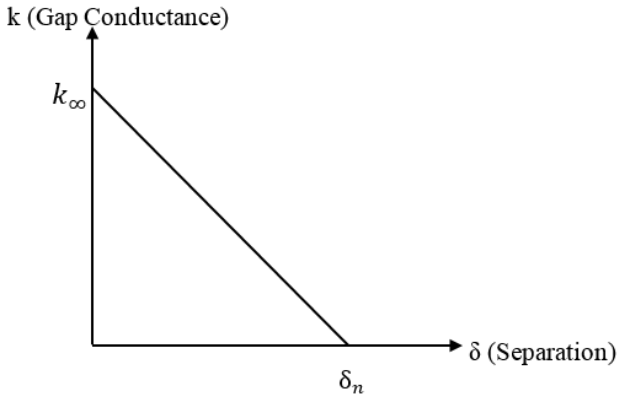


Figure 7.3: Gap Conductance vs. Separation between Two Surfaces in Contact

thermal contact resistance is assumed to negligible and complete heat transfer conditions across the contact surfaces modelled by defining significantly high thermal contact conductance coefficient at the beginning of analysis at which the contact surfaces are fully bonded. The combination of surface-based cohesive behaviour and thermal conductance behaviour has been used in some studies of thermo-mechanical damage modelling composites by different authours (e.g. [134, 154]) but not in this field to the best of our knowledge.

### 7.2.3. Material Properties

The behaviour and failure mechanism of the cement sheath was modelled by using Concrete Damage Plasticity (CDP) model and calibrated according to numerical-experimental studies performed on cement class G by [116, 147]. Elastic mechanical properties of the steel casing and different rock formations are defined as shown in Table 7.2 after [5].

*Table 7.2: Mechanical Properties of Casing and Rock Formation [5]*

| Materials | Thermal Conductivity $(^{W}/_{m.K})$ | Specific Heat $(^{J}/_{kg.K})$ | Thermal Expansion Coefficient $(^{\mu}/_{o_C})$ | Density $(^{kg}/_{m^3})$ | Young's Modulus $(GPa)$ | Poisson's Ratio |
|---|---|---|---|---|---|---|
| **Casing** | 54 | 470 | 12 | 7850 | 200 | 0.3 |
| **Formation** | | | | | | |
| Wellbore-1 | 4.5 | 1000 | 10 | 3000 | 20 | 0.29 |
| Wellbore-2 | 3.0 | 1500 | 13 | 2300 | 5.5 | 0.3 |

#### 7.2.3.1. Cement Constitutive Modelling

The observed non-linearity in obtained stress-strain curve studying cement mechanical behaviour under compression tests [10, 55] results from two different microstructural changes which happen in the materials while subjected to different loading conditions. One is plastic flow causes the permanent deformation and the second is the development of microcracks which leads to elastic stiffness degradation [56]. Therefore, it is necessary to apply a model which combines plasticity and damage mechanics. The creation of microcracks which is also characterized as softening behaviour of the materials is difficult to explain using classical plasticity models [31]. The damage mechanism is described by two physical aspects corresponding to the two modes of cracking (hardening and softening) [56].

Therefore, in this study, Concrete Damage Plasticity (CDP) model developed by [54] and then modified by [55, 115] has been employed. The Concrete damage plasticity (CDP) model is a continuum model based on damage mechanics and plasticity theory which can be used in improving the prediction of cement class G the behaviour, from initial yield to failure. In the modified revision, two damage variables one for compressive damage and one for tensile damage were incorporated to consider different states of damage. This feature makes the model capable of describing the induced anisotropy of microcracking which also facilitates the numerical implementation procedures [55, 115]. The pressure-sensitive yield criterion accompanied by employing the dilatancy (non-associated flow rule), makes this model more suitable than the others that have been employed in the assessments of cement sheath integrity.

The uniaxial tension response is characterised by a linear elastic relationship until reaching the failure stress ($\sigma_t$) which corresponds to the beginning of micro-cracking in the material. Beyond the failure stress, the effects of micro-cracking are taken into account in the model using a softening stress-strain response. The uniaxial compression response is also characterised by a linear elastic relationship until reaching the initial compressive strength ($\sigma_c$) followed by stress hardening in the plastic region up to the ultimate stress ($\sigma_{cu}$). Strain softening occurs subsequent to reaching the ultimate stress.

The stress-strain relations under uniaxial tension and compression in the CDP model are defined as follows respectively.

$$\sigma_t = (1 - d_t)E_0\left(\varepsilon_t - \tilde{\varepsilon}_{pl}^{t}\right) \tag{7.13}$$

$$\sigma_c = (1 - d_c)E_0\left(\varepsilon_c - \tilde{\varepsilon}_{pl}^{c}\right) \tag{7.14}$$

where $d_t$ and $d_c$ are tensile and compression damage variables; $E_0$ is initial undamaged stiffness; $\tilde{\varepsilon}_{pl}^{t}$ , $\tilde{\varepsilon}_{pl}^{c}$ are tensile and compressive equivalent plastic strains respectively.

In this study, the compression damage $d_c$ was computed using Equation (7.15) [4] as shown in Figure 7.4:

$$d_c = 1 - \frac{\sigma_c'}{\sigma_{cu}} \tag{7.15}$$

where $\sigma_c'$ is the axial stress of the cement on the descending branch, and $\sigma_{cu}$ is the peak point of the stress-strain curve.

Tensile damage $d_t$ was defined using a linear relationship [131] between cement tensile strength and cracking displacement as shown in Figure 7.5.

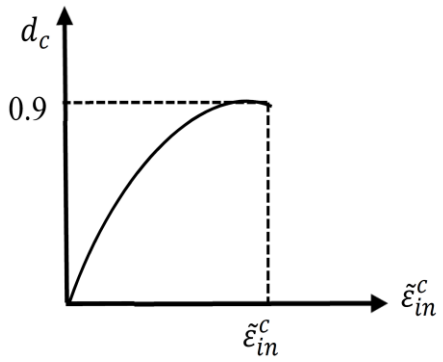


Figure 7.4: Compression Damage vs. Inelastic Strain

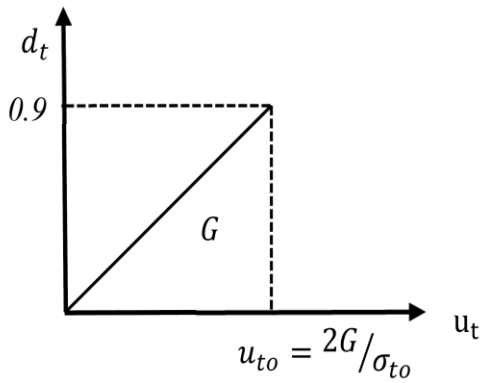


Figure 7.5: Tensile Damage vs. Cracking Displacement

The shape of yield surface in the deviatoric plane changes according to the ratio of the second stress invariant on the tensile meridian to the compressive meridian which allows capturing the material behaviour very well. This yield function was defined by Lubliner, Oliver, Oller and Onate [54] with some modifications made by Lee and Fenves [55], Lee and Fenves [115] afterwards to interpret the evolution of strength under tension and compression. It is defined as follows.

$$F = \frac{1}{1-\alpha}\left(\bar{q} - 3.\alpha.\bar{p} + \beta\left(\tilde{\varepsilon}_{pl}\right)\langle\bar{\sigma}_{max}\rangle - \gamma\langle-\bar{\sigma}_{max}\rangle\right) - \bar{\sigma}_c\left(\tilde{\varepsilon}_{pl}^{c}\right) = 0 \tag{7.16}$$

where $\langle \quad \rangle$ is the Macaulay bracket, $\bar{\sigma}_{max}$ is the maximum principle effective stress, $\bar{p} = -\frac{1}{3}\bar{\sigma}.I$ is the effective hydrostatic stress and $\bar{q} = \sqrt{\frac{3}{2}\bar{S}.\bar{S}}$ is the Mises equivalent effective stress with $\bar{S} = \bar{p}I + \bar{\sigma}$ being the deviatoric part of the effective stress tensor. The function $\beta\left(\tilde{\varepsilon}_{pl}\right)$ in (7.8) is defined as follows.

$$\beta\left(\tilde{\varepsilon}_{pl}\right) = \frac{\bar{\sigma}_c\left(\tilde{\varepsilon}_{pl}^{c}\right)}{\bar{\sigma}_t\left(\tilde{\varepsilon}_{pl}^{t}\right)}(1-\alpha) - (1+\alpha) \tag{7.17}$$

in which two cohesion stresses are employed for the modelling of cyclic behaviour.

$$\alpha = \frac{\left(\frac{\sigma_{bo}}{\sigma_c}\right) - 1}{2\left(\frac{\sigma_{bo}}{\sigma_c}\right) - 1} \tag{7.18}$$

where $\frac{\sigma_{bo}}{\sigma_c}$ is the ratio of biaxial compressive yield stress to uniaxial compressive yield stress. The shape of loading surface in the deviatoric plane is controlled by parameter $\gamma$ in Equation (7.11) [123] and define as

$$\gamma = \frac{3(1 - K_c)}{2K_c + 3} \tag{7.19}$$

where $K_c = \frac{(\sqrt{J_2})_{TM}}{(\sqrt{J_2})_{CM}}$ is a coefficient determined at a given state $\bar{p}$ , $J_2$ is the second invariant of stress with the subscripts TM and CM employed for the tensile and compressive meridians respectively and must satisfy the condition $0.5 \leq K_c \leq 1$ . For the non-associated flow rule, the plastic potential $G$ in the form of the Drucker-Prager hyperbolic function is used.

$$G = \sqrt{(\epsilon \sigma_{to} \tan\psi)^2 + \bar{q}^2} - \bar{p}.\tan\psi \tag{7.20}$$

In which $\sigma_{to}$ is the uniaxial tensile stress at failure, the dilation angle ψ is measured in a p-q plane at high confining pressure, and $\epsilon$ is an indicator for the eccentricity of the plastic potential surface.

***Determination of Cement Constitutive Model Parameters***

The selection of an appropriate constitutive law for the cement sheath as a geo-material and its corresponding model parameters are the utmost of importance part of wellbore integrity modelling. The constitutive parameters were determined through performing experiments and the interpretation of experimental results to obtain the failure envelope of the constitutive model (Concrete Damage Plasticity Model). The experimental outcomes of uniaxial, triaxial compression tests and three-point bending tests performed by Arjomand, Bennett and Nguyen [116] (also completely explained in Chapter 6) on cement class G specimens were utilised in this study. The experimental set-up and procedures were briefly described in the following section.

The cylindrical and prismatic specimens were cured in a water tank with an automatic thermostat was set on 30°C for 28 days. Prior to performing compression tests the surface of the cylindrical samples was ground to achieve smooth surfaces in the way that the ends were completely orthogonal to the cylinder's longitudinal axis [100]. For this purpose, the sample moulds were designed 3 mm taller than the desired sample length. The uniaxial compression tests were run with the displacement rate of to 0.04 mm/min, at which rate the specimens showed less brittle behaviour. Triaxial compression tests were performed with confining pressures ($P_c$) of 15 MPa and 30 MPa. The loading path was designed so that the pressure confinement reached the desired confining pressure at the first step and then were loaded axially under displacement control

until failure occurred. Three-point bending tests on notched and un-notched beam samples were performed to obtain the cement class G tensile strength and fracture energy accompanied by applying modifications on three-point bending set-up. The approximate shape of the yield surface for concrete damage plasticity models and the corresponding constitutive parameters were obtained through parameters calibration as described in [147] and chapter 6 of this thesis.

The cement sheath thermal properties were taken from the study performed by Asamoto, Le Guen, Poupard and Capra [5]. Table 7.3 summarises the cement mechanical and thermal properties utilised in this study.

*Table 7.3: Cement Thermal [5] and Mechanical Properties [147]*

| **Cement Thermal Properties** | | | | |
|---|---|---|---|---|
| **Thermal Conductivity** $\left(W/_{m.K}\right)$ | **Specific Heat** $\left(J/_{kg.K}\right)$ | **Thermal Expansion Coefficient** $\left(\mu/_{^oC}\right)$ | | |
| 1.2 | 2100 | 9 | | |
| **Cement Mechanical Properties** | | | | |
| **Young's modulus** $E_0$ **(GPa)** | **Poisson's ratio (υ)** | **Density** $\left(kg/_{m^3}\right)$ | **Dilation angle** $\psi$ **(degrees)** | **Eccentricity** $\varepsilon$ |
| 6.8 | 0.25 | 1900 | 42 | 0.1 |
| $\frac{\sigma_{bo}}{\sigma_c}$ | $K_c$ | **Initial compressive stress** $\sigma_c$ **(MPa)** | **Ultimate compressive stress** $\sigma_{cu}$ **(MPa)** | **Tensile stress** $\sigma_t$ **(MPa)** |
| 1.16 | 0.8 | 50 | 55 | 1.92 |

## 7.3.Influence of Enhanced Pressure and Temperature on Wellbore-1

The data pertaining to different wellbores geometries, casing and formation material properties are extracted from a case study on the Ketzin site by [5, 53, 148]. A wellbore diameter is a few tens of centimetres whereas the wellbores depth can reach 5000 m, consequently, modelling a wellbore in field scale consisting of surrounding formations requires a very long computational time and excessive finite elements [5]. Therefore, in this study cross-sectional cuts with the height of five inches (0.127 meter) and half of the model due to the symmetric aspect were considered for modelling purposes.

The shallower wellbore (wellbore-1) consists of two layers of casing and cement sheaths located at a shallow depth of 600 m surrounded by caprock. Wellbore-1 was encased by two layers of conductor and surface casings with the diameter of $5\frac{1}{2}^{"}$ and $9\frac{5}{8}^{"}$ and thicknesses of 9.2 mm and 8.9 mm, respectively. To perform more realistic simulations, stress-related factors which induce

wellbore failure in some fields were incorporated within the frameworks including employing anisotropic in-situ stresses as stated in section 7.2.1, and 50% eccentricity applied to the layers of the cement sheath.

Figure 7.6 shows different geometries considered for wellbore-1. The effect of model size including the surrounding formation is important to prevent any artificial effects in the stress distributions and to assure that far-field stresses are applied from a reasonable distance from the wellbores [155]. Salehi [114] suggested that the model size is better to be at least four times bigger

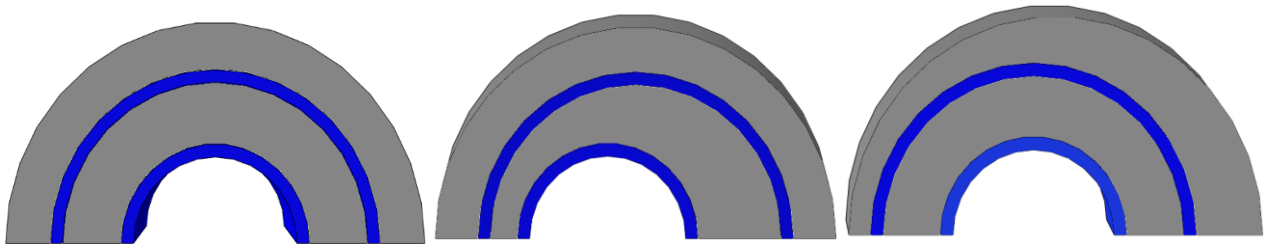

Figure 7.6: Wellbore-1 with Three Different Geometries (Concentric and Eccentric)

than the borehole size. Furthermore, the element size within the section near the wellbore should be smaller than the rest of the formation. This finer section should be at least 2-3 times bigger than the borehole size to improve accuracy [114]. Therefore, the formation rock was partitioned into two sections and meshed with finer mesh near the wellbore area and coarser mesh in the far field area.

The degree of eccentricity (ε) can be computed according to Equation (7.21) [156].

$$\varepsilon\ \% = \frac{\delta}{(R_w - r_c)} \times 100 \tag{7.21}$$

where δ is the distance between the casing centre from the wellbore centre, $R_w$ is the wellbore radius, and $r_c$ is the casing radius. The degree of eccentricity varies from 0 which is completely centralised casing to 100% which means the outer wall of the casing touches the inner of the cement sheath and cement sheath thickness is zero at one side [157].

Wellbore-1 is subjected to $CO_2$ injection conditions imposed to the inner surface of conductor casing while the injection pressure is 7.5 MPa and the maximum $CO_2$ temperature is set to 310.15 K. The initial temperature ($T_0$) is assumed to be constant for the entire wellbore and surrounding formation with the initial temperature of 305.15 K [53]. Anisotropic in-situ stresses were applied to the model (section 7.2.1) using some of the magnitudes taken from geological information study on the Ketzin site [148].

The effect of three different geometries was investigated including concentric and eccentric with 50% eccentricity embedded into the first and second layer of the cement sheath as shown in Figure 7.6. The local compression and tensile damage contour are illustrated in Figure 7.7.

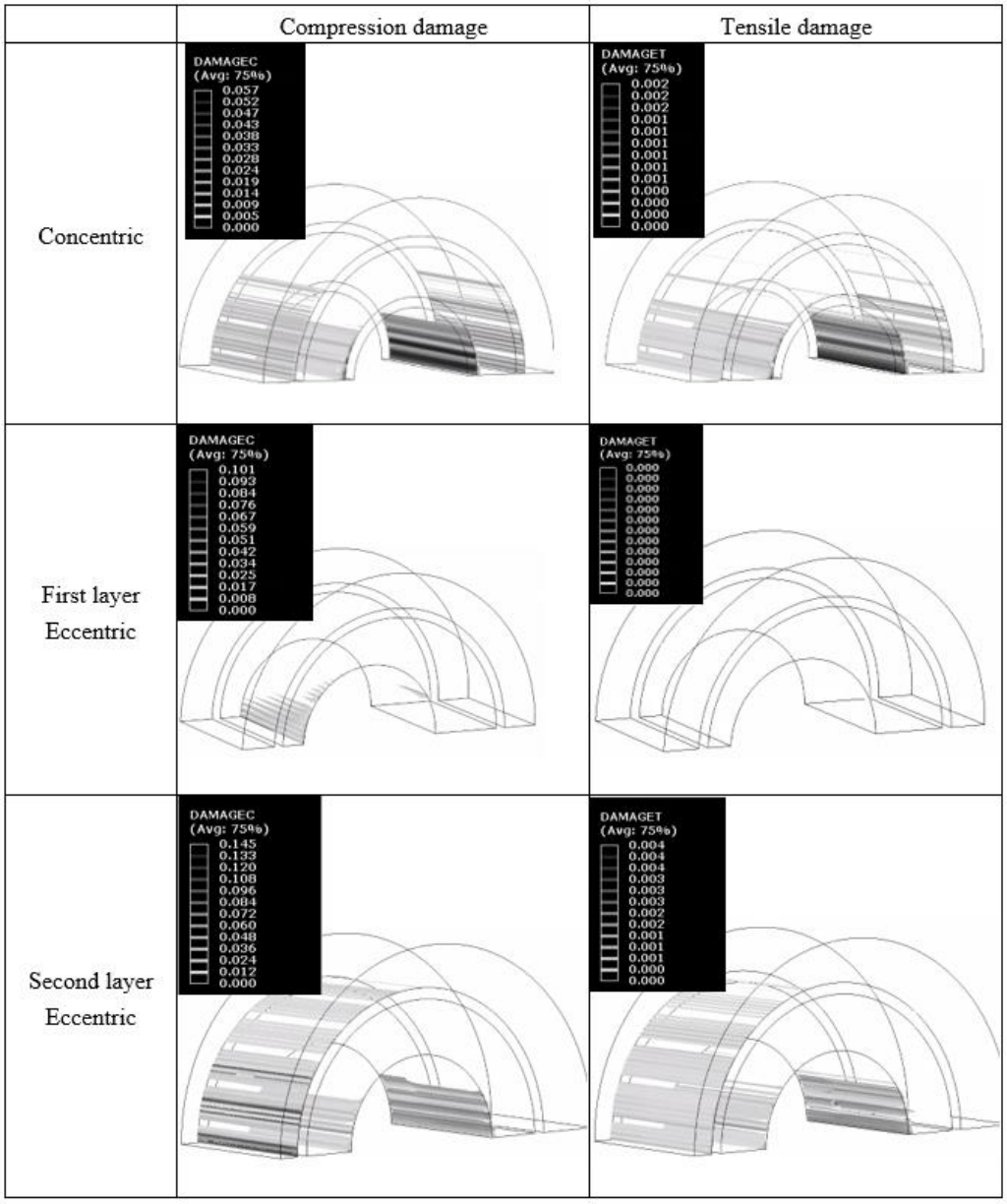


Figure 7.7: Local Compression and Tensile Damage Contours within the Cement Sheaths

As can be seen in Figure 7.7, the magnitudes of local compression damage and tensile damage are negligible. The highest magnitude of compression damage and tensile damaged occurred with the outer layer of cement sheath with 50% eccentricity in wellbore-1. It is worth noting that the magnitude of applied pressure was very low compared to the in-situ stress confinement magnitudes and the temperature variations were only five degrees which leads to minimal

compression and tensile damage. The obtained results are in good agreement with the other studies carried out on this case-study, for instance, Asamoto, Le Guen, Poupard and Capra [5]. However, wellbore-1 was placed in a critical location due to its vicinity to the underground water. Therefore, the injection of higher pressure and temperature variations in this location should be executed with caution.

## 7.4.Influence of Heating Scenarios Operated along with Pressure on Wellbore-2

The deeper wellbore (wellbore-2) consists of single intermediate $7^{"}$steel casing thickness of 9 mm and one layer of cement sheath surrounded by unconsolidated sandstone formation located at a depth of 1000 m. Three different degrees of eccentricity of 30%, 50% and 70% were assessed for wellbore-2 as shown in Figure 7.8.

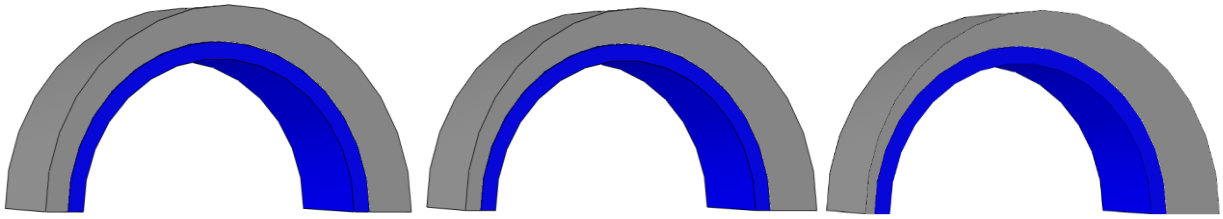

Figure 7.8: Wellbore-2 with Three Different Degrees of Eccentricity (30%, 50%, and 70%)

The contribution of thermal loading scenarios along with different heating rates on cement sheath stress state, plastic deformations, and debonding within the cement sheath corresponding to the different mechanical-thermal scenarios and three different degrees of eccentricity were analysed. The materials' mechanical-thermal properties, the magnitude and arrangements of anisotropic in-situ stresses are maintained constant for all the following analyses.

Wellbore-2 is subjected to 18 MPa pressure at the inner wall of the casing along with temperature variations. The initial temperature ($T_0$) is assumed to be constant for all the model components as $303.15$ K. Temperature variations of $\Delta T = (T_1 - T_0) = (573.15\ \text{K} - 303.15\ \text{K})$ considering three different heating rates were applied at the inner wall of the casing.

### 7.4.1. Compression Damage Considering Heating Scenarios

The potential crushing ($d_c$) occurrence caused by pressuring the wellbore, temperature changes and employment of anisotropic in-situ stresses within the cement sheaths are examined through the local compression damage contours and a global compression damage indicator in the following sections. Figure 7.9 illustrates the local compression damage contours within the cement sheaths subjected to pressure and temperature changes with three different heating rates of instant

heating, and controlled heating rates of $\frac{1.2^{o}C}{min}$ and $\frac{0.5^{o}C}{min}$. All the damage contours were scaled from zero to one for comparison purposes.

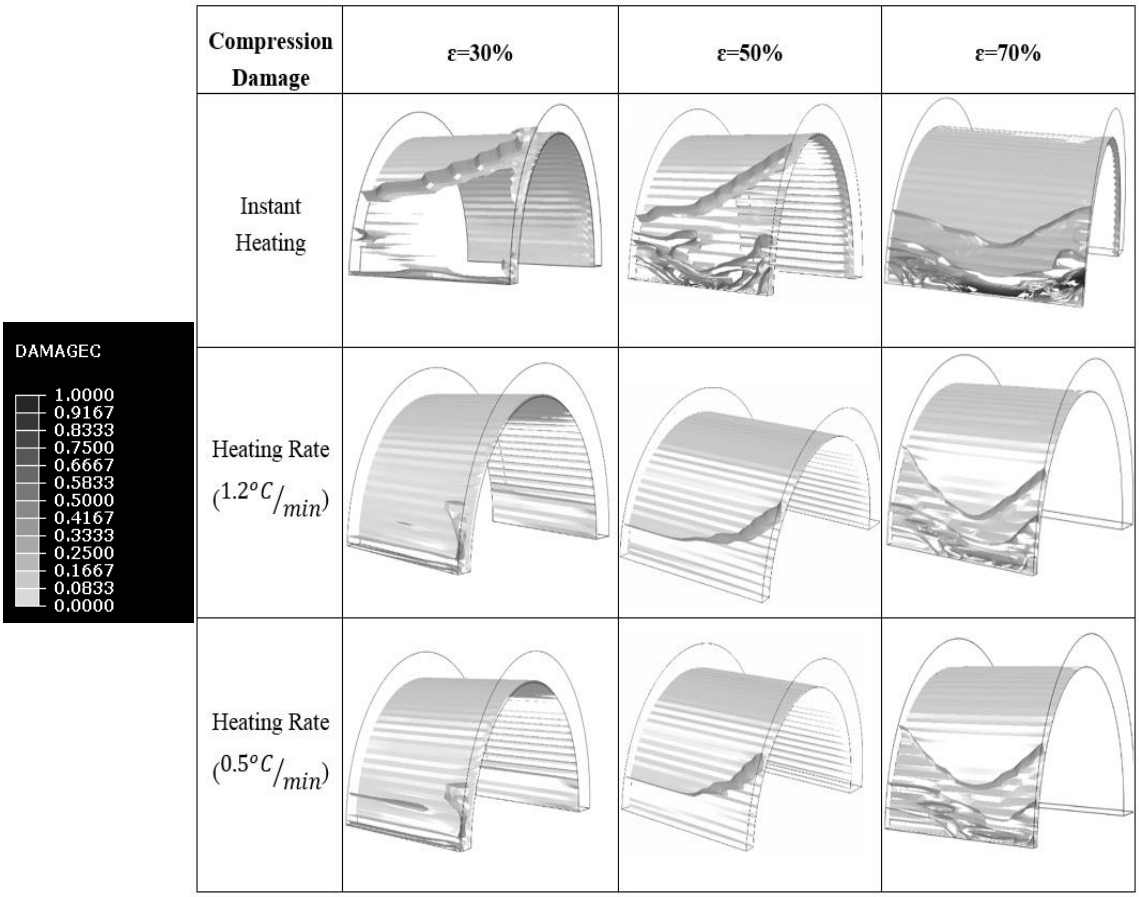


Figure 7.9: Local Compression Damage Contours within the Cement Sheaths Subjected to Pressure during Heating Scenarios

The additional shear stress caused by the anisotropy of in-situ stresses and casing expansion due to the imposed thermal loads resulted in the creation of radial cracks within the cement sheaths as can be seen in Figure 7.9. The compression damage within the wellbores is more distributed in wellbores with 30% and 50% eccentricity. While for the wellbore with 70% eccentricity the compression damage is highly concentrated in the narrower parts. The local maximum compression damage occurred in the narrower part of cement sheath for all the cases regardless of mechanical and thermal loading scenarios which shows the dominant effect of eccentricity on the stress distribution within the cement sheaths. The highest magnitude of local compression damage ($d_c$ =0.95) occurred within the cement sheath with 70% eccentricity subjected to instant heating. Whereas, this magnitude reduces to 0.47 in wellbores subjected to controlled heating rates for the same degree of the eccentricity. This pattern repeated for the wellbores with 50% and 30%

eccentricity (the maximum local compression damage occurred within the wellbores subjected to instant heating). The considerable difference in maximum compression damage magnitude is indicative of the destructive impact of instant heating on causing crushing damage within the cement sheaths.

Figure 7.10 shows the temperature gradients within the casing and the 70% eccentric cement sheath after subjected to different heating rates. As can be seen in Figure 7.10, by the end of the simulation time, the temperature was consistent throughout the entire casing while the cement sheath experienced a temperature gradient across the whole section. A significant thermal gradient was also noticeable from the narrow side towards the wide section.

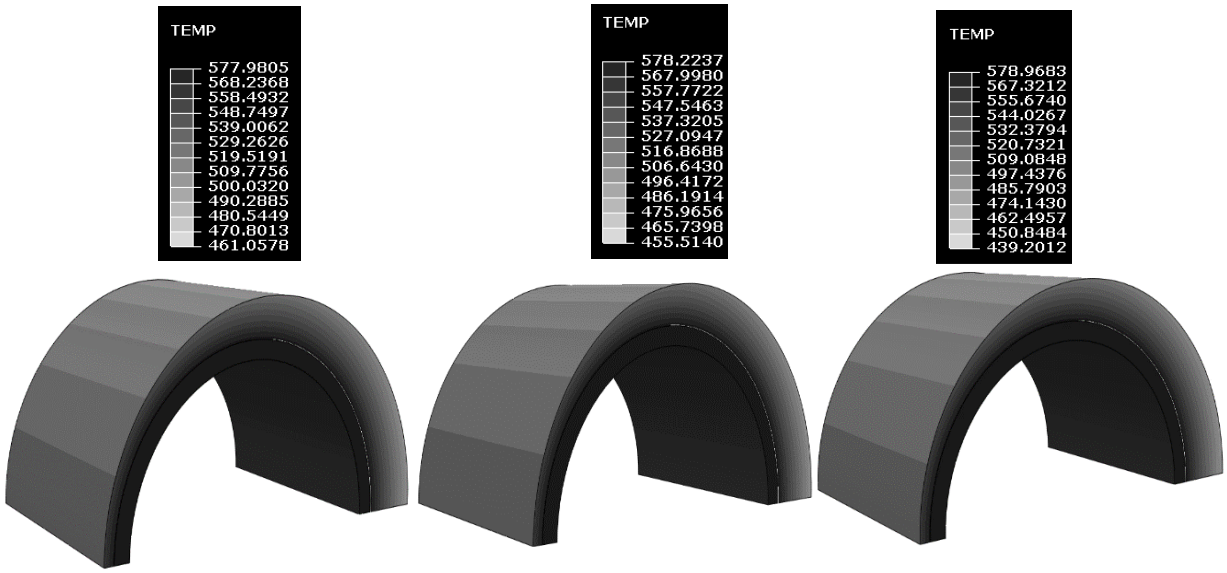


Figure 7.10: Temperature Gradient across the Casing and 70% Eccentric Cement Sheath in Instant, Fast, and Slow Heating Rate Scenarios Respectively

The highest compression damage occurred in the instant heating scenarios for the cement sheath with 70% eccentricity is also be attributed to the highest thermal flux magnitude detected at the cement sheath interface with the casing and the formation (Figure 7.11) subjected to the instant heating scenario.

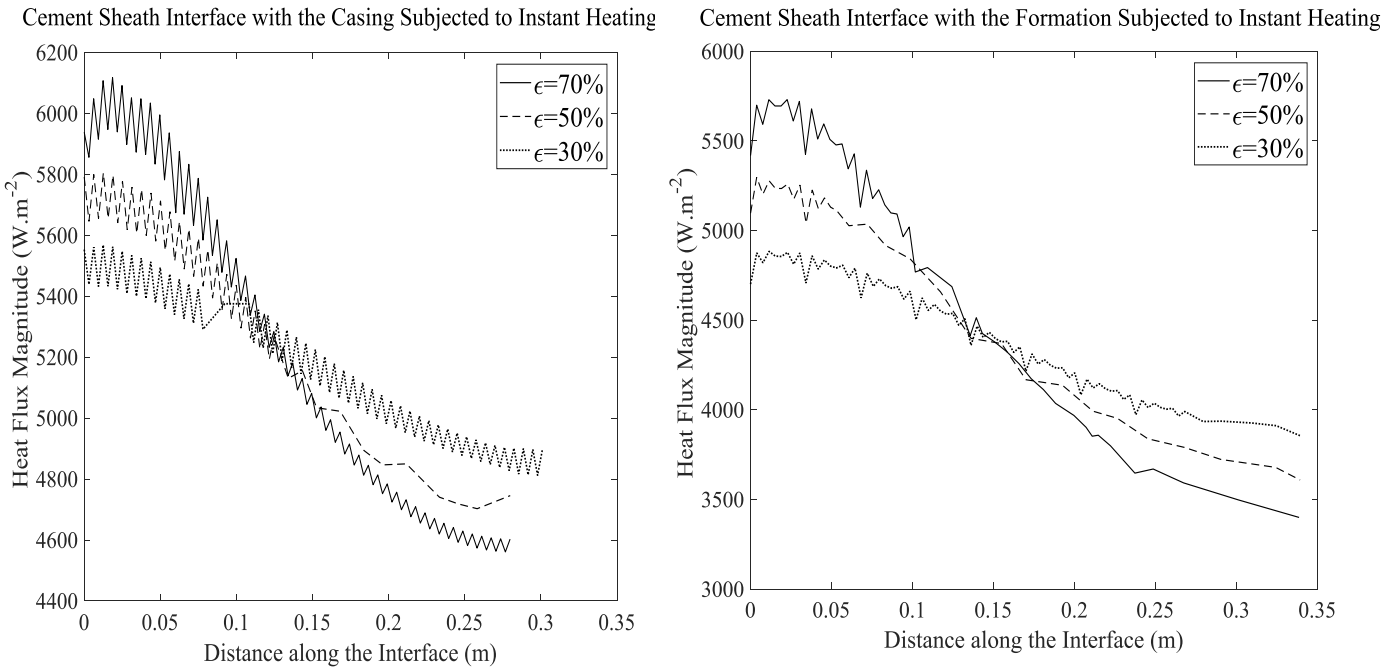


Figure 7.11: Heat Flux Magnitude at the Interface of the Cement Sheaths with the Casing and the Formation Subjected Instant Heating Scenarios

The narrower sides of the cement sheath with 70% and 50% eccentricity are also experiencing some disking cracks as a result of steel casing expansion and highly unbalanced stress distribution in these cases. The thermal expansion coefficient and thermal conductivity of are both higher for the steel compared to the cement thermal properties which resulted in uneven thermal strains of the steel casing and the cement sheath led to the creation of disking cracks in this section.

In order to have a more general indicator to compare all the different scenarios, we defined a global compression damage indicator ($D_c$) as follows.

$$D_c = \sum_0^N \left(\frac{d_c}{N}\right) \tag{7.22}$$

where $d_c$ is the local compression damage magnitudes for all the nodes within the cement sheath, and N is the number of nodes with associated compression damage, i.e. excluding nodes where the damage is zero.

Figure 7.12 shows the global compression indicator values versus the degree of eccentricity for heating scenarios.

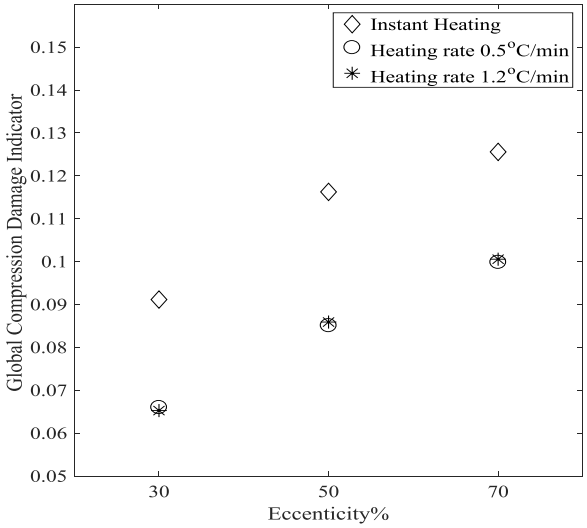


Figure 7.12: Global Compression Damage Indicator vs. Eccentricity for Different Heating Scenarios under High Temperature Changes

The critical effect of eccentricity and application of controlled heating rates on the integrity of cement sheaths again can be confirmed by considering the compression damage contour in Figure 7.9, and the global compression damage indicator in Figure 7.12. The global compression damage indicator reaches the highest value in the case of cement sheath with 70% eccentricity subjected to instant heating. The magnitude of global compression damage indicator is higher for all the cement sheaths subjected to instant heating. The magnitude of global compression damage in cases subjected to controlled heating rates is similar which is indicative of the benefit of finding a reasonable heating rate to reduce the cement sheath damage.

### 7.4.2. Tensile Damage Considering Heating Scenarios

The tensile cracking susceptibility is investigated using the tensile damage contours and a global tensile damage indicator. The state of local tensile damage (cracking) contours within the cement sheath after mechanical-thermal loading is shown in Figure 7.13. All the damage contours were scaled from zero to one for comparison purposes. As can be seen in Figure 7.13, the tensile damage is more localised in comparison with compression damage as shown in Figure 7.9. Considering the localisation of tensile damage contours demonstrates the important role of eccentricity in the distribution of tensile stress within the cement sheath again as the tensile damage occurred only the narrower side of the cement sheaths.

The maximum local tensile damage ($d_t$=0.774) occurred at the narrowest side of the cement sheath with 70% eccentricity subjected to instant heating. The maximum local tensile damage magnitude decreases to 0.39 and 0.28 for the cases subjected to the controlled heating rates of $\frac{1.2^oC}{min}$ and $\frac{0.5^oC}{min}$ respectively. The high thermal strains occurred at the interface of the cement sheath with the formation in the narrower sides make this section more vulnerable towards the tensile cracks.

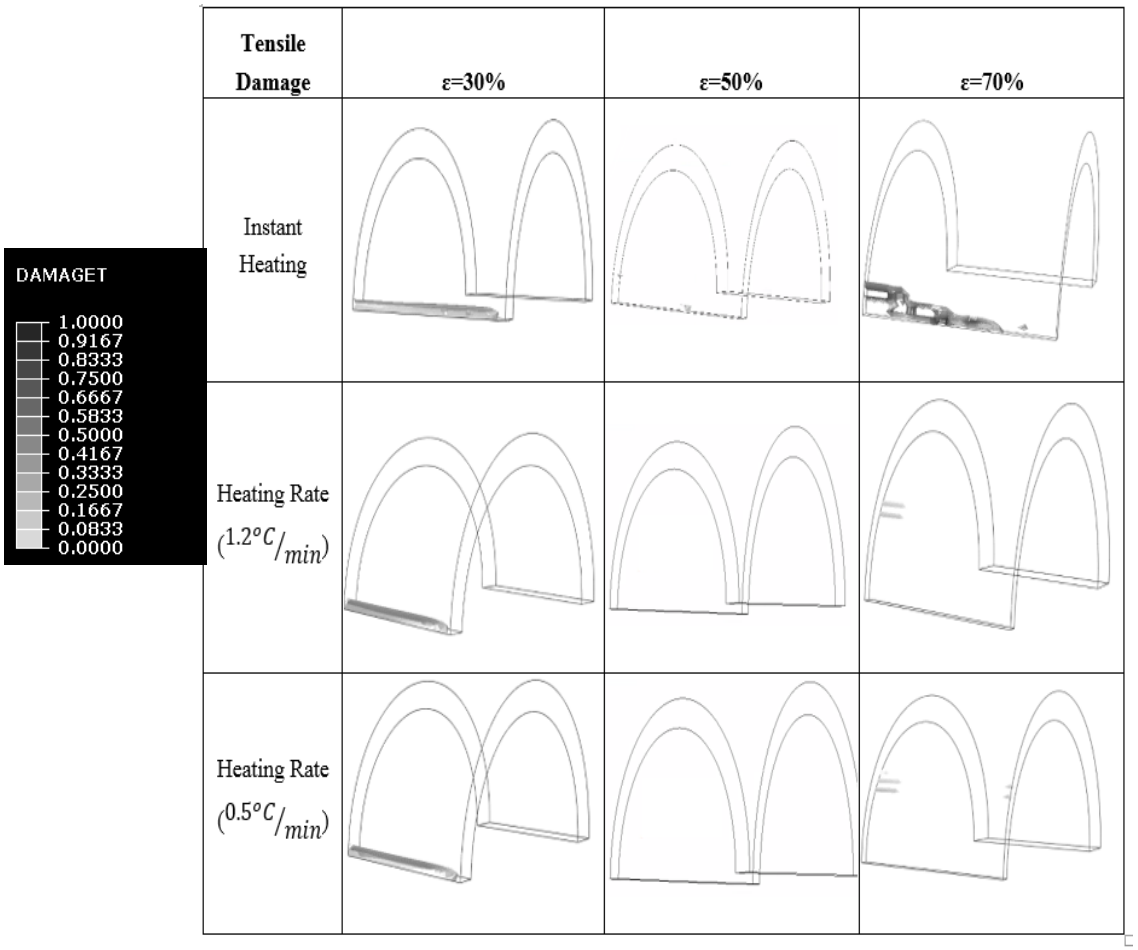


Figure 7.13: Local Tensile Damage Contours within the Cement Sheath Subjected to Pressure during Heating

To compare all the zones within the cement sheath experiencing tensile cracking, a global tensile damage indicator ($D_t$) was computed as follows.

$$D_t = \sum_0^N \left(\frac{d_t}{N}\right) \tag{7.23}$$

where $d_t$ is the local tensile damage magnitude for all the nodes within the cement sheath, and N is the number of nodes with associated tensile damage.

Figure 7.14 demonstrates the magnitude of global tensile damage indicators within the cement sheath subjected to heating scenarios.

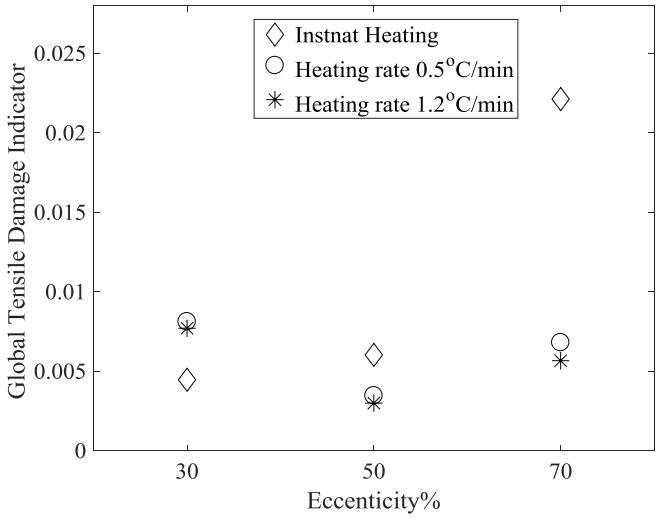


Figure 7.14: Global Tensile Damage Indicator vs. Eccentricity during Heating Scenarios

As can be seen in Figure 7.14 the magnitude of global tensile damage reaches the highest value in the case with 70% eccentricity subjected to the instant heating which emphasises the conservative aspect of monotonic simulations.

The global tensile damage indicators within the cement sheath with 30% eccentricity subjected to controlled heating rates are higher than the instant heating scenario in Figure 7.14. In these scenarios for the 30% eccentric cement sheath with controlled heating rates, the wellbores gradually warm up which allows the heating flux to transmit entirely within the model which leads to the higher temperature gradient and consequently creation of higher thermal strains within the narrower side of the cement sheath. The narrower side of the cement sheath with 30% eccentricity shows more resistance to the casing expansion in comparisons with the cement sheath with 50% and 70% eccentricity due to having the highest thickens among them. The high resistance of the cement sheath with 30% eccentricity leads to high contact shear stresses and subsequently high tensile damage. Theses observation of tensile cracks indicates that the magnitude of local and global tensile damage is more dependent on the wellbore geometry rather than the heating rates.

## 7.5.Influence of Cooling Scenarios along with Pressure Operated on Wellbore-2

Wellbore-2 in the cooling scenarios is subjected to 18 MPa pressure at the inner wall of the casing along with temperature variations with the initial temperature is assumed to be constant for all the model components as 573.15 K. Temperature variations of $\Delta T = 303.15\,K - 573.15\,K$ considering three different cooling rates were applied at the inner wall of the casing.

### 7.5.1. Compression Damage Considering Cooling Scenarios

Figure 7.15 shows the local compression damage contours within the cement sheaths subjected to cooling scenarios. The compressive response of the wellbores is different during cooling in terms of compression damage magnitude, crack type, and localisations to its compressive response

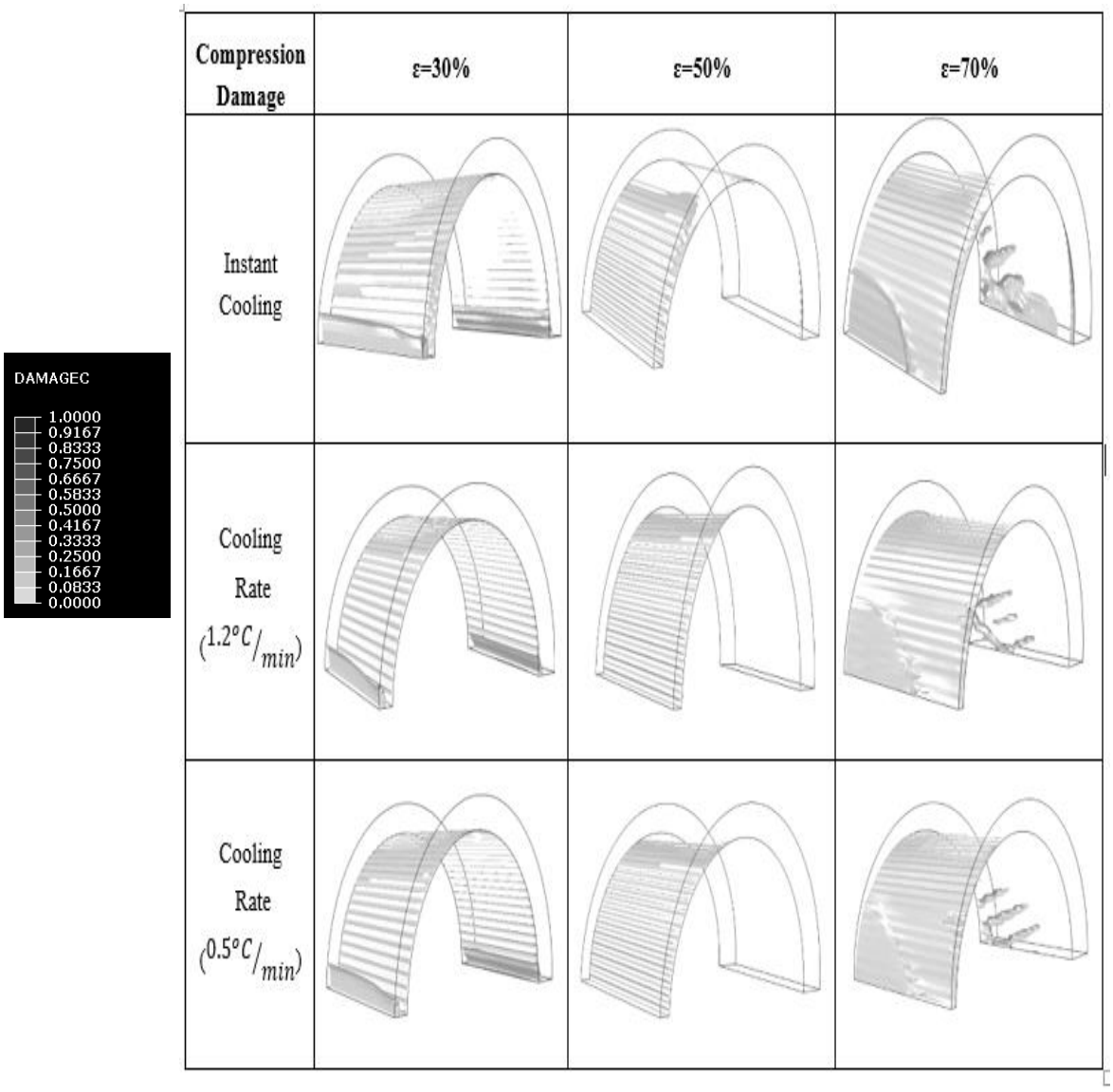


Figure 7.15: Local Compression Damage Contours within the Cement Sheaths Subjected to Pressure during Cooling Scenarios

to heating events. As the contraction of steel casing and subsequently dragging the cement sheath towards the wellbore centre counterbalanced with the applied mechanical pressure at the inner wall of the casings.

In addition, the compression/shear damage was observed at the wider side of the cement sheath with 70% eccentricity while in heating scenarios the heating scenarios compression damage was mainly concentrated at the narrower side of the cement sheath. The maximum local compression damage ($d_c \approx 0.3$) occurred at the narrower side of the cement sheath with 70% eccentricity subjected to controlled heating rates. The process of cooling down happens gradually in the controlled heating rates which allow the wellbore to contract further and leads to higher thermal strains.

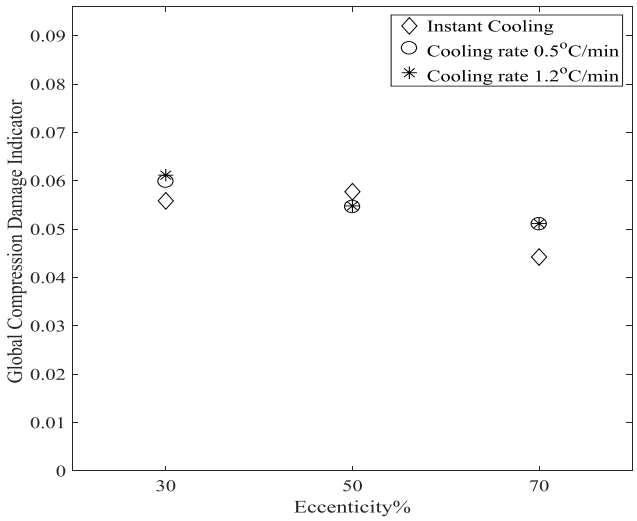

Figure 7.16: Global Compression Damage Indicator during Cooling

Figure 7.16 shows the global compression damage indicator computed according to Equation (7.14). As can be seen in Figure 7.16 the effect of cooling rates on the cement sheath compression damage is minimal due to the dominant effect of pressurizing the wellbore and in-situ stresses confinements within the range studied in this paper. These observations are in a good agreement with the numerical-experimental study performed on the impacts of thermal cycling on wellbore integrity during $CO_2$ injections by Roy, Walsh, Morris, Iyer, Hao, Carroll, Gawel, Todorovic and Torsæter [158].

### 7.5.2. Tensile Damage Considering Cooling Scenarios

The tensile damage occurred in the cooling scenarios was relatively low comparing to the heating scenarios. The maximum local tensile damage occurred at the narrower side of the cement sheath with 70% eccentricity ($d_t$=0.21) subjected to the slowest cooling rate $\left(\frac{0.5^{o}C}{min}\right)$. The low tensile damage magnitudes are attributed to the dominant compressive effect of the mechanical

load and the confinement of in-situ stresses. Figure 7.17 demonstrates the global tensile damage indicator computed according to Equation (7.15) subjected to different cooling rates.

As can be seen in Figure 7.17, the employment of slowest cooling rate led to the highest global tensile damage within the cement sheath with 70% eccentricity. An arbitrary path was defined from the narrowest section towards the widest section to compare the thermal strains with respect

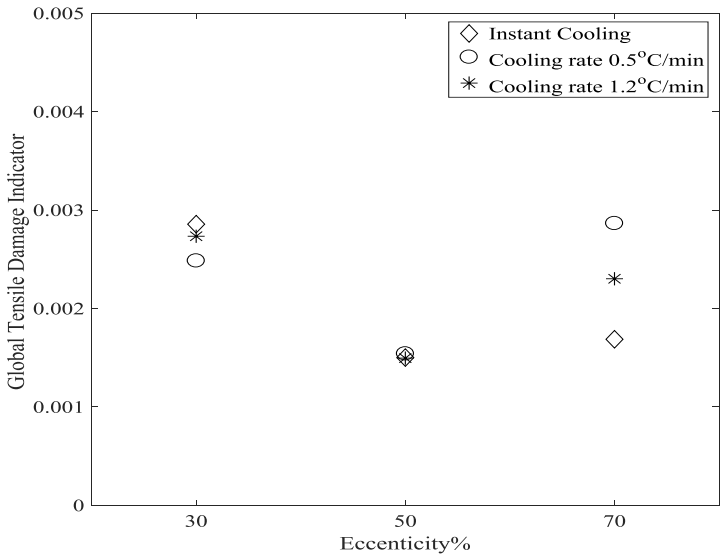


Figure 7.17: Global Tensile Damage Indicator during Cooling

to the three different cooling rates within the cement sheath with 70% eccentricity. Figure 7.18 shows the arbitrary path.

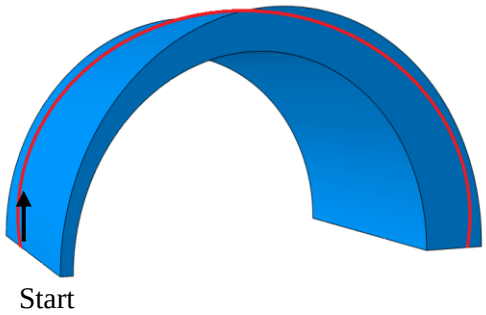


Figure 7.18: Arbitrary Path within the Cement Sheath with 70% Eccentricity

Figure 7.19 shows the corresponding thermal strains for the three different cooling rates. As can be seen in Figure 7.19 the gradient of thermal strain corresponding to the slowest rate is the steepest which resulted in higher global tensile damage among the three rates. As applying thermal loads in this scenario with the slowest rate provides more time for the thermal flux to be transmitted across the wellbore which led to the sharpest gradient of thermal strains.

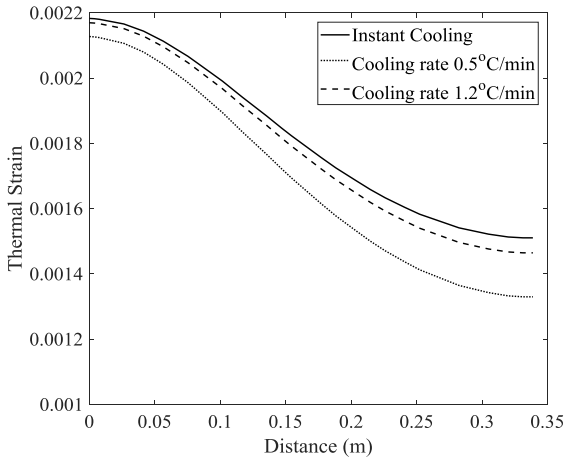


Figure 7.19: Thermal Strain Gradient for the Selected Path Considering Different Cooling Rates

## 7.6. Susceptibility of Forming Micro Annuli

The integrity of the cement sheath bonds in two extreme eccentric cement sheaths studied (30% and 70%) are examined through a contact stiffness degradation index in this section. Two arbitrary paths were selected at the cement sheath interfaces as shown in Figure 7.20 along with the starting locations of the selected paths. Both paths start at the narrowest side and end at the thickest part of the cement sheaths.

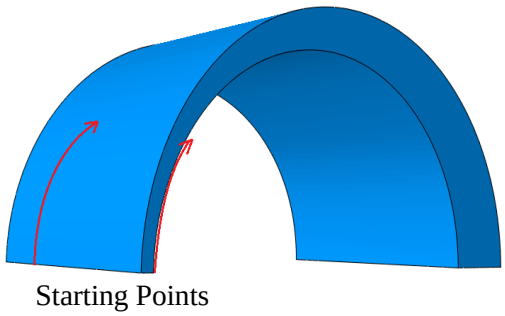


Figure 7.20: Cement Sheath Interfaces with the Casing and Rock Formation

Figure 7.21 demonstrates the degradation of contact stiffness at the cement sheath interface with the casing subjected to heating and cooling scenarios considering the three thermal rates within the cement sheaths with 30% eccentricity.

As can be seen in Figure 7.21(a) the contact stiffness between the casing and the cement sheath is fully degraded when subjected to instant heating which is again an indication of the detrimental effect of instant heating. While for the controlled heating rates scenarios the degradation index reaches one in particular section (almost at the centre of the selected path) of the interface. Figure 7.21 (b) shows debonding at the interfaces is not occurred yet in the cooling scenarios, although at the starting and ending locations of the selected path the degradation index reaches 0.8 (which means 80% of the contact stiffness is degraded).

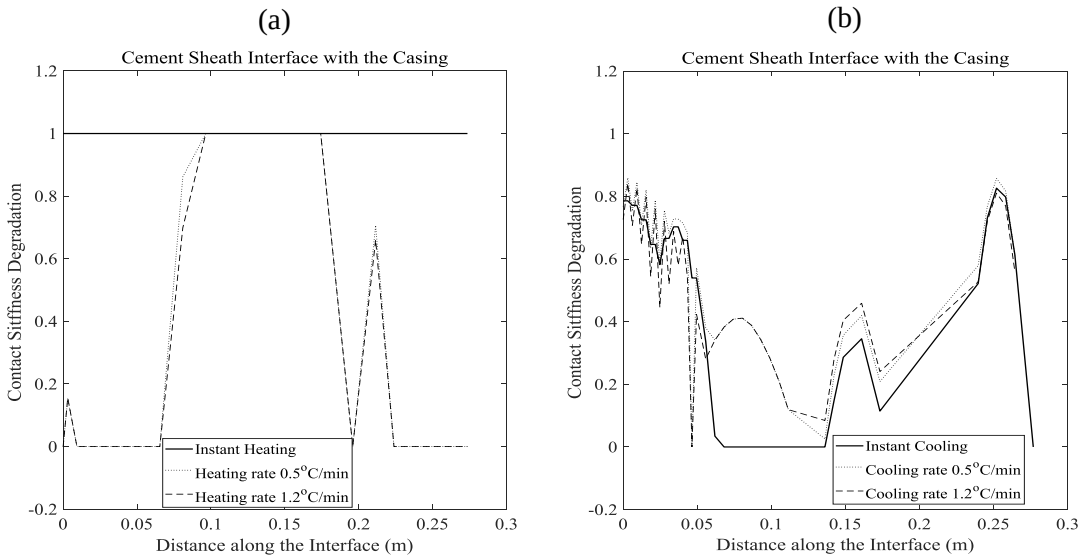


Figure 7.21: Contact Stiffness Degradation at the Interface of the 30% Eccentric Cement Sheaths with the Casing Subjected to Heating and Cooling Scenarios

Figure 7.22 demonstrates the degradation of contact stiffness at the cement sheath interface with the casing subjected to heating and cooling scenarios considering the three thermal rates within the cement sheath with 70% eccentricity.

(a) (b)

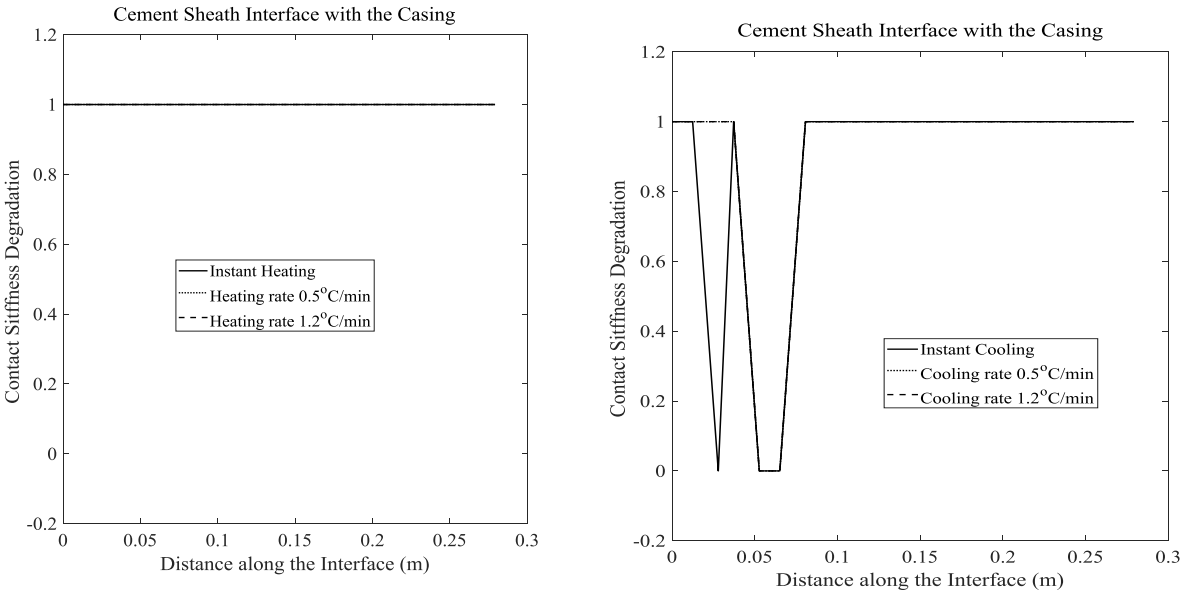


Figure 7.22: Contact Stiffness Degradation at the Interface of the 70% Eccentric Cement Sheaths with the Casing Subjected to Heating and Cooling Scenarios

As can be seen in Figure 7.22 the contact stiffness of the cement sheath with 70% eccentricity is fully degraded in all the scenarios except a very small section of the interface subjected to controlled cooling rates (Figure 7.22(b)). Comparing the Figure 7.21 corresponding to the interface of the cement sheath (with 30% eccentricity) with the casing with the same interface for the cement sheath with 70% eccentricity (Figure 7.22) confirms the destructive effect of a high degree of eccentricity.

Figure 7.23 demonstrates the degradation of contact stiffness at the cement sheath interface with the formation subjected to heating and cooling scenarios considering the three thermal rates within the cement sheaths with 30% eccentricity.

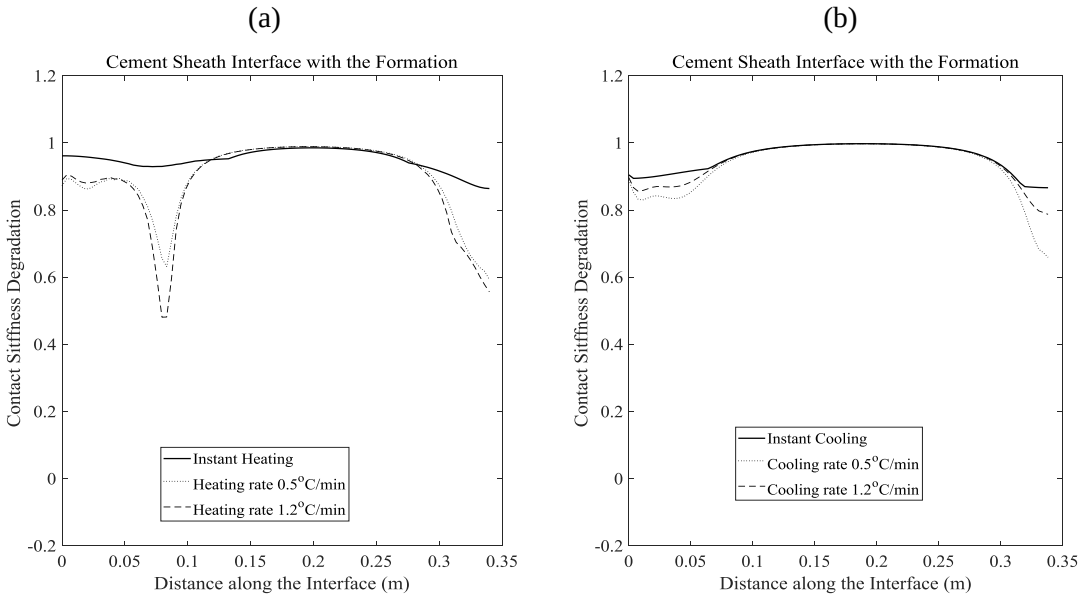


Figure 7.23: Contact Stiffness Degradation at the Interface of the 30% Eccentric Cement with the Formation Subjected to Heating and Cooling Scenarios

Comparing Figure 7.23(a) demonstrates that this interface resists debonding in the scenarios subjected to controlled heating rates while for the instant heating scenario is almost deboned from the formation (the degradation index is 0.95). Figure 7.23(b) shows the cement sheath interface with the formation in the scenarios subjected to cooling thermal loads are almost fully degraded and reaches very close to one for all the scenarios.

Figure 7.24 demonstrates the degradation of contact stiffness at the cement sheath interface with the formation subjected to heating and cooling scenarios considering the three thermal rates within the cement sheaths with 70% eccentricity.

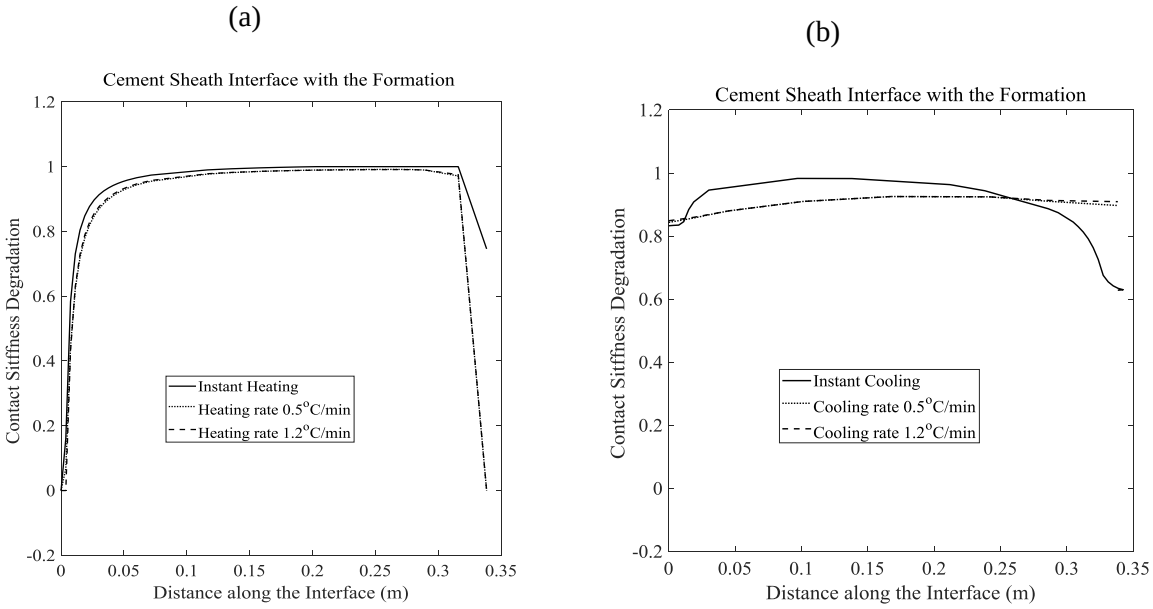


Figure 7.24: Contact Stiffness Degradation at the Interface of the 70% Eccentric Cement with the Formation Subjected to Heating and Cooling Scenarios

Considering the damage index at the interfaces in Figure 7.24 shows the weakness of the interfaces while subjected to mechanical and thermal loads in the cement sheath with 70% eccentricity.

The interfaces are the most vulnerable parts of wells due to the high difference in the stiffness of surrounding materials, and high contact shear stresses in tangential and normal directions of the interfaces. The contact stiffness degradation reaches near to one in all the simulations signifies the high potential of debonding at the interfaces. However, the occurrence of cement sheath debonding from the casing prevents the stress transference from the casing to the cement, therefore, it may prevent the incidence of cement sheath cracking and it may relax the stress regime within the cement sheath. Cement sheath centralisation, remedial cementing and using expandable liners (at the interfaces of cement and casing) may help to alleviate these kinds of problems.

## 7.7.Conclusion

A numerical approach was carried out to investigate the integrity of eccentric cement sheaths after being subjected to mechanical and thermal well operational procedures in relation to the creation of cracks within the cement sheath and the propensity of cement sheath interface debonding. The importance of incorporating a comprehensive constitutive model (Concrete Damage Plasticity model) for modelling geo-materials such as cementitious materials was shown.

The superiority of Concrete Damage plasticity model with respect to simulating different states of damage by considering the different response of geo-materials to tensile and compression stress state and consequently capability to reproduce experimental data were highlighted. This model also considers the materials pressure-dependency behaviour under shearing at different levels of confinement and dilatancy of the geo-materials by incorporating non-associated flow rule.

The integrity of the cement sheath was assessed based on the local compression and tensile damage, and global damage indicators within the cement sheaths considering different mechanical and thermal scenarios. The compression and tensile damage occurred on the narrowest side of the cement sheaths in all the studied scenarios confirm the importance of casing centralisation.

The simulations results show employing controlled heating rates might lead to less potential compression damage within the cement sheaths. The magnitude and localisation of tensile damage are more dependent on the geometry of the wellbore rather than the heating rates.

In cooling scenarios (within the range studied) the magnitude of local and global compression and tensile damage occurred within the cement sheaths are considerably lower than heating scenarios. Moreover, the effects of different rates of cooling on the cement sheath damage are also minimal due to the dominant effect of pressurizing the wellbore and in-situ stresses confinement. The simulations result also show that the cement sheath interfaces with the casing and the formation are potential weak points to provide zonal isolation.

To prevent damage occurring within the cement sheaths requires assessments and simulations considering the specific features of each case. There are many influential factors which make every case different than the others. The effect of cement and the surrounding mechanical and thermal properties, different geometries and architectures of the wellbores, wellbore operational procedures, the anisotropy of geological stress fields, and the complex behaviour of the interfaces etc. are required to be investigated and implemented for each simulation.

# 8. Conclusions

The cement sheath in oil and gas wells acts as the key barrier to provide complete zonal isolation and prevents the undesired fluid migration to the surrounding environment. The cement sheath integrity might be compromised due to the imposed pressure and temperature variations to the wellbores during wellbores lifetime or even after wellbores are abandoned/decommissioned. The cement sheath mechanical failure within a wellbore is influenced and controlled by many factors including but not limited to cement mechanical properties, cement bonding strength, in-situ stresses conditions, cement history (cement shrinkage), wellbore architecture, and wellbore deviation. Due to the complications accompanied by each factor, it is of utmost importance to include all the pertinent features into the predicting models with respect to the cement failure mechanisms within the current state of the art.

To achieve the above goal, this thesis aimed to improve the modelling capabilities in cement sheath integrity evaluations by employing a more comprehensive constitutive model (Concrete Damage Plasticity model) compared to the rest of the models previously used. The superiorities of Concrete Damage Plasticity model have been explained with respect to its abilities to embed different states of damage (compression/shear and tensile), pressure sensitive yield criterion, and the materials dilatancy (utilising non-associative flow rule). However, the paucity of cement class G mechanical properties was an obstacle to perform precise numerical simulations in particular data pertaining to the cement long-term mechanical properties and confinement dependent strength. Therefore, in the experimental phase of this study, the corresponding constitutive model parameters were obtained through performing confined, unconfined compression tests, and indirect tensile tests (three-point bending tests) on specimens made out of cement class G. The suitability and reliability of the intended model parameters were also calibrated and validated by numerical simulations.

The effects of different influential factors including the anisotropy of in-situ stresses, different stiffness's of surrounding rocks, different degrees of casing eccentricity, and different mechanical and thermal loading scenarios (heating rates/cooling rates) were investigated in the numerical simulations. The significance of casing centralisation and elevated risks of cement mechanical failure caused by wellbore operations in anisotropic in-situ stress fields with soft rocks were highlighted. The simulations result also showed that the cement sheath subjected to controlled heating rates might experience less potential compression damage comparing to cement sheath subjected to instant heating. The magnitude and localisation of tensile damage were shown to be more dependent on the geometry of the wellbore rather than the heating rates. In cooling scenarios,

the effects of wellbore contractions due to temperature reduction on the cement sheath integrity were shown to be minimal due to the dominant effect of pressurizing the wellbore and in-situ stresses confinement.

## 8.1.Research Contributions

This thesis improved the capabilities of predictive models for cement sheath integrity assessments and addressed the limitations of the previous models and shortcomings in the cement class G mechanical properties inventory. The specific research contributions to address the research intentions are as follows.

- **Objective 1- Evaluation of Cement Sheath Integrity Subject to Enhanced Pressure (PAPER-1)**

An experimental-numerical approach was developed to evaluate the integrity of the cement sheath after being pressurised regarding the creation of cracks within the cement sheath and the creation of micro-annuli. The key intention of the approach is the incorporation of Concrete Damage Plasticity (CDP) constitutive model for the cement sheath. The CDP model especially formulated for modelling geo-materials by considering the difference in tensile and compressive material responses, the pressure-dependent material behaviour under shearing at different levels of confinement, and the materials dilatancy.

The experimental studies including uniaxial compression tests and three-point bending tests were performed on specimens manufactured from cement class G to obtain the corresponding constitutive model parameters. The results indicate the paramount influence of eccentricity on the distribution of stress within the cement sheath which highlights the significance of casing centralisation. The scenarios simulating pressure enhancement events considering anisotropic in-situ stress fields with soft rocks exhibit the elevated possibility of high global damage indicator in crushing and cracking. The high magnitude of cracking index (tensile damage) verifies the importance of including tensile failure mechanisms into the constitutive modelling. The simulations also show that the material interfaces are potential weak points.

- **Objective 2- Effect of Curing Conditions on the Mechanical Properties of Cement Class G with the Application to Wellbore Integrity (PAPER-2)**

The cement class G inventory lacks some important aspects of cement mechanical properties which cause complications and uncertainties into the performance of numerical simulations. The effect of curing conditions on the responses of cement class G in confined and unconfined compression tests and the measurement of tensile properties including cement fracture energy was

neglected in the inventory. The aim of the experimental phase was to add these important values to the cement class G inventory.

The confined and unconfined compression tests were performed on the on cylindrical specimens with the size of 42×100 mm cured at different temperatures of $30^{o}$C and $70^{o}$C for 28 days. An appropriate loading rate was determined for unconfined (uniaxial) tests as the peak load is shown to be rate dependent on uniaxial tests. The specimens showed a well-defined peak load, followed by highly brittle post-peak behaviour. However, the peak load in confined (triaxial) tests is almost independent of the loading rate in the range measured. Moreover, the maximum strength of the samples increases greatly as the confining pressure increases. The specimens exhibited more ductile behaviour in confined compression tests in which the gradient of the load-displacement graph inclines towards a plateau by the end of the test.

The investigations on curing temperature effects showed by increasing the curing temperatures, the compressive strength of the material decreases considerably. This is attributed to the differences in the formation of calcium silicate hydrate (CSH) gels, due to an increase in the curing temperature.

The highly brittle behaviour of the prismatic samples in three-point bending tests indicated that some modifications were required to be able to measure cement fracture energy properly. To modify the test set-up configuration, the displacement rate was controlled by opening the crack mouth clip gauge instead of the crosshead displacement (which usually controls the displacement rate in three-point bending tests). The axial displacement of the loading platen was measured using two LVDTs installed on both sides of the beam specimens. These applied modifications prevent highly brittle crack propagation and allow capturing the post-peak response and measuring the fracture energy. The results obtained from the clip gauge were also validated by non-contact strain measurement technique using two-dimensional Digital Image Correlation (DIC) technology measurements. In this technique, surface images before and during the deformation are taken by digital cameras. The deformation measurements were based on the displacements of random speckles spread over the surface of the sample. To analyse the images after the test, an area of interest (in the vicinity of the notch) was chosen in which to detect the deformations and strain localizations. The surface displacement was computed by comparing the number of digital images taken during the test with the reference image (undeformed image). The correlation computations were based on tracing a set of pixels sited in deformed images.

The approximate shape of the loading/yield surface for elastoplastic models was obtained utilising the experimental outcomes. The corresponding parameters for Concrete Damage

Plasticity were computed by curve fitting process and were validated by numerical analyses. The obtained parameters improve the accuracy of Concrete Damage Plasticity model implementation for cement sheaths in wellbores integrity simulations.

- **Evaluation of Cement Sheath Integrity Reflecting Thermo-Plastic Behaviour of the Cement in Downhole Conditions (PAPER-3)**

Thermal-mechanical frameworks employing the Concrete Damage Plasticity model using the obtained constitutive parameters (from the performed experiments on cement class G) were developed to investigate the integrity of eccentric cement sheaths after being subjected to mechanical and thermal loads due to different wellbore operational procedures. The interfaces were modelled using surface-based cohesive behaviour accompanied by heat transfer behaviour. The employment of surface-based cohesive behaviour instead of cohesive elements (commonly used) allows the incorporation of thermal conduction behaviour as surface interaction properties to overcome the limitation of the nonexistence of temperature degree of freedom in cohesive elements. The integrity of the cement sheaths was assessed according to the local and global damage indicators for compression and tensile damage within the cement sheaths considering different degrees of eccentricity and different heating/cooling rates.

The results of heating simulations indicated that controlled heating rates might lead to less potential compression damage. While the magnitude and localisation of tensile damage are more dependent on the geometry of the wellbore rather than the heating rates. The results of cooling scenarios (within the range studied) showed the lower magnitude of local and global compression and tensile damage compared to the heating scenarios. In these scenarios, the contraction of wellbore components (caused by temperature reduction) which pulls the wellbore components towards the centre of the wellbore is counterbalanced with the applied pushing pressure at the casing. Moreover, the effects of cooling rates on the cement sheath damage are also minimal due to this dominant effect of pressurizing the wellbore. The low tensile damage magnitudes are attributed to the dominant compressive effect of the applied mechanical load and the confinement of in-situ stresses.

It is worth mentioning that preventing the occurrence of damage within the cement sheaths requires investigation and assessments regarding each case specific characteristics. There are many influential factors which indicate the studies should be done in the case by case basis. The impact of cement and the surrounding mechanical and thermal properties, different geometries and architectures of the wellbores, wellbore operational procedures, the heterogeneity of

geological stress fields, and the complicated response of interfaces, etc. are required to be investigated for each case separately.

## 8.2.Research Limitations

In the numerical phase, uncertainties remain in the cement sheath integrity modelling approaches owing to the complex interactions of the well components at the interfaces; the adherence degree of cement to the surrounding materials is variable and dependent on each site characteristic features including the mechanical characteristics of the rocks (formations), surface finish of the casing, type of mud layer, and degree of mud removal, etc. The data required to generate complex constitutive models (for both materials and the interfaces between them) in addition to the variability of wellbore architectures, cement mix designs, cement curing regimes, and operating conditions (monotonic and / cyclic operational procedures) indicates that the assessment of wellbore integrity resumes a challenge.

## 8.3.Recommendations for future work

The paucity of experimental data that is required for measuring mechanical properties of well cement corresponding to different curing conditions and mixed design still require attention. The experimental phase of this research retains some limitations in terms of simulating the downhole conditions at which cement cures, and the cement slurry formulation regarding lead and tail cement. The curing conditions for cement (pressure and temperature) varies along a well length as depth changes. Therefore, it is better for the cement specimens to be cured under different pressure and temperature to imitate the downhole condition precisely. While in this research the effect of curing temperature alone was examined on the samples made of only cement class G without any additive. The limitations of the current research also represent opportunities for future research, including developing an experimental framework with a special focus on simulating the downhole curing condition along with the associated cement slurry design (lead and tail cement). Moreover, developing regulated protocols to measure cement mechanical properties in particular cement tensile properties is very important.

Developing a comprehensive model to predict cement sheath failure mechanisms in wellbores is still a complicated task. Thus, working in some directions including the poro-plastic behaviour of cement sheath, the effect of porosity, the cement adherence degree to different types of rock formations, and cement mechanical failure under cyclic temperate and pressure variations may lessen the complications in wellbore integrity assessments.

# 9. References

[1] S.S. Rahman, G.V. Chilingarian, Casing Design-Theory and Practice, Elsevier, 1995.

[2] Drilling and casing the wellbore, in: Industri Miga, industrimigas.com/2013/06/drilling-and-casing-wellbore.html, 2013.

[3] L.K. Britt, M.B. Smith, Horizontal well completion, stimulation optimization, and risk mitigation, in: SPE Eastern Regional Meeting, Society of Petroleum Engineers, 2009.

[4] T. Yu, J. Teng, Y. Wong, S. Dong, Finite element modeling of confined concrete-II: Plastic-damage model, Engineering Structures, 32 (2010) 680-691.

[5] S. Asamoto, Y. Le Guen, O. Poupard, B. Capra, Well integrity assessment for CO2 injection: A numerical case study on thermo-mechanical behavior in downhole CO2 environments, Engineering Computations, 30 (2013) 842-853.

[6] B. Weideman, R. Nygaard, How Cement Operations affect your Cement Sheath Short and Long Term Integrity, in: American Assocoation of Drilling Engineers Fluids Technical Conference and Exhibition Houston, Texas, 2014, pp. 15-16.

[7] M.A. Celia, S. Bachu, J.M. Nordbotten, D. Kavetski, S.E. Gasda, Modeling critical leakage pathways in a risk assessment framework: representation of abandoned wells, in: Fourth Annual Conference on Carbon Capture and Sequestration DOE/NETL, 2005.

[8] A.-P. Bois, A. Garnier, G. Galdiolo, J.-B. Laudet, Use of a mechanistic model to forecast cement-sheath integrity, SPE Drilling & Completion, 27 (2010) 303-314.

[9] R.J. Davies, S. Almond, R.S. Ward, R.B. Jackson, C. Adams, F. Worrall, L.G. Herringshaw, J.G. Gluyas, M.A. Whitehead, Oil and gas wells and their integrity: Implications for shale and unconventional resource exploitation, Marine and Petroleum Geology, 56 (2014) 239-254.

[10] W. Crow, J.W. Carey, S. Gasda, D.B. Williams, M. Celia, Wellbore integrity analysis of a natural CO 2 producer, International Journal of Greenhouse Gas Control, 4 (2010) 186-197.

[11] B. Lecampion, D. Quesada, M. Loizzo, A. Bunger, J. Kear, L. Deremble, J. Desroches, Interface debonding as a controlling mechanism for loss of well integrity: Importance for CO2 injector wells, Energy Procedia, 4 (2011) 5219-5226.

[12] M. Zhang, S. Bachu, Review of integrity of existing wells in relation to CO2geological storage: What do we know?, International Journal of Greenhouse Gas Control, 5 (2011) 826-840.

[13] E.B. Nelson, Well cementing, in: Newnes, 1990.

[14] R.D. Vidic, S.L. Brantley, J.M. Vandenbossche, D. Yoxtheimer, J.D. Abad, Impact of shale gas development on regional water quality, Science, 340 (2013) 1235009.

[15] R.B. Jackson, A. Vengosh, T.H. Darrah, N.R. Warner, A. Down, R.J. Poreda, S.G. Osborn, K. Zhao, J.D. Karr, Increased stray gas abundance in a subset of drinking water wells near

Marcellus shale gas extraction, Proceedings of the National Academy of Sciences, 110 (2013) 11250-11255.
[16] S.M. Miller, S.C. Wofsy, A.M. Michalak, E.A. Kort, A.E. Andrews, S.C. Biraud, E.J. Dlugokencky, J. Eluszkiewicz, M.L. Fischer, G. Janssens-Maenhout, Anthropogenic emissions of methane in the United States, Proceedings of the National Academy of Sciences, 110 (2013) 20018-20022.
[17] API Guidance Document, Hydraulic Fracturing Operations-Well Construction and Integrity Guidelines, in: API Guidance Document HF1, American Petroleum Institute Washington, DC, 2009, pp. 36.
[18] G.E. King, D.E. King, Environmental Risk Arising From Well-Construction Failure--Differences Between Barrier and Well Failure and Estimates of Failure Frequency Across Common Well Types Locations and Well Age, SPE-166142.SPE Production & Operations, 28 (2013) 323-344.
[19] T.L. Watson, S. Bachu, Evaluation of the potential for gas and CO2 leakage along wellbores, in: E&P Environmental and Safety Conference, Society of Petroleum Engineers, 2007.
[20] C. Teodoriu, C. Kosinowski, M. Amani, J. Schubert, A. Shadravan, Wellbore Integrity and Cement Failure at HPHT Conditions, International Journal of Engineering, 2 (2013) 2305-8269.
[21] G. Altun, J. Langlinais, A. Bourgoyne Jr, Application of a new model to analyze leak-off tests, SPE Drilling & Completion, 16 (2001) 108-116.
[22] A. Wojtanowicz, D. Zhou, Borehole failure resulting from formation integrity (leak-off) testing in upper marine sediments offshore, Journal of energy resources technology, 120 (1998) 111-117.
[23] D. Postler, Pressure integrity test interpretation, in: SPE/IADC drilling conference, Society of Petroleum Engineers, 1997.
[24] D. Lee, T. Bratton, R. Birchwood, Leak-Off Test Interpretation and Modeling with Application to Geomechanics, in: American Rock Mechanics Association (ARMA), American Rock Mechanics Association, Houston, Texas, 2004.
[25] Y. Feng, K. Gray, A comparison study of extended leak-off tests in permeable and impermeable formations, in: 50th US Rock Mechanics/Geomechanics Symposium, American Rock Mechanics Association, 2016.
[26] D.T. Mueller, R.N. Eid, Characterization of the Early-Time Mechanical Behavior of Well Cements Employed in Surface Casing Operations, in: SPE Drilling Conference, Society of Petroleum Engineers, Florida, USA, 2006.
[27] P. Skalle, A. Aamodt, O.E. Gundersen, Detection of symptoms for revealing causes leading to drilling failures, SPE Drilling & Completion, 28 (2013) 182-193.

[28] A. Nabipour, B. Joodi, M. Sarmadivaleh, Finite element simulation of downhole stresses in deep gas wells cements, in: SPE Deep Gas Conference and Exhibition, Society of Petroleum Engineers, Manama, Bahrain, 2010.
[29] R.K. Khandka, Leakage behind casing, in: Drilling specialization thesis Work Norwegian University of Science and Technology 2007.
[30] B. Reddy, Y. Xu, K. Ravi, D.W. Gray, P. Pattillo, Cement Shrinkage Measurement in Oilwell Cementing--A Comparative Study of Laboratory Methods and Procedures, SPE Drilling & Completion, 24 (2009) 104-114.
[31] K. Ravi, M. Bosma, O. Gastebled, Improve the economics of oil and gas wells by reducing the risk of cement failure, in: SPE Drilling Conference, Society of Petroleum Engineers, Dallas, Texas, 2002.
[32] K. Goodwin, R. Crook, Cement sheath stress failure, SPE-20453.SPE drilling engineering, 7 (1992) 291-296.
[33] M. Bellabarba, H. Bulte-Loyer, B. Froelich, S. Le Roy-Delage, R. van Kuijk, S. Zeroug, D. Guillot, N. Moroni, S. Pastor, A. Zanchi, Ensuring zonal isolation beyond the life of the well, Oilfield Review, 20 (2007) 18-31.
[34] M.B. Dusseault, M.N. Gray, P.A. Nawrocki, Why oilwells leak: cement behavior and long-term consequences, in: International Oil and Gas Conference and Exhibition, SPE-64733.Society of Petroleum Engineers, Beijing, China, 2000.
[35] A. Albawi, Influence of Thermal Cycling on Cement Sheath Integrity, in: Department of Petroleum Engineering and Applied Geophysics, Norwegian University of Science and Technology, 2013.
[36] A.-P. Bois, A. Garnier, F. Rodot, J. Sain-Marc, N. Aimard, How to prevent loss of zonal isolation through a comprehensive analysis of microannulus formation, SPE-124719. SPE Drilling & Completion, 26 (2011) 13-31.
[37] W. Wang, A.D. Taleghani, Three-dimensional analysis of cement sheath integrity around Wellbores, Journal of Petroleum Science and Engineering, 121 (2014) 38-51.
[38] R. Maharidge, A. Bottiglieri, S. Dighe, A. Holley, H. Zhang, A. Koch, Development of Permeability and Mechanical Properties of Class G Cement from Slurry to Set, in: SPE Annual Technical Conference and Exhibition, Society of Petroleum Engineers, 2016.
[39] S. Saidin, S. Sonny Irawan, F.F. Nuruddin, New Approach for Optimizing Cement Design To Eliminate Microannulus in Steam Injection Well, in: International PetroleumTechnology Conference, KualaLumpur,Malaysia, 2008.

[40] C. Teodoriu, K.M. Reinicke, C. Fichter, P. Wehling, Investigations on casing-cement interaction with application to gas and CO2 storage wells, in: SPE EUROPEC/EAGE Annual Conference and Exhibition, Society of Petroleum Engineers, 2010.
[41] K. Ravi, M. Bosma, O. Gastebled, Safe and economic gas wells through cement design for life of the well, in: SPE Gas Technology Symposium, Society of Petroleum Engineers, 2002.
[42] E.B. Nelson, Well cementing, Newnes, Amsterdam ; New York : New York, NY, USA : Elsevier ; Distributors for the United States and Canada, Elsevier Science Pub. Co, 1990.
[43] K. Ravi, M. Bosma, O. Gastebled, Improve the economics of oil and gas wells by reducing the risk of cement failure, in: IADC/SPE Drilling Conference, Society of Petroleum Engineers, 2002.
[44] M. Bosma, K. Ravi, W. van Driel, G. Schreppers, Design Approach to Sealant Selection for the Life of the Well, in: SPE Annual Technical Conference and Exhibition, Houston, Texas, 1999.
[45] M. Shahri, J.J. Schubert, M. Amani, Detecting and Modeling Cement Failure in High-Pressure/High-Temperature (HP/HT) Wells Using Finite Element Method (FEM), in: International Petroleum Technology Conference, Doha, Qatar, 2005.
[46] J.E. Griffith, G. Lende, K. Ravi, A. Saasen, N.E. Nødland, O.H. Jordal, Foam cement engineering and implementation for cement sheath integrity at high temperature and high pressure, in: SPE drilling conference, Dallas, Texas, 2004.
[47] K.E. Gray, E. Podnos, E. Becker, Finite-element studies of near-wellbore region during cementing operations: Part I, SPE-106998.SPE drilling & completion, 24 (2009) 127.
[48] Y. Li, S. Liu, Z. Wang, J. Yuan, F. Qi, Analysis of cement sheath coupling effects of temperature and pressure in non-uniform in-situ stress field, in: International Oil and Gas Conference and Exhibition Beijing, China, 2010.
[49] S. Guo, Y. Bu, X. Yan, Cement Sheath Integrity under Two Different Formation Conditions in Steam Stimulation Well, in: The Twenty-fifth International Ocean and Polar Engineering Conference, International Society of Offshore and Polar Engineers, 2015.
[50] Y. Feng, E. Podnos, K. Gray, Well Integrity Analysis: 3D Numerical Modeling of Cement Interface Debonding, in: 50th US Rock Mechanics/Geomechanics Symposium, American Rock Mechanics Association, Huston, Texas, 2016.
[51] W. Fleckenstein, A. Eustes, M. Miller, Burst induced stresses in cemented wellbores, in: SPE/AAPG Western Regional Meeting, Society of Petroleum Engineers, 2000.
[52] L. Zhang, X. Yan, X. Yang, X. Zhao, Evaluation of wellbore integrity for HTHP gas wells under solid-temperature coupling using a new analytical model, Journal of Natural Gas Science and Engineering, 25 (2015) 347-358.

[53] Y. Guen, S. Asamoto, E. Houdu, O. Poupard, Well Integrity: Modeling of Thermo-Mechanical Behavior and Gas Migration along Wells-Application to Ketzin Injection Well, Energy Procedia, 23 (2012) 462-471.
[54] J. Lubliner, J. Oliver, S. Oller, E. Onate, A plastic-damage model for concrete, International Journal of solids and structures, 25 (1989) 299-326.
[55] J. Lee, G.L. Fenves, Plastic-damage model for cyclic loading of concrete structures, Journal of engineering mechanics, 124 (1998) 892-900.
[56] Z.P. Bažant, B.H. Oh, Crack band theory for fracture of concrete, Matériaux et construction, 16 (1983) 155-177.
[57] D. Hibbitt, B. Karlsson, P. Sorensen, ABAQUS documents (version 6.14), in: Dassault Systemes Simulia Corporation, 2011.
[58] U.M.v. Abaqus, 6.14, Providence: Hibbit Karlsson and Sorensen, (2015).
[59] P. Jackson, C. Murphey, Effect of casing pressure on gas flow through a sheath of set cement, in: SPE-25698/IADC drilling conference, Society of Petroleum Engineers, 1993.
[60] P. Roy, J.P. Morris, S.D. Walsh, J. Iyer, S. Carroll, J. Todorovic, K. Gawel, M. Torsæter, Assessment of Thermal Stress on Well Integrity as a Function of Size and Material Properties, Energy Procedia, 114 (2017) 5241-5248.
[61] S. Abbas, B. Lecampion, R. Prioul, Competition Between Transverse And Axial Hydraulic Fractures In Horizontal Wells, in: SPE Hydraulic Fracturing Technology Conference SPE-163848.Society of Petroleum Engineers, 2013.
[62] Z. Luo, S. Bryant, Influence of thermo-elastic stress on fracture initiation during CO2 injection and storage, Energy Procedia, 4 (2011) 3714-3721.
[63] M. Thiercelin, B. Dargaud, J. Baret, W. Rodriquez, Cement design based on cement mechanical response, SPE drilling & completion, 13 (1998) 266-273.
[64] X. Honglin, Z. Zhang, T. Shi, J. Xiong, Influence of the WHCP on cement sheath stress and integrity in HTHP gas well, Journal of Petroleum Science and Engineering, 126 (2015) 174–180.
[65] Y. Shi, B. Li, B. Guo, Z. Guan, H. Li, An Analytical Solution to Stress State of Casing-Cement Sheath-Formation System with the Consideration of its Initial Loaded State and Wellbore Temperature Variation, International Journal of Emerging Technology and Advanced Engineering, 5 (2015) 59-65.
[66] J. De Andrade, S. Sangesland, Cement sheath failure mechanisms: numerical estimates to design for long-term well integrity, Journal of Petroleum Science and Engineering, 147 (2016) 682-698.
[67] A. Al-Ajmi, Wellbore stability analysis based on a new true-triaxial failure criterion, in: Land Water Recour. Eng., KTH, 2006.

[68] P. Pattillo, T. Kristiansen, Analysis of horizontal casing integrity in the Valhall field, in: SPE/ISRM Rock Mechanics Conference, Society of Petroleum Engineers, 2002.
[69] L.R. Alejano, A. Bobet, Drucker–Prager Criterion, Rock Mechanics and Rock Engineering, 45 (2012) 995-999.
[70] H. Jiang, Y. Xie, A note on the Mohr–Coulomb and Drucker–Prager strength criteria, Mechanics Research Communications, 38 (2011) 309-314.
[71] O. Dahlblom, N.S. Ottosen, Smeared crack analysis using generalized fictitious crack model, Journal of engineering mechanics, 116 (1990) 55-76.
[72] S. Ghabezloo, J. Sulem, S. Guédon, F. Martineau, J. Saint-Marc, Poromechanical behaviour of hardened cement paste under isotropic loading, Cement and Concrete research, 38 (2008) 1424-1437.
[73] S. Petty, J. Gastineau, D.L. Bour, K. Ravi, Life Cycle Modeling of Wellbore Cement Systems Used for Enhanced Geothermal System Development, in: 28th Workshop on Geothermal Reservoir Engineering, Stanford U.(27–29 January 2003), 2003.
[74] R. Nygaard, S. Salehi, B. Weideman, R.G. Lavoie, Effect of dynamic loading on wellbore leakage for the wabamun area CO2-sequestration project, Journal of Canadian Petroleum Technology, 53 (2014) 69-82.
[75] H.Y. Zhu, J.G. Deng, J. Zhao, H. Zhao, H.L. Liu, T. Wang, Cementing failure of the casing-cement-rock interfaces during hydraulic fracturing, Computers and Concrete, 14 (2014) 91-107.
[76] F. Ansari, Q. Li, High-strength concrete subjected to triaxial compression, Materials Journal, 95 (1998) 747-755.
[77] I. Imran, S. Pantazopoulou, Experimental study of plain concrete under triaxial stress, ACI Materials Journal-American Concrete Institute, 93 (1996) 589-601.
[78] J. Dorris, S. Nemat-Nasser, A plasticity model for flow of granular materials under triaxial stress states, International journal of solids and structures, 18 (1982) 497-531.
[79] T. Rabczuk, Computational methods for fracture in brittle and quasi-brittle solids: state-of-the-art review and future perspectives, ISRN Applied Mathematics, 2013 (2013).
[80] S. Yazdani, H. Schreyer, Combined plasticity and damage mechanics model for plain concrete, Journal of engineering mechanics, 116 (1990) 1435-1450.
[81] T. Wolterbeek, C. Peach, C.Spiers, Reaction and transport in wellbore interfaces under $CO_2$ storage conditions: Experiments simulating debonded cement–casing interfaces, International Journal of Greenhouse Gas Control, 19 (2013) 519-529.
[82] W. Wang, Emergence of Delamination Fractures around Casing and Its Stability, in, University of Louisiana State University, 2014, pp. 201.

[83] N. Barton, V. Choubey, The shear strength of rock joints in theory and practice, Rock mechanics, 10 (1977) 1-54.
[84] L. Carter, G. Evans, A study of cement-pipe bonding, Journal of Petroleum Technology, 16 (1964) 157-160.
[85] H.K. Ladva, B. Craster, T.G. Jones, G. Goldsmith, D. Scott, The cement-to-formation interface in zonal isolation, SPE Drilling & Completion, 20 (2004) 186-197.
[86] G.W. Evans, L.G. Carter, Bounding Studies of Cementing Compositions to Pipe and Formations, in: Drilling and production Practice, American Petroleum Institute, New York, 1962.
[87] ABAQUS, Surface-based cohesive behavior, in: Analysis User's Guide 6.14, Dassault Systèmes.
[88] J. Makar, K. Luke, Thermal Stability of the Cement Sheath in Steam Treated Oil Wells, Journal of the American Ceramic Society, 94 (2011) 4463-4470.
[89] Z. Yuan, P. Gardoni, J. Schubert, C. Teodoriu, Cement failure probability analysis in water injection well, Journal of Petroleum Science and Engineering, 107 (2013) 45-49.
[90] B. Reddy, A.K. Santra, D.E. McMechan, D.W. Gray, C. Brenneis, R. Dunn, Cement mechanical property measurements under wellbore conditions, SPE-95921.SPE Drilling & Completion, 22 (2005) 33-38.
[91] L. Roy-Delage, C. Baumgarte, M. Thiercelin, B. Vidick, New cement systems for durable zonal isolation, in: IADC/SPE Drilling Conference, Society of Petroleum Engineers, 2000.
[92] M. Nasvi, P. Ranjith, J. Sanjayan, Comparison of mechanical behaviors of geopolymer and class G cement as well cement at different curing temperatures for geological sequestration of carbon dioxide, in: 46th US Rock Mechanics/Geomechanics Symposium, American Rock Mechanics Association, 2012.
[93] S.G. James, L. Boukhelifa, Zonal isolation modeling and measurements-past myths and today's realities, SPE-101310.SPE Drilling & Completion, 23 (2008) 68-75.
[94] D. Guner, H. Ozturk, Comparison of Mechanical Behaviour of G Class Cements for different Curing Time, in: 24th International Mining Congress and Exhibition Turkey, 2015.
[95] C. Teodoriu, P. Asamba, Experimental study of salt content effect on class G cement properties with application to well integrity, Journal of Natural Gas Science and Engineering, 24 (2015) 324-329.
[96] N. Romanowski, A. Ichim, C. Teodoriu, Investigations on Oilwell Cement Strength Response to Ultrasonic Measurements in the Presence of Additives, Journal of Energy Resources Technology, 140 (2018) 072904.

[97] T. Heinold, R.L. Dillenbeck, M.J. Rogers, The effect of key cement additives on the mechanical properties of normal density oil and gas well cement systems, in: SPE Asia Pacific Oil and Gas Conference and Exhibition, Society of Petroleum Engineers, 2002.
[98] R.L. Dillenbeck, G. Boncan, V. Clemente, M.J. Rogers, Testing cement static tensile behavior under downhole conditions, in: SPE Eastern Regional Meeting, Society of Petroleum Engineers, 2005.
[99] T. Heinold, R.L. Dillenbeck, W.S. Bray, M.J. Rogers, Analysis of Tensile Strength Test Methodologies For Evaluating Oil and Gas Well Cement Systems, in: SPE Annual Technical Conference and Exhibition, Society of Petroleum Engineers, 2003.
[100] G. Quercia, D. Chan, K. Luke, Weibull statistics applied to tensile testing for oil well cement compositions, Journal of Petroleum Science and Engineering, 146 (2016) 536-544.
[101] W. Weibull, A statistical distribution function of wide applicability, Journal of applied mechanics, 18 (1951) 293-297.
[102] W. Morris, M.A. Criado, J. Robles, G. Bianchi, Design of high toughness cement for effective long lasting well isolations, in: SPE Latin American and Caribbean Petroleum Engineering Conference, Society of Petroleum Engineers, 2003.
[103] Z. Yuan, C. Teodoriu, J. Schubert, Low cycle cement fatigue experimental study and the effect on HPHT well integrity, Journal of Petroleum Science and Engineering, 105 (2013) 84-90.
[104] M. Labibzadeh, B. Zahabizadeh, A. Khajehdezfuly, Early-age compressive strength assessment of oil well class G cement due to borehole pressure and temperature changes, Journal of American Science, 6 (2010) 1-7.
[105] J. Del Viso, J. Carmona, G. Ruiz, Shape and size effects on the compressive strength of high-strength concrete, Cement and Concrete Research, 38 (2008) 386-395.
[106] F.K. Kong, R.H. Evans, Reinforced and prestressed concrete, CRC Press, 2014.
[107] M.K. Abd, Z.D. Habeeb, Effect of Specimen Size and Shape on Compressive Strength of Self-Compacting Concrete, Diyala Journal of Engineering Sciences, 7 (2014) 16-29.
[108] M. Thiercelin, B. Dargaud, J. Baret, W. Rodriguez, Cement design based on cement mechanical response, in: SPE annual technical conference and exhibition, Society of Petroleum Engineers, 1997.
[109] D. Bentz, Transient plane source measurements of the thermal properties of hydrating cement pastes, Materials and structures, 40 (2007) 1073-1080.
[110] A. Loiseau, Thermal Expansion of Cement and Well Integrity of Heavy Oil Wells, in: SPE Heavy and Extra Heavy Oil Conference, Medellín, Colombia, 2014.
[111] G.E. King, D.E. King, Environmental Risk Arising From Well-Construction Failure--Differences Between Barrier and Well Failure, and Estimates of Failure Frequency Across

Common Well Types, Locations, and Well Age, SPE Production & Operations, 28 (2013) 323-344.
[112] J.F. Heathman, F.E. Beck, Finite Element Analysis Couples Casing and Cement Designs for HTHP Wells in East Texas, in: SPE Drilling Conference, Florida, USA, 2006.
[113] M. Thiercelin, C. Baumgarte, D. Guillot, A Soil Mechanics Approach To Predict Cement Sheath Behavior, in: Rock Mechanics in Petroleum Engineering, Society of Petroleum Engineers, Trondheim, Norway, 1998.
[114] S. Salehi, Numerical simulations of fracture propagation and sealing: implications for wellbore strengthening, in: Geosciences and Geological and Petroleum Engineering Department, Missouri University, 2012, pp. 222.
[115] J. Lee, G.L. Fenves, A plastic-damage concrete model for earthquake analysis of dams, Earthquake engineering & structural dynamics, 27 (1998) 937-956.
[116] E. Arjomand, T. Bennett, G. Nguyen, Study of class G well cement behavior under triaxial compression and flexure tests, in: Mechanics of Structures and Materials: Advancements and Challenges, CRC Press, Curtin University, Perth, WA, 2016, pp. 933-938.
[117] K. Thuro, R. Plinninger, S. Zäh, S. Schütz, Scale effects in rock strength properties. Part 1: Unconfined compressive test and Brazilian test, EUROCK 2001: Rock Mechanics-A Challenge for Society, (2001) 169-174.
[118] C. Teodoriu, P. Asamba, A. Ichim, Well Integrity Estimation of Salt Cements with Application to Long Term Underground Storage Systems, in: SPE Europec featured at 78th EAGE Conference and Exhibition, Society of Petroleum Engineers, 2016.
[119] C. Teodoriu, M. Amani, Z. Yuan, J. Schubert, C. Kosinowski, Investigation of the mechanical properties of class g cement and their effect on well integrity, International Journal of Engineering, 3 (2013) 2305-8269.
[120] ASTM, C 348-02 Standard test method for flexural strength of hydraulic-cement mortars, in, 2002.
[121] X. Shen, M. Bai, W. Standifird, Drilling and Completion in Petroleum Engineering: Theory and Numerical Applications, CRC Press, 2011.
[122] S. Oller, E. Onate, J. Oliver, J. Lubliner, Finite element nonlinear analysis of concrete structures using a “plastic-damage model”, Engineering Fracture Mechanics, 35 (1990) 219-231.
[123] T. Jankowiak, T. Lodygowski, Identification of parameters of concrete damage plasticity constitutive model, Foundations of civil and environmental engineering, 6 (2005) 53-69.
[124] G. Schickert, H. Winkler, Results of test concerning strength and strain of concrete subjected to multi-axial compressive stress, in: deutsche ausschuss fὺr stahlbeton, Berlin,Germany, 1977.

[125] F.E. Richart, A. Brandtzaeg, R.L. Brown, A study of the failure of concrete under combined compressive stresses, in, University of Illinois at Urbana Champaign, College of Engineering. Engineering Experiment Station., 1928.
[126] L.L. Mills, R.M. Zimmerman, Compressive strength of plain concrete under multiaxial loading conditions, Journal of Proceedings, 67 (1970) 802-807.
[127] R. Halama, M. Šofer, F. Fojtík, Choice and calibration of cyclic plasticity model with regard to subsequent fatigue analysis, Engineering Mechanics, 19 (2012) 87-97.
[128] G.D. Nguyen, A.M. Korsunsky, Development of an approach to constitutive modelling of concrete: isotropic damage coupled with plasticity, International Journal of Solids and Structures, 45 (2008) 5483-5501.
[129] J. Handin, Strength of oil well cements at downhole pressure-temperature conditions, SPE-1300.Society of Petroleum Engineers Journal, 5 (1965) 341-347.
[130] A. Philippacopoulos, M. Berndt, Mechanical property issues for geothermal well cements, Geothermal Resources Council Transactions, 25 (2001) 119-124.
[131] A. Hillerborg, M. Modéer, P.-E. Petersson, Analysis of crack formation and crack growth in concrete by means of fracture mechanics and finite elements, Cement and concrete research, 6 (1976) 773-781.
[132] W. Wang, A. Dahi Taleghani, Emergence and propagation of delamination cracks along the casing-cement interface, ARMA (American Rock Mechanics Association), (2012) 12-449.
[133] M. Benzeggagh, M. Kenane, Measurement of mixed-mode delamination fracture toughness of unidirectional glass/epoxy composites with mixed-mode bending apparatus, Composites science and technology, 56 (1996) 439-449.
[134] C. Luo, J. Lua, P.E. DesJardin, Thermo-mechanical damage modeling of polymer matrix sandwich composites in fire, Composites Part A: Applied Science and Manufacturing, 43 (2012) 814-821.
[135] N. van der Tuuk Opedal, M. Torsæter, T. Vrålstad, P. Cerasi, Potential Leakage Paths along Cement-formation Interfaces in Wellbores; Implications for $CO_2$ Storage, Energy Procedia, 51 (2014) 56-64.
[136] S. Manoochehr Salehabadi, S. Min Jin, H.H. Jinhai Yang, S. Bahman Tohidi, Finite Element Modelling of Casing in Gas Hydrate Bearing Sediments, in: EAGE Annual Conference and Exhibition, Rome, Italy, 2008.
[137] Schlumberger, Well Services Field Data Handbook (i-Handbook), in: version1,0,4,2, 2006.
[138] API Specification 10A, 10A:"Specifications for Cements and Materials for Well Cementing," in, American Petroleum Institute, Washington, DC, 1995.

[139] B. Lothenbach, F. Winnefeld, C. Alder, E. Wieland, P. Lunk, Effect of temperature on the pore solution, microstructure and hydration products of Portland cement pastes, Cement and Concrete Research, 37 (2007) 483-491.
[140] RILEM, Determination of the Fracture Energy of Mortar and Concrete by Means of Three-Point Bend Tests on Notched Beames, in: Materials and Structures, RILEM Recommendation, 1985, pp. 285-290.
[141] P.L. Narloch, M. Lidner, E. Kunicka, M. Bielecki, Flexural Tensile Strength of Construction Elements Made out of Cement Stabilized Rammed Earth, Procedia Engineering, 111 (2015) 589-595.
[142] G. Gao, S. Huang, K. Xia, Z. Li, Application of digital image correlation (DIC) in dynamic notched semi-circular bend (NSCB) tests, Experimental Mechanics, 55 (2015) 95-104.
[143] B. Pan, K. Qian, H. Xie, A. Asundi, Two-dimensional digital image correlation for in-plane displacement and strain measurement: a review, Measurement science and technology, 20 (2009) 062001.
[144] S. Shah, J.C. Kishen, Fracture properties of concrete–concrete interfaces using digital image correlation, Experimental mechanics, 51 (2011) 303-313.
[145] H. Munoz, A. Taheri, E. Chanda, Pre-peak and post-peak rock strain characteristics during uniaxial compression by 3D digital image correlation, Rock Mechanics and Rock Engineering, 49 (2016) 2541-2554.
[146] F. Lin, C. Meyer, Hydration kinetics modeling of Portland cement considering the effects of curing temperature and applied pressure, Cement and Concrete Research, 39 (2009) 255-265.
[147] E. Arjomand, T. Bennett, G.D. Nguyen, Evaluation of cement sheath integrity subject to enhanced pressure, Journal of Petroleum Science and Engineering, 170 (2018) 1-13.
[148] A. Ouellet, T. Bérard, J. Desroches, P. Frykman, P. Welsh, J. Minton, Y. Pamukcu, S. Hurter, C. Schmidt-Hattenberger, Reservoir geomechanics for assessing containment in CO2 storage: a case study at Ketzin, Germany, Energy Procedia, 4 (2011) 3298-3305.
[149] M. Balla, Formulation of Coupled Problems Of Thermoelasticity By Finite Elements, Periodica Polytechnica Mechanical Engineering, 33 (1989) 59-70.
[150] T.K. Wolterbeek, C.J. Peach, C.J. Spiers, Reaction and transport in wellbore interfaces under CO2 storage conditions: experiments simulating debonded casing-cement interfaces.
[151] Z.-H. Jin, C. Sun, Cohesive zone modeling of interface fracture in elastic bi-materials, Engineering fracture mechanics, 72 (2005) 1805-1817.
[152] C.G. Dávila, P.P. Camanho, M.F. de Moura, Mixed-mode decohesion elements for analyses of progressive delamination, in: Proceedings of the 42nd AIAA/ASME/ASCE/AHS/ASC Structures, Structural Dynamics and Materials Conference, Seattle, WA, 2001.

[153] ABAQUS, in, Dassault Systèmes. , 2014.
[154] M. Zhang, C. Zuo, B. Sun, B. Gu, Thermal ageing degradation mechanisms on compressive behavior of 3-D braided composites in experimental and numerical study, Composite Structures, 140 (2016) 180-191.
[155] S. Salehi, R. Nygaard, Numerical Study of Fracture Initiation, Propagation, Sealing to Enhance Wellbore Fracture Gradient, in: 45th US Rock Mechanics/Geomechanics Symposium, American Rock Mechanics Association, 2011.
[156] M. Salehabadi, M. Jin, J. Yang, R. Ahmed, B. Tohidi, Effect of Casing Eccentricity on Casing Stability Analysis in Wellbores Drilled in Gas Hydrate Bearing Sediments, in: SPE EUROPEC/EAGE Annual Conference and Exhibition, Society of Petroleum Engineers, 2010.
[157] M. Salehabadi, Hydrates in sediments: their role in wellbore/casing integrity and CO2 sequestration, in, Heriot-Watt University, 2009.
[158] P. Roy, S.D. Walsh, J.P. Morris, J. Iyer, Y. Hao, S. Carroll, K. Gawel, J. Todorovic, M. Torsæter, Studying the Impact of Thermal Cycling on Wellbore Integrity during CO 2 Injection, in: 50th US Rock Mechanics/Geomechanics Symposium, American Rock Mechanics Association, 2016.